2022

53BP1/Shieldin Counteract DSB Resection Through Fill-In Synthesis

Zachary Kenneth Mirman

53BP1/shieldin counteract DSB resection through fill-in synthesis

A Thesis Presented to the Faculty of

The Rockefeller University

in Partial Fulfillment of the Requirements for

the degree of Doctor of Philosophy

by

Zachary Kenneth Mirman

June 2022

53BP1/shieldin counteract DSB resection through fill-in synthesis

Zachary Kenneth Mirman, Ph.D.

The Rockefeller University 2022

53BP1 is a DNA damage response (DDR) factor that gained notoriety because it determines the efficacy of PARP1 inhibitors (PARPi) in BRCA1-deficient cancers. Additionally, 53BP1 promotes end-to-end fusions of telomeres lacking end protection from the shelterin component TRF2, and facilitates end-joining at programmed breaks generated during class switch recombination in the immune system. The role of 53BP1 in double strand break (DSB) repair outside of these three well-studied contexts is less clear, though it has been proposed that 53BP1 acts as a master regulator of so-called "DSB repair pathway choice," promoting classical non-homologous end-joining (cNHEJ) at the expense of homology-directed repair (HDR). In the introductory chapter to the thesis, we first discuss our current understanding of the literature regarding 53BP1 and then present an alternate view: that the features of 53BP1 have evolved to promote high-fidelity DNA repair and avoid mutagenesis. This notion is supported by the data presented in the subsequent two chapters. We demonstrate that 53BP1 and its downstream effectors RIF1 and the shieldin complex limit the generation of long 3' overhangs at DSBs by recruiting CST/Polα to counteract resection, challenging the long-standing model of a block to resection by this pathway. Like loss of 53BP1/RIF1/shieldin, disruption of CST/Polα/primase reverses the hallmarks of BRCA1-deficiency. CST/Polα localize to DSBs, and we directly detect fill-in synthesis by

observing shieldin/CST/Polα/primase-dependent nucleotide incorporation. We also demonstrate that tethering CST to DSBs can bypass the need for recruitment by 53BP1/shieldin. A novel shieldin mutant which fails to recruit CST was non-functional in BRCA1-deficient cells, but its function could be fully restored by chemical-induced dimerization with CST. These results indicated that in BRCA1-deficient cells, CST/Polα/primase is the major effector of 53BP1/shieldin function. After an interlude (Chapter 4) on the role of CRL4/DDB1/WDR70 in regulation of the DDR, I discuss and contextualize the new results and revisit the model of 53BP1 as a DSB escort which controls DSB processing and promotes high-fidelity repair.

Dedicated to my mother, Nancy (1949-2021)

ACKNOWLEDGMENTS

I am grateful and indebted to many people for inspiring and facilitating the research presented here. Foremost are members, past and present, of the de Lange lab: Stew Barnes, Rosaura Mejia, Kaori Takai, and Devon White for their support; Alessandro Bianchi for help with yeast work; Leonid Timashev and Zhe Yang for help with image analysis; Zhe Yang, Hiro Takai, and other former lab members for generating useful reagents. Former lab members John Maciejowski and Sally Dewhurst are thanked particularly for keeping me going in and out of the lab. Current lab members Nanda Sasi and Audrey Goldfarb are thanked for being superb bay-mates and superlative friends. Thank you also to Keshav Sharma for working diligently with me on WDR70. My sincerest gratitude and respect go to the researchers in the lab who trained me and collaborated with me in my first few years in the lab: Tatsuya Kibe, Yi Gong, Hiro Takai, and most of all my dear collaborator and friend, Francisca Lottersberger. I am also appreciative of Adriana Garzon, the best lab manager one could hope for. And finally, to Titia: I have been extraordinarily fortunate to have five years to learn from you, work with you, and share with you a small portion of your journey. Truly—thank you.

Rockefeller University is a special place that I have been lucky to call home for these years. I am deeply grateful to my friends in Security, Plant Operations, and Housing, and to the Dean's Office for making RU the best place to be a PhD student. I am particularly grateful to Sid Strickland for bringing me to Rockefeller and making me feel at home here from *before* "day one." I am also thankful to the Rockefeller core facilities including the BioImaging Center and the Flow Cytometry Resource Center for their support.

My colleagues in the genome integrity field have provided many helpful and memorable discussions for which I am grateful. They include Ylli Doksani, Ross Chapman, Simon Powell, Maria Jasin, Scott Keeney, Roger Greenberg, Gaelle Legube, and Dan Durocher. Drs. Greenberg, Legube, and Durocher, along with Carolyn Price are also thanked for providing reagents.

I wish to thank my thesis committee members, Fred Cross and Agata Smogorzewska for their excellent insight and advice, and for caring about me and my work. Special thanks also to Alberto Ciccia for serving as the external examiner on my committee. I am grateful for my NCI F99 award (1F99CA245720-01) and for the support for the de Lange lab which helped fund this work: NCI (5 R35 CA210036), NIA (5 R01 AG016642), the Breast Cancer Research Foundation (BCRF-19-036) and the Melanoma Research Alliance (MRA#577521).

Finally, thank you to my dear family. I particularly want to express my love and respect for my two brothers, Aaron and Jesse, and gratitude which cannot be put into words for my parents. And thank you, Marian, for everything.

TABLE OF CONTENTS

LIST OF FIGURES AND TABLES

FIGURES

TABLES

LIST OF ABBREVIATIONS

53BP1	p53-binding protein 1
aNHEJ	Alternative non-homologous end-joining
Aphi	Aphidicolin
ATM	Ataxia telangiectasia-mutated
aux	Auxin
BER	Base excision repair
BLM	Bloom Syndrome protein
BRCA1	Breast cancer associated 1
BRCT	BRCA1 C-terminal
BrdU	Bromodeoxyuridine
CDK	Cyclin dependent kinase
CID	Chemical-induced dimerization
cNHEJ	Classical non-homologous end-joining
co-IP	Co-immunoprecipiation
CRL	Cullin ring ligase
CSR	Class switch recombination
CST	CTC1, STN1, TEN1 complex
DAPI	4', 6-diamidino-2-phenylindole
DDB1	DNA damage binding 1
DDR	DNA damage response
DKO	Double knockout
DNA-PKcs	DNA protein kinase catalytic subunit
dox	Doxycycline
DSB	Double-strand break
DWD	DDB1-binding WD40
EdU	Ethynyl deoxyuridine
EXO1	Exonuclease 1
FACS	Fluorescence-activated cell sorting
FFR	Focus forming region
FHA	Forkhead-associated
HDR	Homology-directed repair
HU	Hydroxyurea
IF	Immunofluorescence
IgA	Immunoglobulin A
IR	Ionizing radiation
Kb	Kilobases
LIG4	DNA ligase 4

MAD2L2/REV7	MAD2-like protein 2 (REV7)
mAID	mini-Auxin induced degron
MEF	Mouse embryonic fibroblast
MMR	Mismatch repair
MRN	MRE11, RAD50, NBS1 complex
nt	Nucleotide
OBFC1/STN1	OB fold-containing protein 1 (STN1)
OD	Oligomerization domain
ORF	Open reading frame
PARPi	Poly(ADP-ribose) polymerase inhibitor
PCNA	Proliferating cell nuclear antigen
PCR	Polymerase chain reaction
PLA	Proximity ligation assay
PNKP	Polynucleotide kinase 3' phosphatase
Polα	Polymerase alpha
Polδ	Polymerase delta
PRIM1	DNA Primase small subunit
Rb	Retinoblastoma
RPA	Replication protein A
RPE	Retinal pigment epithelium
SSA	Single-strand annealing
SSB	Single-strand break
ssDNA	Single-stranded DNA
WDR70	WD repeat domain 70
WRN	Werner's Syndrome helicase
wt	wild-type
γH2AX	Phosphorylated histone H2A S139

CHAPTER 1. 53BP1: A DSB Escort

1.1 Abstract

53BP1 is an enigmatic DNA damage response factor that gained prominence because it determines the efficacy of PARP1 inhibitory drugs (PARPi) in BRCA1-deficient cancers. 53BP1 also promotes fusion of deprotected telomeres and end-joining at DSBs during class switch recombination. Recent studies have elevated 53BP1 from its modest status of (yet another) DNA damage factor to master regulator of DSB repair pathway choice. The body of work in this thesis suggests an alternative view, which is introduced in Chapter 1. We first provide an overview of the role of 53BP1 in DSB repair and then propose that 53BP1 has evolved to avoid mutagenic repair outcomes and does so by controlling the processing of DNA ends and the dynamics of DSBs. The consequences of 53BP1 deficiency, such as diminished PARPi efficacy in BRCA1-deficient cells and altered repair of damaged telomeres, can be explained from this viewpoint. We further propose that some of the fidelity functions of 53BP1 co-evolved with class switch recombination (CSR) in the immune system. Finally, we speculate that, rather than being deterministic in DSB repair pathway choice, 53BP1 functions as a DSB escort* that guards against illegitimate and potentially tumorigenic recombination.

1.2 Introduction

*Escort: Late 16th century (originally denoting a body of armed men escorting travelers): from French ***escorte*** (noun), ***escorter*** (verb), from Italian ***scorta***, feminine past participle of ***scorgere*** 'to conduct, guide', based on Latin ***ex-*** 'out of' + ***corrigere*** 'set right'

- Oxford Dictionary of English

Every eukaryotic cell contends with a staggering variety and quantity of threats to its DNA, with insults generating double-strand breaks (DSBs) representing perhaps the most toxic events. A crucial, yet enigmatic player in the repair of DSBs is 53BP1 (p53-binding protein 1, also known as TP53BP1). Although 53BP1 was discovered and named based on its interaction with p53[1], 53BP1 has been most thoroughly characterized in terms of its role at broken DNA ends where it recruits effector proteins to mediate DSB repair[2,3]. Chief among these effector proteins are those that affect the formation of single-strand DNA (ssDNA) at breaks, which is an important step in repair of physiological and pathological DSBs[2,4,5].

DSBs are repaired by two distinct pathways: classical non-homologous end-joining (cNHEJ) and homology-directed repair (HDR) (Figure 1.1). cNHEJ ligates blunt DNA ends or DSBs with short overhangs (Figure 1.1A)[6]. This pathway is initiated by DNA end-binding of the ring-shaped KU70/80 heterodimer which also can hold two DNA ends together[7]. Ligation of the ends requires DNA Ligase IV (LIG4) together with its associated factors (e.g., XRCC4 and XLF). This process requires the catalytic subunit of DNA protein kinase (DNA-PKcs) and, in some settings, is promoted by nucleases (e.g.,

Artemis) and polynucleotide kinase 3' phosphatase (PNKP). cNHEJ is rapid, efficient, and very accurate when the DNA ends are 'clean' (have compatible or blunt ends not blocked by attached proteins). Although active throughout interphase, cNHEJ can be inhibited in S/G2 by CYREN (also called MRI[8,9]) when DSBs contain 5' or 3' overhangs[10]. In contrast, CYREN/MRI stimulates cNHEJ in G1[11].

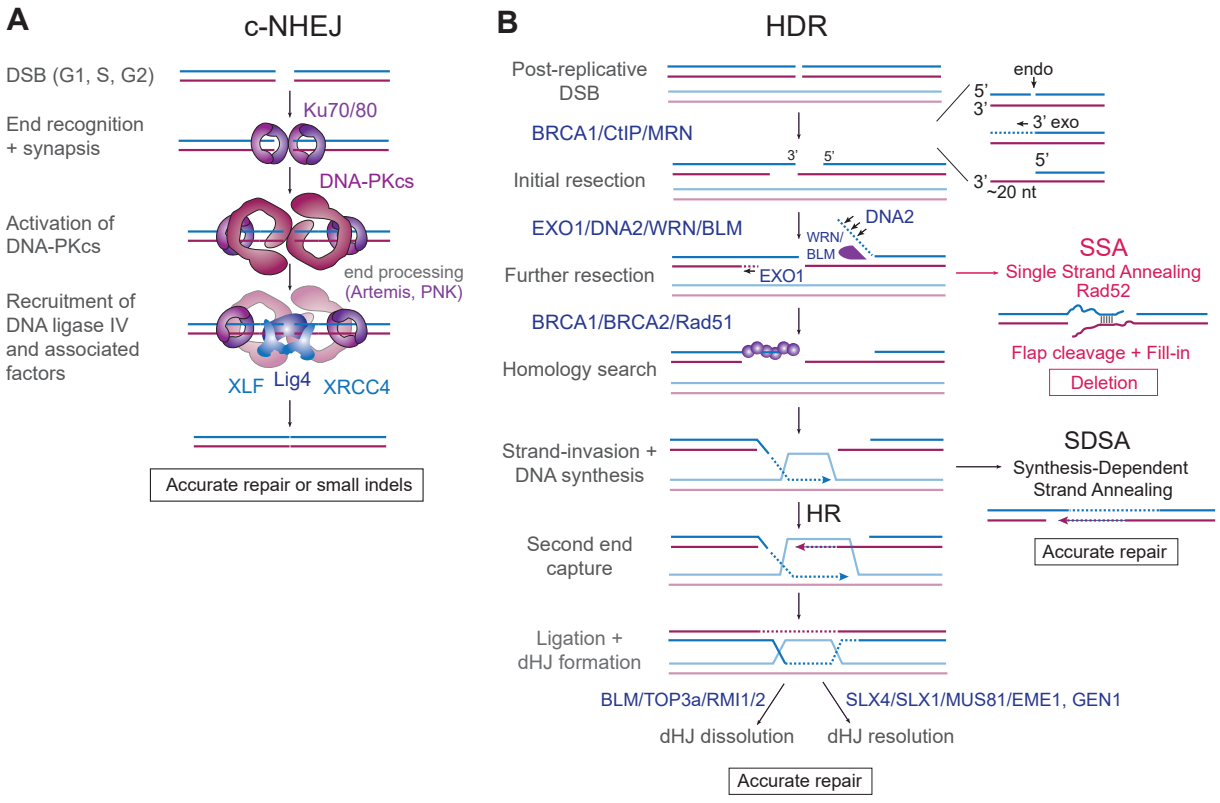

Figure 1.1. The two predominant DSB repair pathways in mammalian cells. A, Schematic of c-NHEJ repair of blunt or minimally-processed DNA ends. This pathway is active throughout the cell cycle and the result is accurate repair or small insertions or deletions (indels). **B**, Schematic of HDR of post-replicative (S/G2) DSBs. This pathway requires the generation of 3' overhangs competent for loading RAD51. Single-Strand Annealing (SSA), resulting in deletions, can also occur if excessive resection exposes regions of homology. Accurate repair is achieved either by SDSA or HR followed by dissolution or resolution of the double Holliday Junction.

Unlike cNHEJ, HDR of DSBs (Figure 1.1B) requires the presence of a 3' overhang[12]. When coated with the RAD51 recombinase, 3' overhangs can initiate the critical strand-invasion event required for HDR. Accurate HDR uses the sister chromatid as a template and DSB repair by HDR is therefore prominent in newly-replicated parts of the genome. The critical step towards HDR, formation of the 3' overhang, is thought to require BRCA1[13]. Resection of the 5' end is initiated by the MRN (MRE11, RAD50, and NBS1) complex in conjunction with CtIP[14]. MRN/CtIP binds to DSBs and possesses both endo- and 3' exonucleolytic activity allowing formation of a short oligonucleotide that can be degraded from its 3' end[15–19]. This process creates a short 3' overhang that can be further processed by long-range 5' end resection either by the processive exonuclease EXO1[15], or by the flap endonuclease DNA2 acting on ssDNA formed by BLM or WRN helicase activity[20]. BRCA2-mediated loading of RAD51 on the ssDNA creates the RAD51 nucleofilament that executes a homology search[21,22]. The resulting strand-invasion generates the substrate for DNA synthesis, which elongates the 3' overhang in a templated fashion. Capture and ligation of the other DNA end generates a double Holliday Junction (dHJ) that can be dissolved through migration by the BTR (BLM-TOP3A-RMI2) complex to separate the sister chromatids without a cross-over. Alternatively, persistent dHJs can be resolved later in the cell cycle by HJ resolvases such as the SLX4/SLX1/MUS81/EME1 complex, and GEN1, yielding separated sister chromatids with or without a cross-over[23]. If the second end is not captured, the extended overhang can anneal to sequences at the second end (after resection) in a process called Synthesis-Dependent Strand Annealing (SDSA) (Figure 1.1B). SDSA leads to accurate repair of DSBs without cross-overs.

Although 3' overhang formation is critical for HDR, excessively long 3' overhangs at DSBs can be dangerous if they contain repetitive sequences that allow the RAD52-dependent single-strand annealing (SSA) pathway to create deletions (Figure 1.1B). DNA breaks with 3' overhangs can also be processed by a second mutagenic DNA repair pathway, referred to as alternative NHEJ (aNHEJ) or microhomology-mediated end-joining (MMEJ). In mammalian cells, aNHEJ requires only minimal homology (1 or more base pairs) between regions of ssDNA and is mediated by enzymes normally involved in Base Excision Repair (BER), such as the Poly(ADP-ribose) polymerase PARP1 and Ligase 3, as well as the error-prone PolQ polymerase[24].

Because of the dependence of accurate HDR (homologous recombination or SDSA) on single-stranded overhangs, the structure of the DSB is a determinant of the repair pathway choice. It is at this node that 53BP1 has been implicated. Experiments involving dysfunctional telomeres, CSR, and PARPi-treated BRCA1-deficient cells established that a central function of 53BP1 at sites of DNA damage is to limit the formation of long 3' protrusions[25–28]. The mechanism by which 53BP1 controls the structure at DNA ends is still elusive. In addition to regulating DNA end processing, 53BP1 has the ability to endow DSBs with greater mobility in the nucleus and can promote synapsis of DNA breaks[29,30].

The finding that 53BP1 deficiency leads to diminished cNHEJ in the settings discussed above has resulted in the proposal that this factor is critical for cNHEJ. However, unlike core cNHEJ factors, loss of 53BP1 confers only mild sensitivity to DNA damage caused by ionizing radiation (IR)[31] or chemical insults[32]. Similarly, although 53BP1-deficiency slightly reduces and delays the cNHEJ of a subset of 'normal' DSBs

(e.g., those induced by IR)[33], this effect is minor compared to the loss of core cNHEJ[32]. Furthermore, unlike the core cNHEJ factors, 53BP1 is not required for cNHEJ of most RAG-induced DNA breaks during V(D)J recombination[34]. Clearly, 53BP1 is not a core cNHEJ factor but can increase the use of cNHEJ in certain settings.

This chapter summarizes the current understanding of the role of 53BP1 in DSB repair at deprotected telomeres, in CSR, and in the context of PARPi-treated BRCA1-deficient cells. We argue that the primary function of 53BP1 is not to regulate the choice between cNHEJ and HDR, but to ensure the fidelity of DSB repair, a function that is corrupted in diseases where DNA repair is rewired, as in BRCA1-deficient cancers. These ideas grew out of the data presented in Chapters 2[35] and 3 of the thesis.

1.3 53BP1

53BP1 is a large scaffold protein composed of domains that mediate interactions with modified histones and several effector proteins[3,36] (Figure 1.2A). The best-understood region of the 53BP1 protein is the central Focus Forming Region (FFR) which is the minimal region required for accumulation of 53BP1 in chromatin near DSBs. It spans the oligomerization domain (OD), a glycine/arginine-rich (GAR) motif, a tandem Tudor domain, and a ubiquitin-dependent recruitment (UDR) motif (Figure 1.2A).

The FFR interacts with modified histones in a manner dependent on the DNA damage response (DDR). At DSBs, DNA damage signaling is initiated by association of MRN with DNA ends and subsequent activation of MRN-bound ataxia telangiectasia-mutated (ATM) kinase. ATM signaling initiates a cascade of chromatin phosphorylation

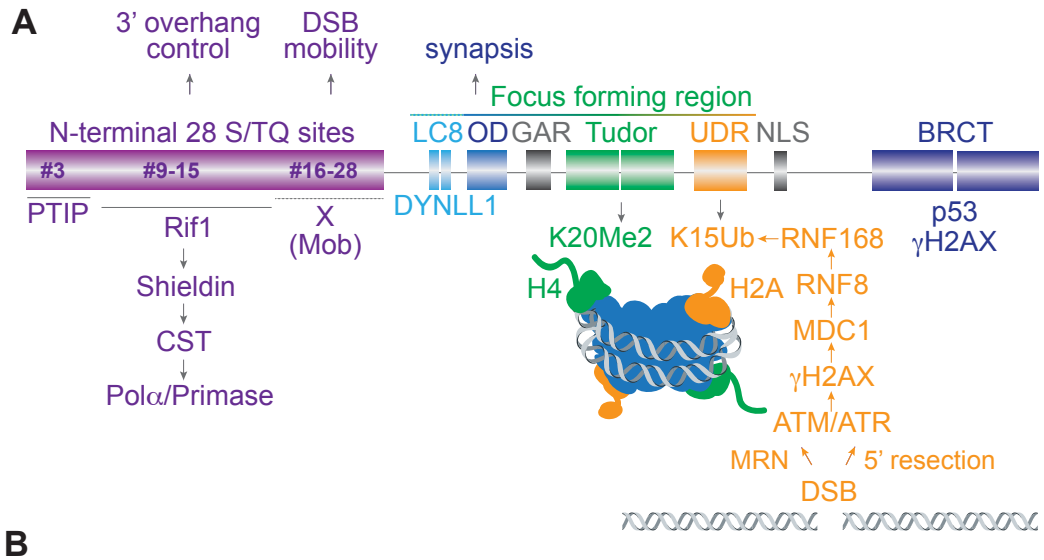

B

Domains required					
PTIP	Rif1 et al.	Mob	LC8	OD	repair context
✔*	✔	✔	✘**	✔	Telomere Fusion
✘	✔	✘	✔	✔	CSR
✔	✔	✔	✔	✔	BRCA1$^{-/-}$ + PARPi

Figure 1.2. Domain structure and function of 53BP1. A, Schematic of human 53BP1. Recruitment of 53BP1 to DSBs requires the Focus Forming Region (FFR), comprising the oligomerization domain (OD), the Glycine-Arginine Rich (GAR) motif, the Tandem Tudor domain, the Ubiquitin-dependent recognition (UDR) motif, and the dynein light chain (LC8) binding domain. The N-terminal S/TQ phosphorylation sites mediate interactions with PTIP, the RIF1/shieldin/CST/Polα/Primase axis, and an as-yet unidentified factor (X) that promotes DSB mobility (Mob). The S/TQ site numbers refer to: #3 (S25); #9-15 (T302, S437, S452, S523, S543, S580, S625); #16-28 (S674, T696, S698, S784, S831, T855, S892, S1068, S1086, S1104, S1148, T1171, S1219)[54]. **B**, Effects of absence of interactions between 53BP1 domains and the indicated interacting partners on c-NHEJ in three contexts. X indicates no requirement; a check mark indicates a requirement. Darker check marks indicate greater dependency. Nuclear localization of 53BP1 and its ability to form foci are required in all three settings; the BRCT domains are not required for any of the three c-NHEJ reactions. *There are conflicting results on the role of PTIP in c-NHEJ of TRF2-deficient telomeres[121, 30, 87]. **The requirement for LC8 in telomere fusions has not been tested in the context of full length 53BP1.

and ubiquitination events leading to recognition of chromatin by the 53BP1 FFR. Phosphorylation of histone H2AX (at S139, termed γH2AX) is followed by recruitment of MDC1[37,38]. Next, two E3 ubiquitin ligases, RNF8 and RNF168, ubiquitinate targets in chromatin surrounding the DSB, including H2AK15[39–44]. The 53BP1 FFR recognizes H2AK15-Ub with its UDR motif[45], while its tandem Tudor domain binds H4K20me2—a mark present throughout the genome[46] (Figure 1.2A). In the absence of DNA damage, the Tudor domain of 53BP1 can associate with TIRR (Tudor-interacting repair regulator; also known as Syndesmos or Nudt16L1), which diminishes the interaction of 53BP1 with H4K20me2[47–50]. TIRR binding is disrupted by DNA damage signaling, improving the ability of 53BP1 to associate with H4K20me2. Thus, upon activation of the DDR two histone marks, H4K20me2 and H2AK15Ub, engage the FFR and lead to 53BP1 accumulation at chromatin proximal to DSBs.

The accumulation of 53BP1 at sites of DNA damage is further stimulated by two domains: the oligomerization domain (OD) and the LC8 domain (Figure 1.2A). The OD mediates homotypic interactions forming 53BP1 dimers and multimers independent of DNA damage signaling[51]. This domain promotes 53BP1 recruitment to IR-induced DSBs[52,53], DSBs formed during CSR[54], and has a (minor) effect on the localization of 53BP1 to damaged telomeres (Figure 1.2B)[30]. The OD also promotes self-assembly of 53BP1 into phase-separated condensates[55]. This feature could explain the 53BP1-mediated synapsis of distal DSBs, which occurs in certain contexts (e.g., V(D)J recombination of distal RAG sites and dysfunctional telomeres, see below). Binding of the LC8 domain to dynein light chain (DYNLL1) can also promote 53BP1 oligomerization and stimulate the recruitment of 53BP1 to sites of DNA damage[56,57].

The functions of the GAR motif and C-terminal BRCT repeats are still elusive as they are not required for DSB repair in the context of BRCA1-deficient cells treated with PARPi, CSR, or dysfunctional telomeres. The 53BP1 BRCT domain can bind to p53[58,59] and recent work showed that 53BP1 enhances the p53-dependent transcriptional changes throughout the genome[60]. 53BP1 BRCT repeats also interact directly with γH2AX[61], but this interaction is not critical for the localization of 53BP1 to sites of DNA damage. However, the C-terminal domain of 53BP1 is important for repair of DSBs in heterochromatin[33].

The critical domain with regard to the effects of 53BP1 on DSB repair is the N-terminal region, which contains 28 S/T-Q phosphorylation sites. These sites are phosphorylated by both the ATM and ATR kinases. ATR is activated by RPA coated along ssDNA together with TopBP1 bound to the 9-1-1 clamp at a nearby 5' ds-ss transition[62]. The ability of 53BP1 to respond to ATR signaling is evident from its localization at telomeres lacking the POT1 component of shelterin, which specifically activate ATR but not ATM signaling[63].

As a result of ATM or ATR signaling, the phosphorylated S/T-Q sites in the N-terminus of 53BP1 interact with three key effector proteins, each of which requires a distinct set of phosphorylated S/T-Q sites (Figure 1.2A). These effectors are 1) RIF1 (homologue of yeast Rap1- interacting factor 1), which governs processing of DNA ends by recruiting shieldin, which in turn binds to a complex composed of CST (CTC1, STN1, TEN1), Polymeraseα, and primase; 2) Pax2 transactivation domain-interacting protein (PTIP), the function of which remains elusive; and 3) an as-yet unidentified factor that

promotes the mobility of DNA ends. The contribution of these factors varies depending on the context of the DSBs being repaired as discussed in detail below.

1.4 cNHEJ of telomeres lacking TRF2

The joining of dysfunctional telomeres was the first of the three specialized cNHEJ contexts where a striking dependency on 53BP1 was observed[64]. Telomeres are protected by the six-subunit shelterin complex, which represses DNA damage signaling, DNA repair, and 5' end hyper-resection (Figure 1.3A)[65]. Shelterin is highly compartmentalized such that different DDR pathways are activated at telomeres depending on which shelterin subunit is removed. When TRF2 is deleted from mouse cells, telomeres activate the ATM kinase signaling cascade, in a manner dependent on the MRN complex[63,66–69] and the telomeres are joined by KU70/80- and LIG4- dependent cNHEJ[66,70]. TRF2 remodels telomeres into the t-loop and it is thought that the occlusion of the chromosome end in this structure denies MRN and KU70/80 access to the telomere terminus, thereby preventing activation of ATM and blocking cNHEJ[71,72] (Figure 1.3B). Remarkably, absence of 53BP1 (or its upstream regulators ATM, MDC1, and RNF8[63,67,73,74]) decreases the rate of telomere fusion to the same extent as LIG4 deficiency. This is due to several separable effects of 53BP1: the promotion of chromatin mobility; an effect of the oligomerization domain that may involve telomere clustering; and a somewhat mysterious third function involving RIF1/shieldin/CST (Figure 1.2B and Figure 1.3C).

Most of the cNHEJ of telomeres lacking TRF2 occurs in G1, resulting in chromosome-type telomere fusions in metaphase after replication of the fused chromosomes (Figure 1.3C). Chromatid-type telomere fusions, which indicate that cNHEJ took place after DNA replication, are observed but are notably less frequent. In

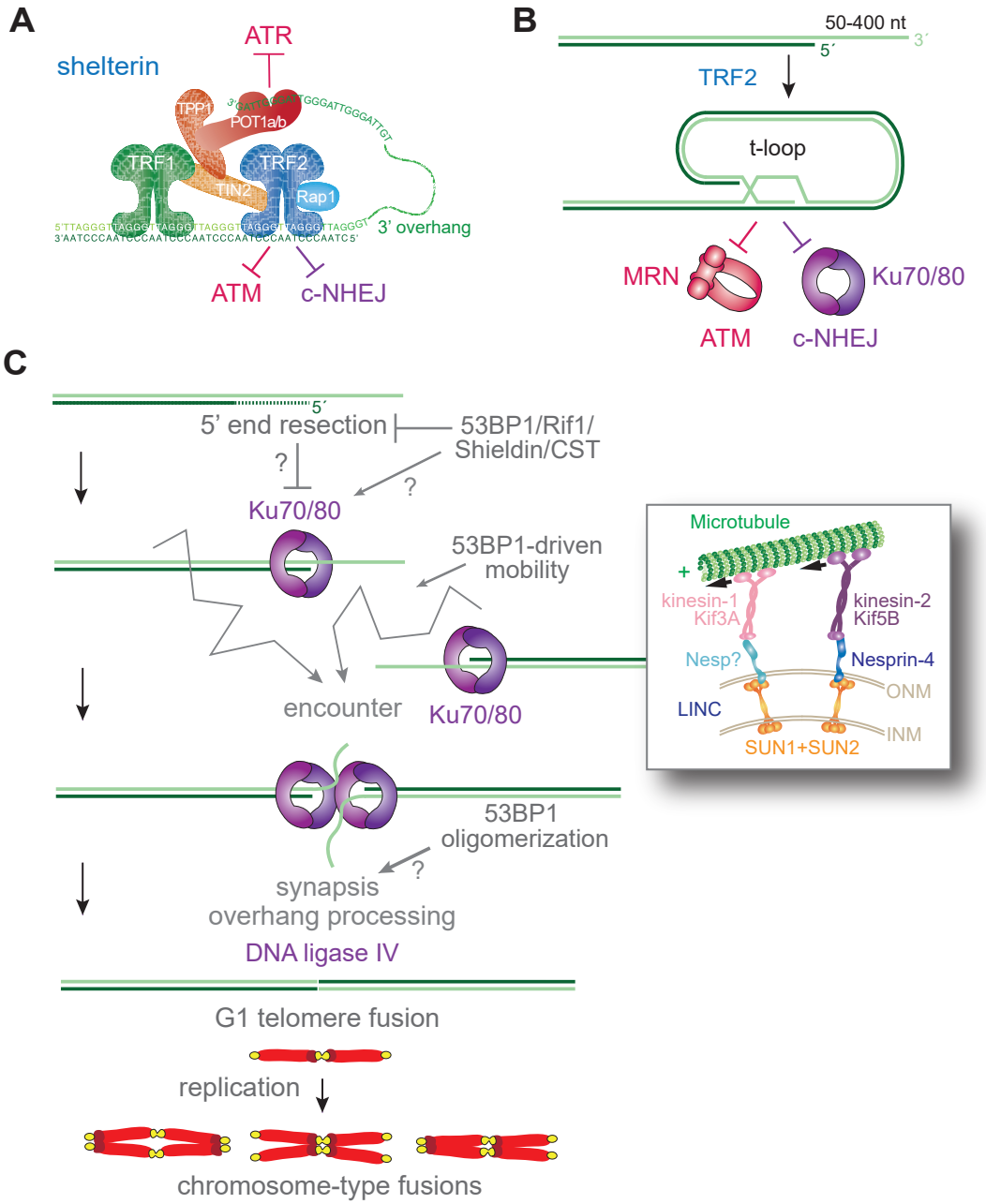

Figure 1.3. 53BP1-dependent c-NHEJ of telomeres lacking TRF2. A, The six-subunit shelterin complex protects telomeres from DNA damage signaling and DSB repair. **B,** TRF2 in shelterin mediates formation of the protective t-loop by promoting strand invasion of the telomeric 3' overhang into duplex telomeric DNA. T-loops are proposed to hide the telomere end from the MRN complex and KU70/80, thereby avoiding initiation of ATM signaling and c-NHEJ. **C,** Mechanisms by which 53BP1 promotes c-NHEJ mediated fusion of telomeres lacking TRF2. Top: The RIF1/shieldin/CST axis promotes telomere fusions. As discussed in the text, the underlying mechanism is unclear. It could involve counteracting 5' end resection or a more direct mechanism of enhancing c-NHEJ. Middle: 53BP1-driven mobility is proposed to increase the chance that two telomeres (which are distributed throughout the nucleus) can encounter each other and fuse. The inset shows the involvement of the LINC complex and cytoplasmic microtubules in the 53BP1-dependent mobility. Bottom: 53BP1-dependent oligomerization and synapsis may further promote the fusion of telomeres that have become closely apposed. Telomere fusions after TRF2 deletion occur predominantly in G1, and after DNA replication are visible as chromosome-type fusions in metaphase spreads.

G1, deprotected telomeres behave like one-ended DSBs, analogous to a reversed replication fork in S phase. Since telomeres are distributed throughout the nucleus, telomere-telomere fusion in G1 requires that deprotected telomeres migrate in the nucleus until they encounter a fusion partner.

Telomere-telomere fusion in G1 is stimulated by the ability of 53BP1 to promote the mobility of deprotected telomeres (Figure 1.3C). Telomeres that have lost TRF2 become more mobile and roam larger territories than functional telomeres, presumably increasing the chance that they encounter one another[64]. While the effect of 53BP1 on chromatin mobility was first identified in the setting of deprotected telomeres, 53BP1 also promotes the mobility of IR-induced DSBs[75]. The underlying mechanism of this dynamic behavior involves a specific set of S/T-Q sites in 53BP1 (Figure 1.2A), microtubule dynamics, kinesins, as well as nesprins and the transmembrane SUN1 and SUN2 proteins in the LINC (Linker of Nucleoskeleton and Cytoskeleton) complex[75] (see insert in Figure 1.3C). The S/T-Q interacting partner(s) involved in promoting the

mobility of damaged chromatin has not been identified and there is no known protein-protein interaction that links 53BP1 to the LINC complex. The interactions of 53BP1 with PTIP or RIF1 are not required for this function, and neither are the LC8, OD, and BRCT domains[27,75].

When deprotected telomeres persist for a long time (days), as is the case in cNHEJ-deficient (*Lig4*$^{-/-}$) cells, a 53BP1-dependent process causes them to become clustered[76]. This phenotype may reflect the ability of 53BP1 to hold different sites of DNA damage together (synapsis) in what may be a phase-separated compartment[55]. This clustering has also been observed with genome-wide DSBs[77]. In the context of V(D)J recombination, the synapsis function of 53BP1 is needed for cNHEJ of RAG-induced DSBs, but only when the DSBs are at a great distance[29]. Interestingly, deletion of the OD domain, which has been implicated in synapsis in V(D)J recombination, also diminished the rate of telomere fusions[30] (Figure 1.3C).

The third manner in which 53BP1 promotes telomere fusions involves the RIF1/shieldin/CST axis (Figure 1.3C), pointing to some structural modification or protection of the telomere end. Telomeres, including those lacking TRF2, contain a sizeable 3' overhang with a minimal length of 50 nt and reaching as long as 400 nt. In mouse cells lacking TRF2, this overhang is removed during cNHEJ and this processing is strictly dependent on KU70/80 and LIG4[66,78] (Figure 1.3C). The nuclease(s) involved in 3' overhang removal have remained elusive although MRE11 is a candidate[69]. Given that overhang processing is coupled to cNHEJ, the initial presence of this ssDNA is clearly not an impediment to the binding of KU70/80 to deprotected telomeres.

When TRF2 is inhibited with a dominant-negative (DN) allele that prevents endogenous TRF2 from binding to telomeric DNA, the situation is different. For unknown reasons, the fusions induced by the TRF2-DN allele primarily take place after DNA replication (in S/G2), giving rise to chromatid-type fusions in metaphase[79]. In this setting, overhang removal takes place prior to the initiation of cNHEJ[79], suggesting that in G2, KU70/80 only acts on telomere ends lacking ssDNA[80]. The explanation for the inhibitory effect of telomeric overhangs in S/G2 is likely found in CYREN/MRI[10]. This small KU70-binding protein inhibits the ability of KU70/80 to act on DSBs with 3' or 5' protrusions. If CYREN/MRI only exerts this effect in S/G2, it could explain the cell cycle-dependent effect of the telomeric 3' overhang on cNHEJ. The issue is slightly complicated by the fact that CYREN/MRI also acts as a positive regulator of cNHEJ in G1[11]. Nonetheless, there is evidence that in S/G2, the XPF/ERCC1 flap endonuclease is required for the removal of the 3' overhang prior to the initiation of cNHEJ[80]. This role for XPF in telomere fusions is consistent with CYREN/MRI inhibiting cNHEJ at DSBs with overhangs in S/G2.

An important consideration regarding the cNHEJ of dysfunctional telomeres in G2 is the mechanism of telomere end processing after DNA replication (Figure 1.4). As telomeres require a 3' overhang for t-loop formation and thus for their protection, this structure needs to be regenerated at both sister telomeres. The sister telomere generated by leading-strand DNA synthesis (referred to as the leading-end telomere), is first processed by Apollo, a TRF2-bound nuclease, to yield a short overhang which may be akin to the product of MRN/CtIP at DSBs[81,82]. Next, both sister telomeres are extensively resected by EXO1, resulting in extended overhangs[83]. If not counteracted,

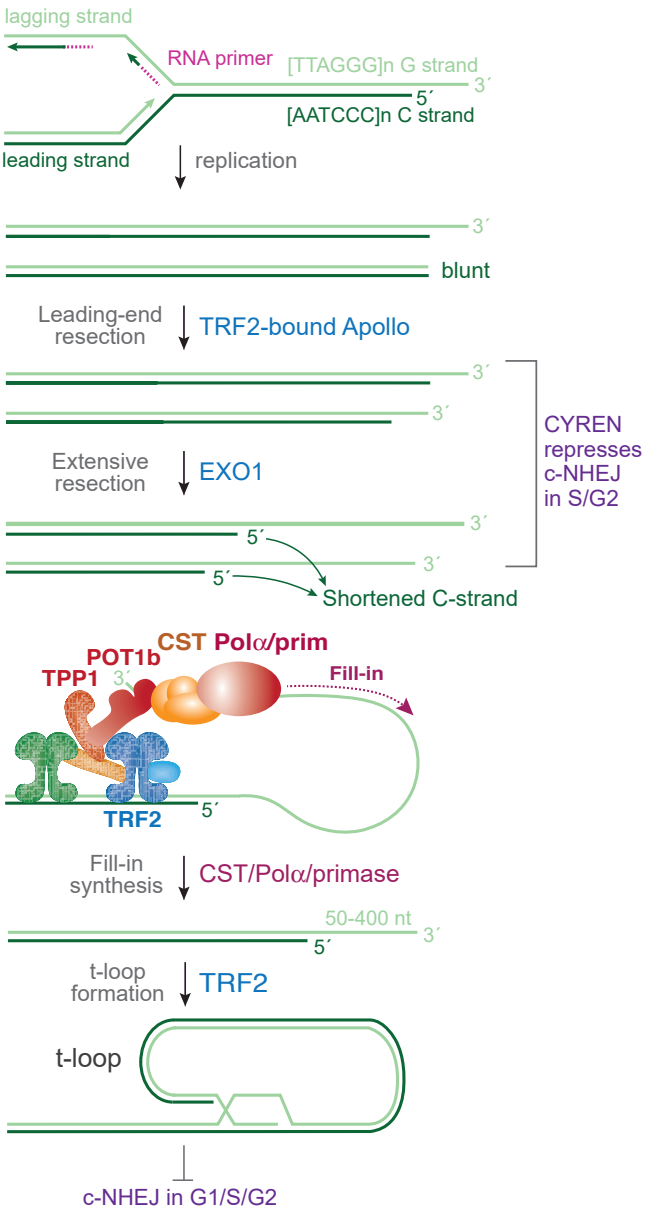

Figure 1.4. Mechanism of telomere end processing after DNA replication. Telomeres generated by lagging-strand synthesis are assumed to have a short 3' overhang after RNA primer degradation, while telomeres generated by leading-strand synthesis are initially blunt. Processing by TRF2-bound Apollo results in short 3' overhangs at leading telomeres, such that both telomere types are substrates for further resection by EXO1. If not counteracted, C-strand attrition due to EXO1 leads to telomere loss. The TPP1/POT1 heterodimer in shelterin recruits the CST/Polα/primase complex to fill-in the resected ends, resulting in a moderately sized (50-400 nt) 3' overhang that is competent for strand-invasion and t-loop formation.

this hyper-resection of the 5' ends can lead to truncated telomeres[84–86]. Such telomere loss is avoided by a final step where the POT1/TPP1 components of shelterin recruit CST/Polα/primase to mediate fill-in of hyper-resected ends[83]. This process creates telomeres with moderately-sized 3' overhangs that can form t-loops.

When TRF2 is deleted from telomeres in cells lacking RIF1, the telomeric overhangs become 2-fold longer and the rate of telomere fusions is diminished by approximately half[27]. A similar effect is observed when shieldin or CST is depleted[35,87–92]. One interpretation of this result is that the longer overhangs are an impediment to KU70/80 loading (Figure 1.3C). However, most telomere fusions studied in these experiments take place in G1 when KU70/80 is not repressed by CYREN/MRI. Why would a doubling of the overhang length (i.e., from 50-400 nt to 100-800 nt) inhibit cNHEJ? Perhaps KU70/80 is particularly sensitive to a doubling of the overhang length, or perhaps the longer overhangs form secondary structures (e.g., G4 structures) and/or bind proteins that impede cNHEJ. Another possibility is that it is not the length of the overhang that affects the repair outcome but rather the presence of the shieldin/CST/Polα/primase complex on the telomeric overhang. Perhaps the shieldin/CST/Polα/primase complex blocks proteins (e.g., RAD51 or RAD52) that can compete with cNHEJ factors. The presence of CST at telomeres is known to block telomerase[93,94] so this type of inhibitory effect is not unprecedented. Further work on the effect of long overhangs at dysfunctional telomeres and other DSBs on cNHEJ in G1 is needed to resolve these issues.

1.5 cNHEJ of AID-induced DSBs in class switch recombination

CSR is a programmed recombination in the immunoglobulin locus that allows B cells to switch between different classes of antibodies (Figure 1.5A)[95]. This remarkable process involves KU70/80-, DNAPKcs-, LIG4-, and XRCC4/XLF-dependent cNHEJ repair of DSBs generated in the Switch regions. Switch regions are positioned in the introns preceding exons that encode the various classes of immunoglobulin heavy chains. Transcription of the highly repetitive, GC-rich Switch regions is required for CSR. In CSR, the repair of DSBs by cNHEJ is unusual in that they are far apart (20-600 kb). For CSR to occur, DSB repair needs to create deletions, rather than non-productive intra-Switch DSB repair (or inversions) (Figure 1.5A).

The DSBs required for CSR are generated by Activation-Induced Deaminase (AID), a member of the family of APOBEC cytosine deaminases (Figure 1.5B). AID deaminates cytosine in ssDNA to uracil, which is converted to a strand break after uracil removal by uracil DNA glycosylase (UNG) and cleavage of the resulting abasic site by the BER nuclease APE1. Cytosine deamination takes place on both the template and non-template strands[96] so that closely positioned nicks on opposite strands can result in DSBs. In addition, recognition of the U:G mismatch by the Mismatch Repair (MMR) MSH2/6 complex and subsequent exonucleolytic attack by EXO1 on nicks on the opposing strand (perhaps generated by APE1) appears to enhance DSB formation in CSR[95,97]. The DSBs formed through this process are predicted to contain either 5' or 3' overhangs of variable lengths (Figure 1.5B). As CSR takes place in G1[98] when CYREN/MRI is not inhibitory to cNHEJ[10], KU70/80 should be able to act on DSBs

despite the presence of 5' and 3' overhangs. Some overhang processing will be needed during cNHEJ, but the nucleases involved are not yet known.

CSR has been a great tool for dissecting the functions of 53BP1. In the absence of 53BP1, CSR is severely impaired and the recombination in the Ig locus shifts to intra-Switch repair events that are accompanied by extensive resection[99–101]. Two distinct aspects of 53BP1 promote CSR (Figure 1.2B and Figure 1.5). First, CSR requires the ability of 53BP1 to form stable oligomeric assemblies at sites of DNA damage. This attribute is dependent on the cooperation of the two LC8 motifs with the OD[30,54,57,102]. The LC8 motifs, through their interaction with DYNLL1, promote oligomerization *in vitro* and enhance the stability of 53BP1 at sites of DNA damage. The LC8 motifs alone are insufficient and CSR requires the simultaneous oligomerization of 53BP1 through its OD[57]. The most likely explanation for CSR dependence on higher order 53BP1 assemblies is that distal DSBs need to be held in proximity for a productive cNHEJ event (Figure 1.5A).

The second main determinant of 53BP1-promoted CSR is found in RIF1/shieldin/CST (Figure 1.5B). Loss of any one of these components or failure of 53BP1 to bring these factors to DSBs reduces CSR[28,87–92,103–105]. Molecular analysis of the few CSR products formed in the absence of RIF1/shieldin/CST shows that there is extensive resection[28,104,105]. The requirement for RIF1/shieldin/CST in CSR is paradoxical since CSR takes place at DSBs that already carry various ssDNA

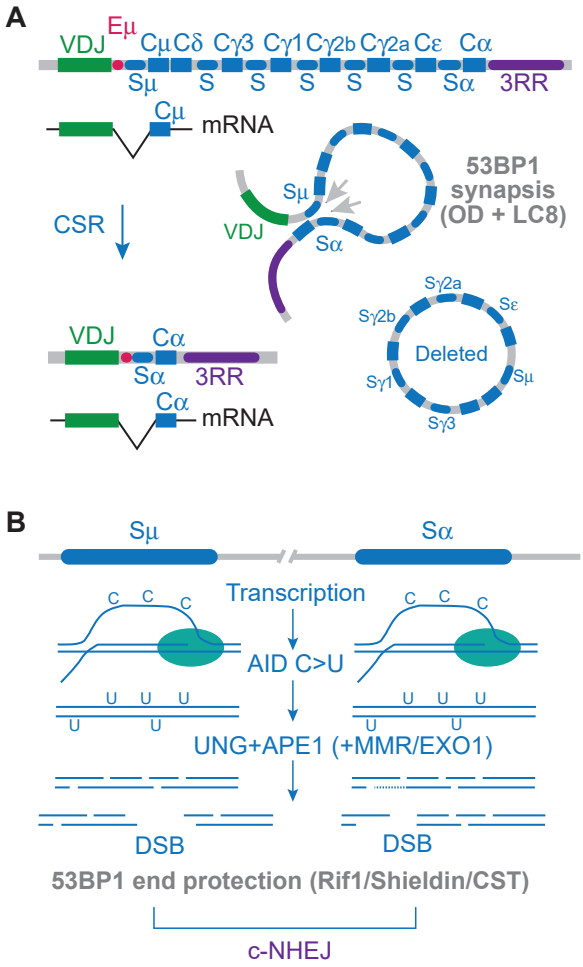

Figure 1.5. The role of 53BP1 in class switch recombination (CSR). A, Schematic of immunoglobulin locus. Rectangles represent exons and ovals represent Switch regions in the introns. In this example AID creates DSBs in Sμ and Sα leading to a switch of Cμ to Cα. The synapsis function of 53BP1 contributes to the proximity of the DSBs. **B,** Mechanism of DSB formation in CSR. Transcription of the Switch regions creates the ssDNA substrate for AID-mediated cytosine deamination. The resulting uracil residues are processed by Base Excision Repair (BER) and Mismatch Repair (MMR) resulting in frequent nicks that can lead to DSB formation. These DSBs can carry 5' or 3' overhangs and require the RIF1/shieldin/CST axis of 53BP1 for efficient joining. As is the case for telomere fusions, the exact role of RIF1/shieldin/CST is not clear (see text).

protrusions. Why then, are proteins involved in minimizing 3' overhang length needed?

This question is analogous to that posed above in the context of telomere fusions where

RIF1/shieldin/CST promote cNHEJ despite the fact that 3' overhangs do not inhibit cNHEJ. Of particular interest is the observation that the shieldin complex co-evolved with CSR[89]. This suggests that shieldin is a relatively recent elaboration of the 53BP1 repertoire that has evolved to facilitate CSR.

1.6 cNHEJ of DSBs in PARPi-treated BRCA1-deficient cells

The context of 53BP1 action that has strongly influenced current models of 53BP1 function is that of BRCA1-deficient cells treated with PARP1 inhibitors. BRCA1 plays a critical role in HDR at multiple steps[12]. BRCA1 is proposed to facilitate 5' end resection and promotes the loading of RAD51 by BRCA2. Together with a role in protecting replication forks[106], the requirement for BRCA1 in HDR is thought to underlie the etiology of BRCA1-deficient cancers. Seminal work revealed that cells deficient in BRCA1 are highly sensitive to PARPi[107,108] and this is now being exploited clinically[109–111].

PARP1 is required for the repair of single-stranded breaks (SSBs) that result from oxidative damage and are formed during BER [112,113], a pathway that removes thousands of aberrant nucleotides per genome each day (Figure 1.6A). PARP1 binds to and is activated by SSBs. Once active, PARP1 will promiscuously PARsylate chromatin constituents resulting in a local network of branched PAR chains. PAR functions to recruit XRCC1, Polymeraseβ and Ligase 3, which repair the SSB. PARP1 also PARsylates itself, allowing the enzyme to evacuate the lesion. When PARP1 activity is inhibited, PARP1 can become locally trapped at the break, preventing further repair [114,115]. The resulting lesions, with or without trapped PARP1, generate DSBs and/or

impede fork progression during DNA replication, but the trapping of PARP1 is thought to be the major source of the effect of PARPi on BRCA1-deficient cells (Figure 1.6B).

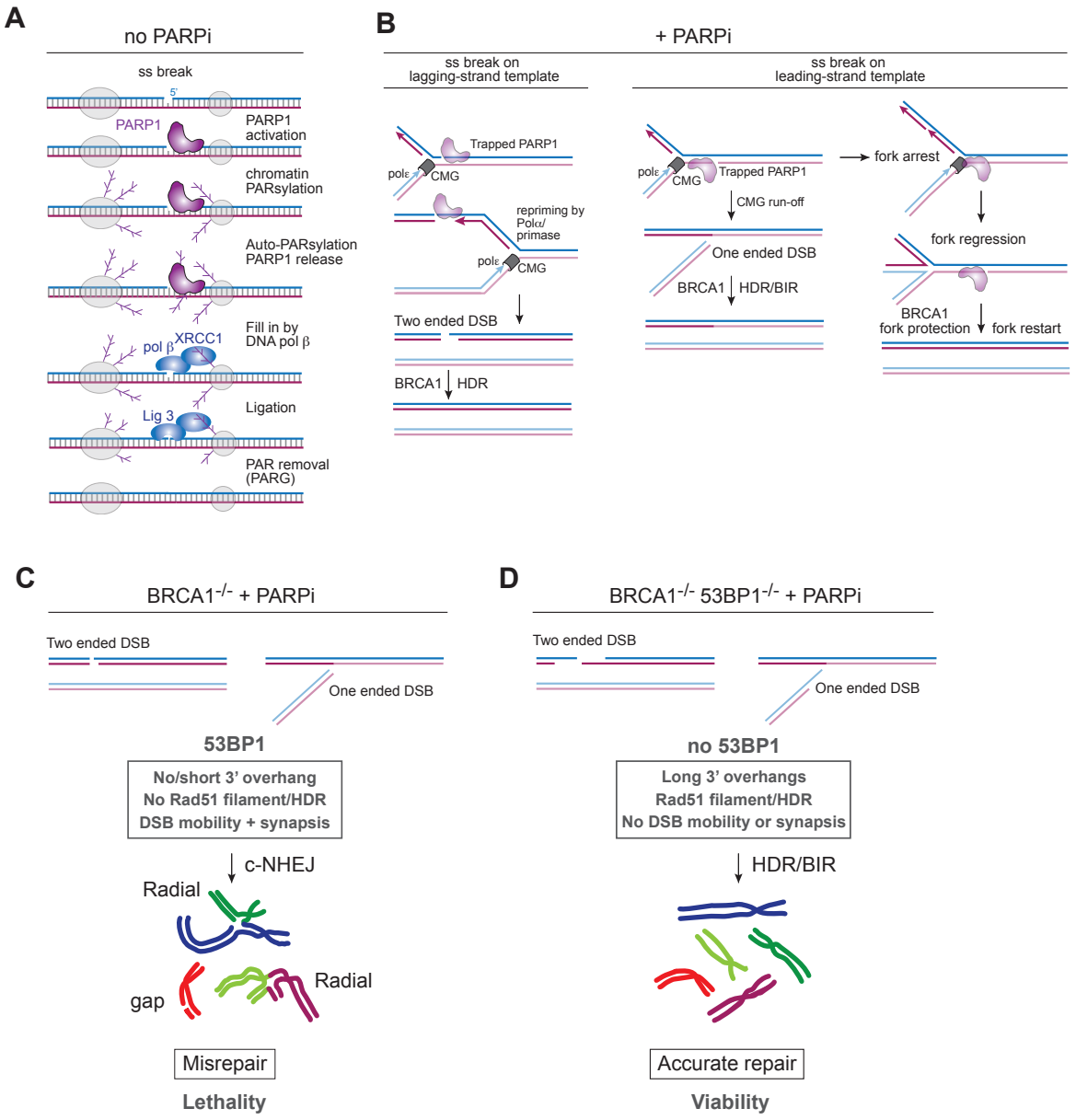

Figure 1.6. Mechanism of action for PARPi and genetic interaction with BRCA1. **A,** The role of PARP1 in recognition and repair of SSBs. **B,** The effects of PARPi on SSBs on lagging- or leading-strand template during DNA replication. "PARP-trapping" occurs when PARP1 remains bound to the SSB due to inhibition of its autoPARsylation activity by PARPi. **C,** The effects of simultaneous disruption of BRCA1 and PARP1. In the absence of BRCA1-mediated HDR, 53BP1 mediates misrepair of broken chromosomes, leading to cellular death. **D,** Concurrent loss of 53BP1 restores HDR, leading to resistance to PARPi in BRCA1-deficient cells.

When a replication fork encounters an SSB, several outcomes are possible (Figure 1.6B). If the lesion is on the lagging-strand template, a two-ended DSB may result after re-priming by Polα[116]. If the leading-strand template has an SSB, no bypass is possible and a one-ended DSB will be formed. Both types of DSBs require HDR for precise repair and therefore depend on BRCA1. In BRCA1-deficient cells, some of the two-ended DSBs may be repaired by cNHEJ without impairing cell viability. However, cNHEJ of one-ended DSBs can give rise to aberrant repair products as can mis-rejoining of two-ended DSBs. Specifically, if a DSB (one- or two-ended) becomes ligated to a DSB on another chromosome, a lethal type of chromosome aberration is formed (Figure 1.6C). These aberrant joining events are evident in metaphase chromosome spreads where they are visible as multi-armed mis-rejoined chromosomes, often referred to as “radial chromosomes”. [Note: “radial chromosomes” has become an accepted term to refer to triradial and quadriradial chromosomes which have chromosome arms extending into three or four rather than the regular two opposing directions; see for instance[117]]. Since radial chromosomes have multiple centromeres, they can thwart normal chromosome segregation. Cells harboring radial chromosomes attempt to undergo cell division but succumb to some form of mitotic catastrophe and show hallmarks of mitotic dysfunction including anaphase bridges and micronuclei[118]. Lack of proper repair of the PARPi-induced DSBs is also evident from gaps and breaks in metaphase chromosomes (Figure 1.6C).

As is the case with dysfunctional telomeres and CSR, several aspects of 53BP1 conspire to promote PARPi-sensitivity of BRCA1-deficient cells (Figures 1.2B and 1.6). First, formation of radial chromosomes requires that a DSB on one chromosome

reaches a DSB on another. It is therefore not surprising that the ability of 53BP1 to promote the mobility of DSBs contributes to the sensitivity of BRCA1 deficient cells to PARPi[75], as does the synapsis function of 53BP1[54]. The second mechanism by which 53BP1 promotes PARPi sensitivity involves the RIF1/shieldin/CST/Polα/primase axis. When this function of 53BP1 is disabled, BRCA1-deficient cells regain their ability to repair PARPi-induced DSBs by HDR and survive[27,35,88–92,103–105,119,120] (Also, see Chapter 3 of this thesis). The proposed mechanism for this re-activation of HDR is discussed below.

A factor whose contribution remains unclear is PTIP. Deletion of PTIP rescues the formation of PARPi-induced radials and lethality in BRCA1-deficient cell lines[106,121,122]. This presents a conundrum since 53BP1 clearly also mediates the effects of PARPi through promoting DSB mobility and synapsis as well as through RIF1/shieldin/CST/Polα. There is no cross-talk between PTIP and either RIF1 or the induction of DSB mobility that can explain the discrepancy. In addition, some of the effects of PTIP in BRCA1-deficient cells do not appear to require its interaction with 53BP1[106]. Indeed, an allele of 53BP1 that does not bind PTIP continues to promote radial formation and lethality in PARPi-treated BRCA1-deficient cells unless the RIF1/shieldin axis is also absent[123]. Perhaps once the mechanism by which PTIP promotes PARPi-induced radials and lethality is known, it will become clear why deletion of PTIP has the same effect as deletion of 53BP1.

In addition to formation of DSBs, trapping of PARP1 at SSBs could create a barrier to replication that results in fork arrest (Figure 1.6B). The contribution (if any) of these PARPi-induced fork stalling events to the formation of radials and accompanying

lethality is not known. However, it is noteworthy that in hydroxyurea (HU)-treated cells, the stability of arrested forks requires BRCA1[106,124–127]. In the absence of BRCA1, a small percentage of HU-induced fork arrests are processed into chromosomal aberrations. BRCA1 blocks degradation of arrested forks by MRE11[125], which is recruited there by PTIP[106]. However, in this context PTIP acts independently of 53BP1, and 53BP1 itself has no effect of the outcome of HU treatment in BRCA1-deficient cells [106]. Therefore, it remains unclear how the events induced by HU relate to those induced by PARPi.

An additional point of consideration is the mutually antagonistic relationship between BRCA1 and 53BP1 that affects each factor's accumulation near DSBs. Independently of BRCA1, the presence of 53BP1 at DSBs is down-modulated in S phase such that there are fewer and/or less extensive sites of 53BP1 accumulation in newly-replicated chromatin where the H4K20Me marks are diluted[128,129]. In G2, 53BP1 foci regain their prominence[130]. In addition, BRCA1 changes the nature of 53BP1 foci in S phase, converting them from homogeneous domains into more hollow spheres, suggesting that BRCA1 has the ability to relegate 53BP1 to the outskirts of the DDR-marked chromatin[103,131,132]. Conversely, 53BP1 appears to minimize the accumulation of BRCA1 at DSBs in G1 in a manner that involves RIF1 and the REV7 component of shieldin[27,103,119,130]. Recent high-resolution imaging of DNA damage foci reveals a complex architecture with different domains occupied by BRCA1, 53BP1, and RIF1 [132]. Interestingly, 53BP1 and RIF1, but not shieldin, are involved in stabilizing damage-proximal chromatin into globular subdomains within DNA damage foci [132]. The

mechanism of the mutual antagonism between 53BP1 and BRCA1 may emerge from further dissection of this interplay.

1.7 Two models for the role of the RIF1 axis

Concerning the mechanism by which 53BP1 limits the formation of ssDNA at DNA breaks, there are two main models (Figure 1.7) [35,89,91,92,105,120,133–136]. In the first model, 53BP1 uses the loading of shieldin onto the ssDNA to protect the 5' end from resection (Figure 1.7A). The finding that SHLD2 alone or in complex with SHLD1 can bind to ssDNA is promising in this regard [91,92,120,135], but it remains to be seen whether shieldin binds sufficiently close to the 5' end to form a barrier to nucleolytic attack. For shieldin to block resection upon engaging the DNA end, at least some ssDNA must already be present. The length of this 3' overhang is not yet clear since the minimal binding site of the whole shieldin complex has not been determined. *In vitro*, SHLD2/SHLD1 complexes bind to oligonucleotides of 60-100 nt[91,92,120,135].

Assuming there is sufficient ssDNA for shieldin to bind at the DSB, how would it prevent additional resection? Perhaps shieldin simply hides the 5' end from nucleases. A second possibility is that shieldin terminates EXO1 resection in the same way that loading of RPA on 3' overhangs inhibits further resection by EXO1[137–141]. In addition, resection by DNA2 in conjunction with either WRN or BLM could be inhibited if shieldin prevents the loading of RPA, which normally stimulates these RecQ helicases[20]. Even though shieldin is much less abundant than RPA and has a lower affinity for ssDNA, it might effectively outcompete RPA due to its tethering to 53BP1. The same principle of local tethering allows POT1, the ssDNA-binding protein in shelterin, to outcompete the

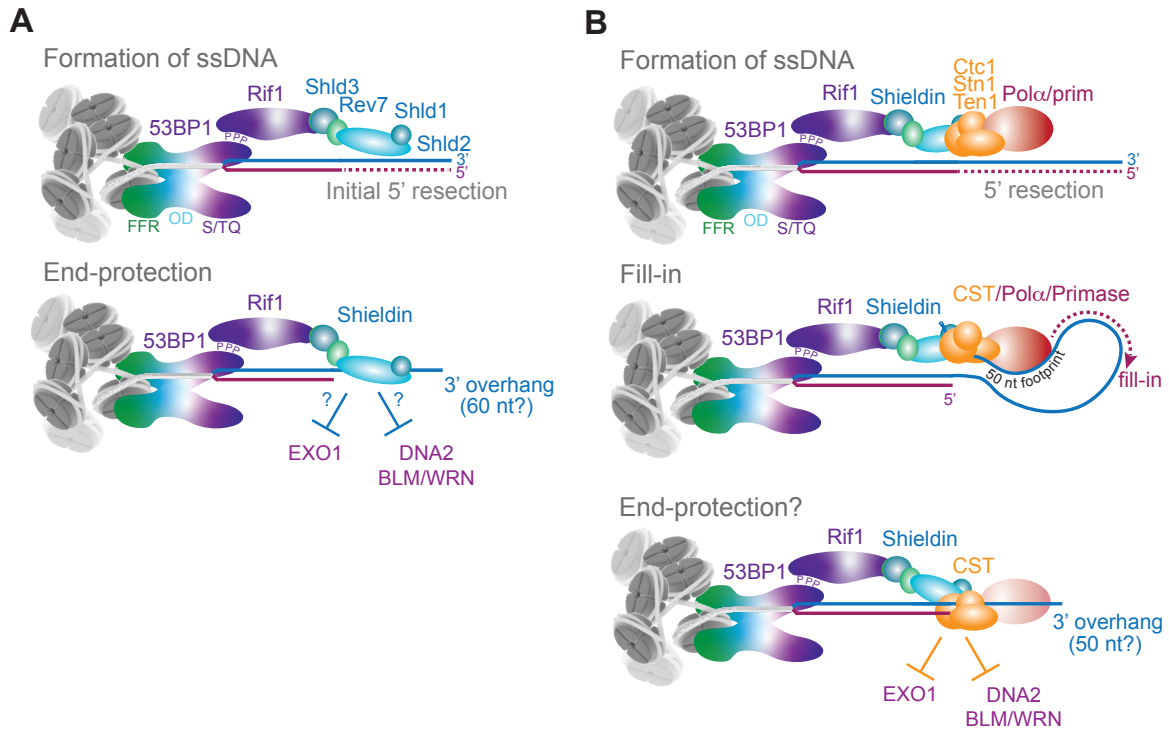

Figure 1.7. Two models for the role of the RIF1 axis. A, End protection by the ssDNA-binding shieldin complex limits resection by EXO1 and BLM/WRN/DNA2. **B,** shieldin recruits CST/Polα/Primase, executing a fill-in reaction to counteract resection. This model is also compatible with an additional step of end protection by shieldin/CST after fill-in. Note that in both models, initial 5' end resection occurs to allow ssDNA binding by shieldin and CST, and a moderately-sized (~50 nt) 3' overhang is predicted to remain.

more abundant RPA[142]. It has also been suggested that instead of or in addition to blocking resection, shieldin could promote removal of the 3' overhang by the structure-specific nuclease ASTE1[143]. However deletions are predicted to occur if resection and overhang trimming preceded cNHEJ.

In the second (not mutually exclusive) model, shieldin functions to recruit CST/Polα/primase (Figure 1.7B). The recruitment of CST/Polα/primase could affect the structure of the DNA in two ways. First, CST is known to bind with high affinity to ds-ss junctions[144], potentially allowing the complex to protect 5' ends from EXO1 and block

access of the BLM and WRN helicases. As is the case with shieldin, CST binding at a DSB will require a 3' overhang (for CST, in the range of 10-18 nt[144]). CST tends to favor sequences with runs of G residues[145] (as in the telomeric TTAGGG or the G-rich Switch regions in the immunoglobulin locus) which would restrict its binding opportunities in short 3' overhangs. It is also possible that the CST binding specificity is altered when it is bound to shieldin, allowing it to engage overhangs without G runs. These possibilities are discussed in more depth in Chapters 3-5.

In addition to CST simply protecting the 5' end from resection activities, CST could counteract resection (Figure 1.7B). CST is known to promote Polα/primase activity[146–148], allowing fill-in synthesis to occur. This fill-in is relevant to the outcome of PARPi-treatment of BRCA1-deficient cells. Inhibition of Polα or primase leads to a reduction in radials formed after PARPi treatment[35] (see also Chapter 3). Furthermore, BrdU incorporation can be detected at DSBs and this DNA synthesis is dependent on 53BP1, shieldin, CST, Polα, and primase (Chapter 3). Polα has limited processivity and usually synthesizes ~20-25 nt[149]. During canonical DNA replication, these products are extended by Polδ, but whether Polδ is involved at DSBs is unknown. Perhaps repeated fill-in steps by Polα can convert long overhangs into dsDNA.

The CST/Polα/primase fill-in reaction is predicted to leave a considerable 3' overhang because of the removal of the RNA primer and the inability of Polα to copy the region where CST (and shieldin) is bound. The residual overhang left by this 'footprint' may be as long as 50 nt. It has been recently suggested that primase-mediated fill-in synthesis may start at or very near the tip of a 3' overhang[150], but this idea requires more biochemical and structural validation. At telomeres, where CST plays an

analogous role in counteracting resection, the fill-in reaction indeed allows retention of overhangs of at least 50 nt[83,151–153]. If CST also has the ability to protect 5' ends from further resection, the outcome would be DNA ends with overhangs of up to 50 nt but not much longer (Figure 1.7B).

Regardless of the mechanism by which the RIF1/shieldin/CST axis acts, a DSB that is acted upon by 53BP1 is predicted to carry a 3' overhang. According to these considerations, 53BP1 does not actually prevent the formation of 3' overhangs. Rather, 53BP1 appears to prevent the formation of 3' overhangs that are *overly long* (greater than 50 nt in the CST model; perhaps as long as 60 nt in the shieldin model).

1.8 The 53BP1 dilemma

The selective advantage of 53BP1 is an enigma because most of its described functions are not obviously beneficial. 53BP1 cannot have evolved solely to promote CSR since it was present long before the innovation of CSR in the adaptive immune system[89]. Obviously, 53BP1 also did not evolve to mediate telomere fusions or make BRCA1-deficient cells sensitive to PARPi. Furthermore, several of 53BP1's attributes are potentially disastrous for cells with multiple DSBs. The propensity of 53BP1 to hold together and/or cluster DSBs that are at a distance is expected to promote translocations with potential cancer-causing consequences. Similarly, promoting the mobility of DSBs is expected to engender mis-repair.

And what is the purpose of 53BP1's ability to limit the extent of ssDNA at DSBs? It has been argued[2,3] that this function of 53BP1 is needed for the control of DSB repair, directing DSBs away from HDR and towards cNHEJ in G1. However, if 53BP1 limits

resection by loading shieldin (with or without CST) on the ssDNA, the ssDNA occupied by shieldin/CST would be removed during the subsequent cNHEJ[143]. This is also true if overhangs were removed by ASTE1 downstream of shieldin[143]. It seems difficult to argue that 53BP1 has evolved to promote a form of cNHEJ that is always accompanied by deletions. Such a system would only make sense in the context of CSR where small deletions are not detrimental. Furthermore, the danger of HDR in G1, and hence the need for 53BP1 to shuttle DSBs into cNHEJ, is limited. For instance, BRCA2 does not accumulate at sites of DNA damage before entry into S phase, even in the absence of 53BP1[154], and initiation of resection by MRN/CtIP is under cell cycle control[14,155].

In summary, 53BP1 prevents formation of long 3' overhangs at DSBs and alters DSB dynamics in a manner that could promote translocations. These potentially detrimental attributes of 53BP1 may be best understood as a mechanism to ensure the fidelity of DSB repair rather than a mechanism to channel DSBs into cNHEJ at the expense of HDR.

1.9 Speculation: 53BP1 as a DSB escort that promotes repair fidelity and CSR

The considerations above led us to speculate that the selective advantage of mammalian 53BP1 resides in its ability to block illegitimate recombination. We further speculate that several of the current-day attributes of 53BP1 co-evolved with CSR. The first aspect of 53BP1 that can improve the fidelity of DNA repair is its ability to mobilize DSBs. It has previously been argued[75] that DSB mobility is a mechanism to counteract ectopic recombination of DSBs (Figure 1.8A). In this view, 53BP1 could disengage DSBs that have lost their proximity to the sister chromatid and are at risk of invading

homologous (e.g., repetitive) sequences at another locus. Processes such as cohesin-mediated loop extrusion and torsional stress induced by transcription could be the source of disengaged DSBs that would need 53BP1-driven mobility to re-join their

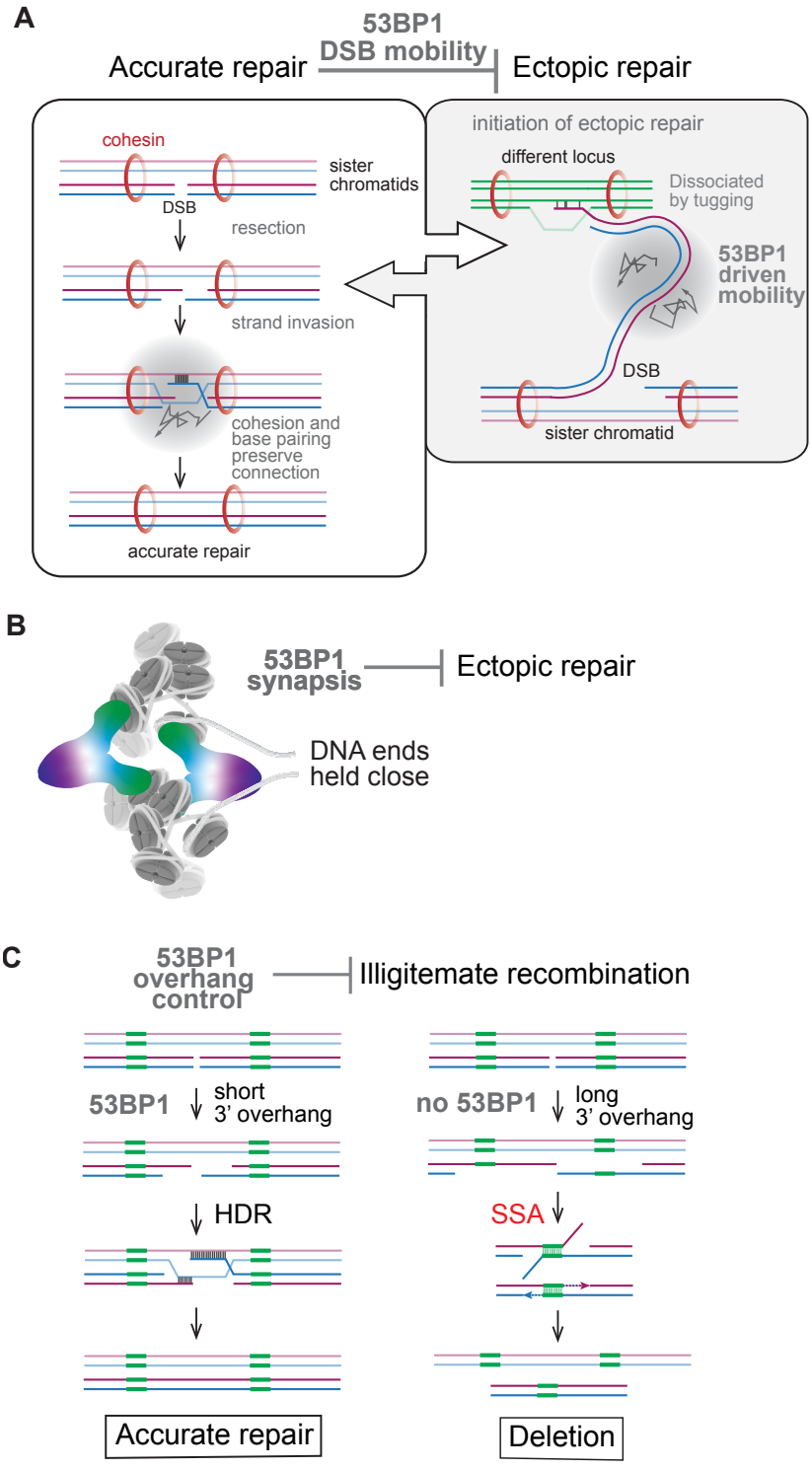

Figure 1.8. Model for 53BP1 as a DSB escort that promotes repair fidelity and CSR. A, 53BP1-driven mobility of chromatin containing a DSB is proposed to discourage ectopic repair. S phase DSBs are preferentially repaired by HDR using the sister chromatid (left). If a DSB becomes disconnected from the sister chromatid (perhaps due to movements created by transcription or loop extrusion), ectopic repair could be initiated (right). 53BP1-driven chromatin mobility is proposed to dislodge such ectopic interactions, allowing the DSB to rejoin the sister chromatid. When the DSB is engaged in repair using the sister chromatid, 53BP1-driven mobility will not dislodge the DSB because of the counterforce of cohesion and extensive base-pairing. **B,** 53BP1 is proposed to prevent ectopic repair by holding the two DNA ends of a DSB in proximity. **C,** The RIF1 axis of 53BP1 is proposed to repress illegitimate recombination through SSA by preventing the formation of long 3' overhangs. Repeats that could lead to SSA (green boxes) are only exposed when 3' overhangs become overly long in the absence of 53BP1.

original partner. DSBs that are engaged in recombination with the sister chromatid would be resistant to this force because they are held down by cohesion and because of RAD51-mediated strand-invasion. DSB mobility in G1 may also allow disconnected DNA ends to undertake a search to reconnect and avoid repair at ectopic sites. DSB mobility could be disadvantageous in cells with a high burden of DNA breaks (such as after IR in laboratory settings or upon removal of TRF2), but *in vivo*, most nuclei will contain only one or a few DSBs.

A second aspect of 53BP1 that may promote the fidelity of DSB repair is its synapsis function (Figure 1.8B). By keeping DSBs together until their successful repair, 53BP1 could diminish the risk of ectopic repair in the setting of DSBs in S/G2 and in G1. This function of 53BP1 is also suited for CSR where distal DSBs need to be held together. Therefore, the synapsis function of 53BP1 may have been enhanced when CSR evolved. As is the case for DSB mobility, synapsis can have detrimental side effects when multiple DSBs become clustered, but (as argued above) this situation is unlikely to occur *in vivo*.

The third aspect of 53BP1 that improves the fidelity of DNA repair is found in the RIF1/shieldin/CST axis. By limiting the formation of long 3' overhangs at DSBs, 53BP1 can prevent DSBs from being processed by SSA (Figure 1.1B; Figure 1.8C). SSA is a dangerous repair pathway in genomes with many repetitive sequences since deletions will be a frequent outcome. Indeed, a shift from HDR to SSA has been noted under conditions where 53BP1 function is insufficient[103,156].

Although the RIF1/shieldin/CST axis can be rationalized based on the proposal that this system has evolved to repress SSA at DSBs, a puzzle remains. As noted above, both in the settings of CSR and telomere fusions, the ability of the RIF1/shieldin/CST axis to promote cNHEJ is not readily explained simply based on limiting the length of 3' overhangs. In addition, the cNHEJ-mediated formation of radial chromosomes in PARPi-treated BRCA2-null cells that lack 53BP1 argues that in this context too, long 3' overhangs do not impede cNHEJ. Is it possible that RIF1/shieldin/CST have a feature that improves cNHEJ independent of their effects on ssDNA formation? Perhaps their presence competes with other factors that would shuttle the ends into alternative pathways? For instance, do they compete with RAD51 and/or RAD52, as suggested by Lukas[156]?

If RIF1/shieldin/CST prevent the binding of other DNA repair factors, this could explain why loss of 53BP1/RIF1/shieldin/CST promotes HDR in cells lacking BRCA1. Re-activation of HDR is not fully explained based on the creation of ssDNA since it is predicted that the DSBs have an overhang even when RIF1/shieldin/CST are engaged. It is not excluded that the re-activation of HDR results from both the creation of 3' overhangs as well as the absence of the RIF1/shieldin/CST complex at the DNA end.

The observation that there are more RPA and RAD51 foci at DSBs in BRCA1-deficient cells when RIF1/shieldin/CST are absent is compatible with the formation of longer regions of ssDNA, but it is also fully compatible with the idea that shieldin/CST compete with RAD51 and other ssDNA-binding proteins.

Taking this line of reasoning to its logical conclusion, one function of BRCA1 may be to prevent the persistence of RIF1/shieldin/CST at DSBs in newly-replicated regions where HDR occurs. This view fits with the ability of BRCA1 (in collaboration with CtIP) to minimize 53BP1 at DSBs[103,131] and with the diminished recruitment of 53BP1 at DSBs where replication has reduced the abundance of H4K20Me2[129,157]. It is even possible that the purported resection function of BRCA1, which is measured based on ssDNA proxies such as RPA and RAD51, actually reflects its efforts to remove 53BP1 from DSBs thereby allowing HDR to take over.

These speculations suggest testable hypotheses. First, it will be important to test the view that the association of KU70/80 with DSBs (and thus cNHEJ) is impeded by 3' overhangs, a contention that does not appear to fit with the current data on telomere fusions and CSR. Second, it is critical to test the hypothesis that HDR can be repressed if 53BP1 and its downstream ssDNA-binding factors persist at DSBs, an idea which is further discussed in Chapter 5 and the Appendix. Indeed, recent data suggest the potential for 53BP1 to repress HDR independent of its effect on resection[123,158]. Third, the view that 53BP1 primarily acts to improve DSB repair fidelity, for instance by preventing translocations and repressing SSA, can be tested by analyzing the genomic consequences of 53BP1 deficiency in contexts other than the three specialized settings that are discussed above.

Chapter 1 of this thesis has introduced the 53BP1 protein and its functions, particularly in the context of BRCA1-deficiency. This idea of 53BP1 as a fidelity factor grew out of our work on fill-in synthesis (Chapter 2) by RIF1, shieldin, and ultimately CST/Polα. In Chapter 3, we provide direct evidence for fill-in synthesis at DSBs, and propose that fill-in synthesis by shieldin/CST/Polα/primase is the end effect of the 53BP1 pathway in BRCA1-deficient cells. After an interlude (Chapter 4) on the regulatory role of the CRL4/DDB1/WDR70 complex in the DDR, Chapter 5 discusses and contextualizes the data.

CHAPTER 2. 53BP1-RIF1-shieldin counteracts DSB resection through CST- and Polα-dependent fill-in synthesis

2.1 Abstract

Resection of DSBs can dictate the choice between homology-directed repair (HDR), which requires a 3' overhang, and classical non-homologous end joining (cNHEJ), which can join unresected ends[2,3]. BRCA1 mutant cancers show minimal DSB resection, rendering them HDR deficient and sensitive to PARP1 inhibitors (PARPi)[25–27,87,88,104]. When BRCA1 is absent, DSB resection is thought to be prevented by 53BP1, RIF1, and the REV7/SHLD1/SHLD2/SHLD3 (shieldin) complex and loss of these factors diminishes PARPi sensitivity[27,87,88,91,104]. This chapter addresses the mechanism by which 53BP1/RIF1/shieldin regulate the generation of recombinogenic 3' overhangs. CST (CTC1, STN1, TEN1[86]), an RPA-like complex that functions as a Polymeraseα/primase accessory factor[147] is a downstream effector in the 53BP1 pathway. CST interacts with shieldin and localizes with Polα to sites of DNA damage in a 53BP1- and shieldin-dependent manner. Like loss of 53BP1/RIF1/shieldin, CST depletion leads to increased resection. Furthermore, in BRCA1-deficient cells, CST prevents RAD51 loading and promotes PARPi efficacy. Finally, Polα inhibition diminishes the effect of PARPi in BRCA1-deficient cells. These data suggest that CST/Polα-mediated fill-in contributes to the control of DSB repair by 53BP1, RIF1, and shieldin.

2.2 Introduction

This study was initiated to determine whether the control of 5' resection at DSBs resembles the regulation of resection at telomeres. The formation of the telomeric t-loop requires a 3' single-stranded (ss) overhang[71,72]. After telomere replication, the 3' overhang is generated in a multi-step process regulated by the shelterin complex[65,159]. Newly-replicated telomeres initially undergo extensive 5' resection by EXO1, leading to 3' overhangs that are overly long[83]. Subsequent fill-in synthesis by Polα/primase restores the 3' overhang to the correct length (Figure 2.1A). Polα/primase is brought to telomeres by CST (also called Polymeraseα-associated factor, or AAF[146,147]), which binds to the POT1b subunit of mouse shelterin[83] (Figure 2.1A). Because POT1b is required for CST/polα-primase fill-in, telomeres lacking POT1b show hyper-resection, similar to DSBs lacking 53BP1, RIF1, or shieldin (REV7/SHLD1/SHLD2/SHLD3[91]). Here we provide data suggesting that the role of CST/Polα is not limited to telomeres but extends to the repair of DSBs.

2.3 Shieldin and CST counteract resection at dysfunctional telomeres

To study the role of CST in controlling 5' end resection at sites of DNA damage, we first used telomeres lacking shelterin protection, which are a versatile model system for DSB resection[30,65,160,161]. Upon Cre-mediated deletion of the TPP1 component of shelterin from immortalized *Tpp1*$^{F/F}$ mouse embryo fibroblasts (MEFs), telomeres undergo hyper-resection that is counteracted by 53BP1 and RIF1[161]. 53BP1 and RIF1 accumulate at telomeres in response to ATR kinase signaling, which is activated at telomeres that lack the TPP1-interacting partner POT1a (Figure 2.1A). We first assessed whether shieldin, like 53BP1 and RIF1, limits hyper-resection at telomeres lacking TPP1. *Tpp1*$^{F/F}$ cells from which either REV7 (Figure 2.1B-D) or SHLD2 (Figure 2.1E-G) was removed with CRISPR/Cas9 showed hyper-resection after deletion of TPP1, indicating that shieldin limits hyper-resection at damaged telomeres as it does at DSBs[87,88,91].

To circumvent the lethality of CST deletion[162,163], we used partial inhibition with shRNAs to explore the role of CST in counteracting resection at dysfunctional telomeres. An shRNA to STN1[83] that did not curb cell cycle progression (Figure 2.1H) increased the telomeric overhang signal in cells lacking TPP1 (Figure 2.1B-D). Similarly, knockdown of CTC1 induced an increase in the overhang signal upon TPP1 loss (Figure 2.1I-K). The single-stranded (ss) telomeric DNA signal induced by CST depletion was removed by *E. coli* 3' nuclease ExoI, confirming that it represents a 3' overhang (Figure 2.2). As expected, STN1 shRNA also resulted in a small increase in the 3' overhang in cells not treated with Cre (Figure 2.1B-D), reflecting the deficiency in

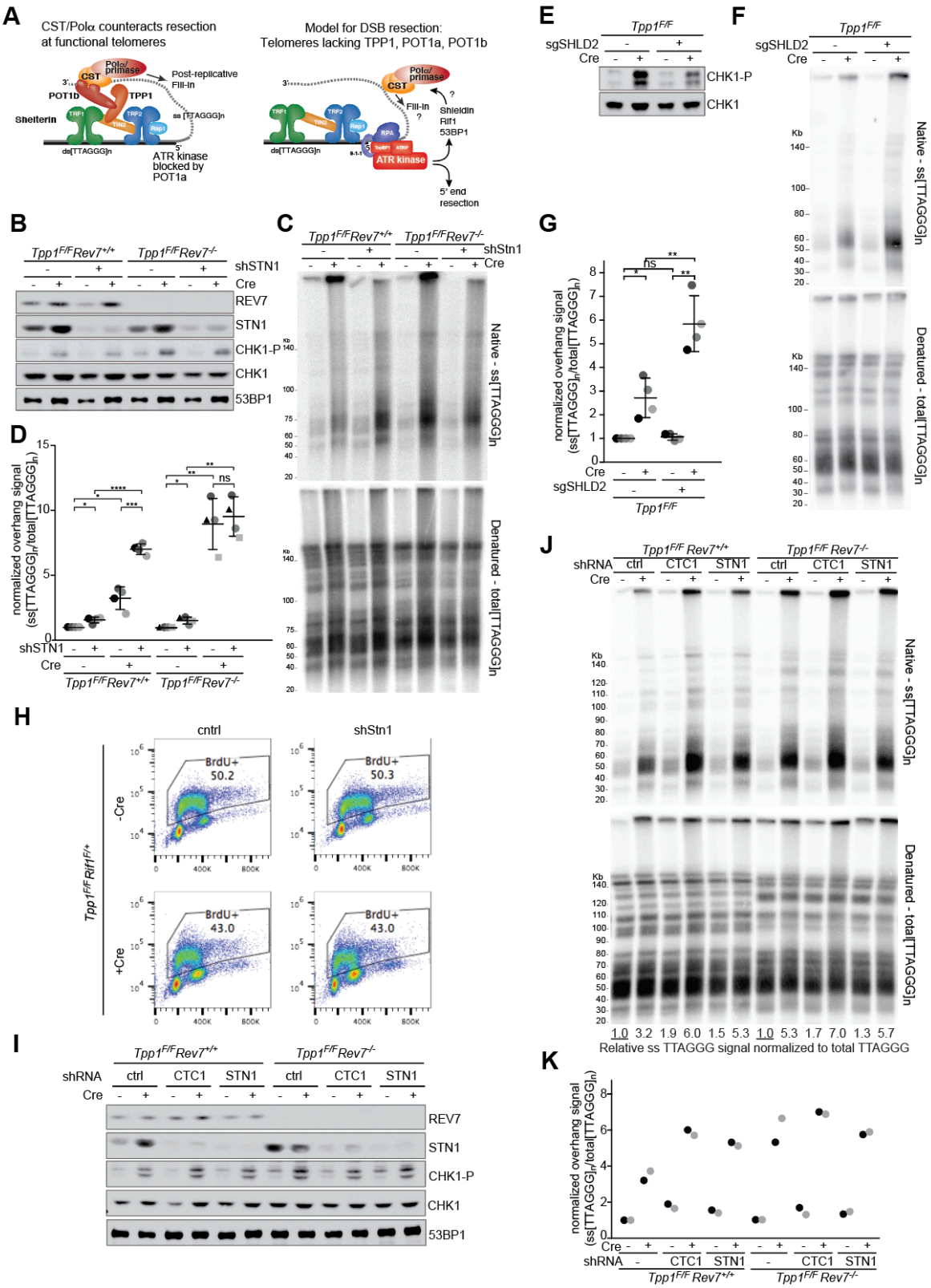
A
CST/Polα counteracts resection at functional telomeres
Model for DSB resection: Telomeres lacking TPP1, POT1a, POT1b
Shelterin
POT1b
TPP1
Post-replicative Fill-in
ATR kinase blocked by POT1a
ATR kinase
Fill-in
Shieldin
Rif1
53BP1
5' end resection
B
Tpp1F/FRev7+/+
Tpp1F/FRev7-/-
shSTN1
Cre
REV7
STN1
CHK1-P
CHK1
53BP1
C
shStn1
Native - ss[TTAGGG]n
Denatured - total[TTAGGG]n
D
normalized overhang signal (ss[TTAGGG]n/total[TTAGGG]n)
E
sgSHLD2
F
G
ns
H
cntrl
shStn1
-Cre
+Cre
BrdU+ 50.2
BrdU+ 50.3
BrdU+ 43.0
BrdU+ 43.0
I
shRNA
ctrl
CTC1
STN1
J
1.0 3.2 1.9 6.0 1.5 5.3 1.0 5.3 1.7 7.0 1.3 5.7
Relative ss TTAGGG signal normalized to total TTAGGG
K

Figure 2.1. Shieldin and CST counteract resection at telomeres lacking TPP1
A, Left: Schematic showing POT1b-bound CST counteracting resection of telomere ends. Right: Depiction of telomeres lacking TPP1, POT1a, and POT1b as a proxy for DSB resection. Telomeres lacking TPP1 undergo ATR-dependent hyper-resection that is repressed by 53BP1. **B**, Immunoblots showing loss of REV7 and STN1 in the indicated *Tpp1*$^{F/F}$ *Rev7*$^{+/+}$ and *Tpp1*$^{F/F}$ *Rev7*$^{-/-}$ (CRISPR) clones treated with Cre (96 h) as indicated and with or without STN1 shRNA. CHK1-P serves as a proxy for TPP1 deletion. **C**, Quantitative analysis of telomere end resection in the cells shown in **B** using in-gel hybridization to detect the 3' overhang (top) followed by rehybridization to the denatured DNA in the same gel, allowing the ratio of ss to total TTAGGG signal to be determined in each lane. **D**, Quantification of resection detected as in **C**, determined from four independent experiments (indicated by different shades of gray) showing means and SDs. Each experiment involved all indicated samples analyzed in parallel, indicated with the same shade of grey. Three independent REV7 CRISPR/Cas9 KO clones were used (indicated with distinct symbols). **E-G,** Effect of SHLD2 on hyper-resection at telomeres lacking TPP1. **E**, Immunoblot for pCHK1, an indicator of TPP1 deletion, in *Tpp1*$^{F/F}$ MEFs with and without bulk population treatment with an sgRNA to *Shld2* and/or Cre. **F**, Quantitative analysis of telomere end resection as in **C** using the cells shown in **E**. **G**, Quantification of the extent of resection detected in **F** as in **D**. **H**, FACS profiles of the indicated cells incubated with BrdU to measure (lack of) S phase effects of the STN1 shRNA. **I**, Immunoblots showing absence of REV7 and reduction of STN1 expression in the indicated *Tpp1*$^{F/F}$ and *Tpp1*$^{F/F}$ *Rev7*$^{-/-}$ MEFs treated with either CTC1 or STN1 shRNA. Diminished STN1 expression is used as a proxy for the efficacy of the CTC1 shRNA. **J**, Quantitative analysis of telomeric overhangs as in **C**. **K**, Quantification of the effect of CTC1 and STN1 on resection at telomeres lacking TPP1 as in **D**. Data is obtained from two independent REV7-proficient and two independent REV7-deficient clones (light and dark shading). All means are indicated with center bars and SDs with error bars. Statistical analysis based on two-tailed Welch's t-test. *, $p<0.05$; **, $p<0.01$; ***, $p<0.001$; ****, $p<0.0001$; ns, not significant. Experiments performed by Tatsuya Kibe and Francisca Lottersberger.

POT1b- and CST/Polα-dependent fill-in of newly-formed 3' overhangs[83]. Importantly, in the Cre-treated *Tpp1*$^{F/F}$ cells, the repression of resection by CST must be independent of its interaction with shelterin since POT1b is absent (Figure 2.1A), suggesting that other factors recruit CST to dysfunctional telomeres.

STN1 knockdown did not affect the extent of resection at telomeres when TPP1 was deleted from REV7-deficient cells and the same result was obtained with an shRNA to CTC1 (Figure 2.1B-D; I-K). Consistent with this finding, STN1 knockdown had no

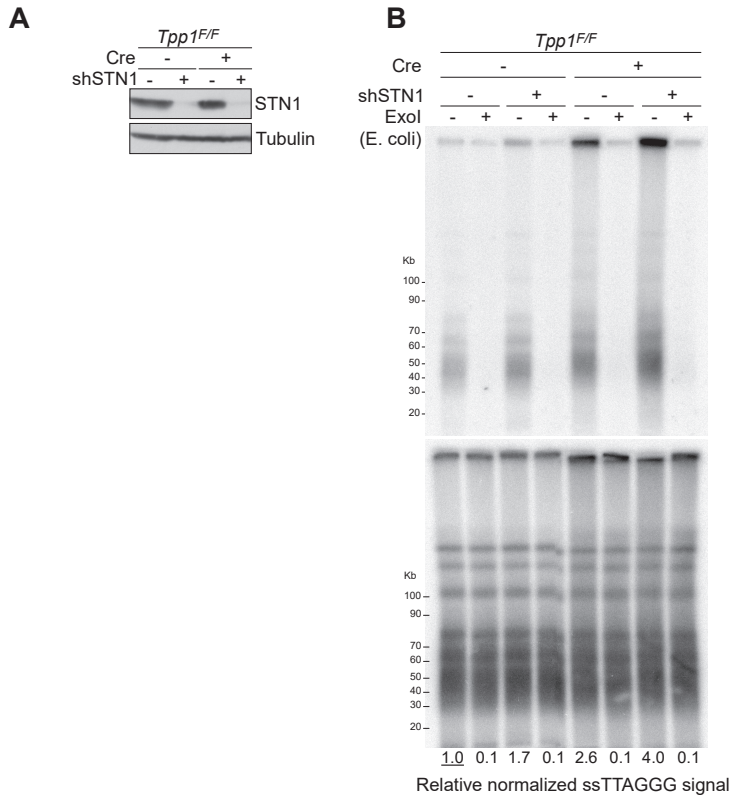

Figure 2.2. ssDNA induced by STN1 depletion represents a 3' overhang
A, Immunoblot for STN1 and g-tubulin in *Tpp1*$^{F/F}$ *(Rif1*$^{F/+}$*)* cells treated with STN1 shRNA and/or Cre. **B,** Experiment to verify that the ssDNA signal derives from a 3' overhang. Plugs in the ExoI lanes were treated with 3' exonuclease from *E. coli*. Experiment performed by Tatsuya Kibe.

effect on the resection of telomeres lacking TPP1 when either 53BP1 or RIF1 were absent or when cells contained an allele of 53BP1 that does not recruit RIF1[75] (Figure 2.3). These data suggest that CST acts in a 53BP1-, RIF1-, and shieldin-dependent manner to limit the formation of ssDNA at dysfunctional telomeres.

To determine whether CST also counteracted resection at sites of DNA damage that activate the ATM kinase, we used conditional deletion of the shelterin subunit TRF2 (Figure 2.4A). Telomeres lacking TRF2 activate the ATM kinase and undergo fusion through cNHEJ[66,79,164]. In LIG4-deficient cells, in which most telomere fusions are

prevented[66], telomeres lacking TRF2 undergo 5' end resection that is repressed by 53BP1 and RIF1[27,30] (Figure 2.4A). As expected, deficiency in either REV7 (Figure 2.4B-D) or SHLD2 (Figure 2.4E-G) led to greater resection at telomeres lacking TRF2, indicating that shieldin also controls resection at sites of ATM signaling. Consistent with the results at telomeres lacking TPP1, when STN1 was depleted from cells lacking TRF2, resection at telomeres was significantly increased (Figure 2.4B-D). And as was

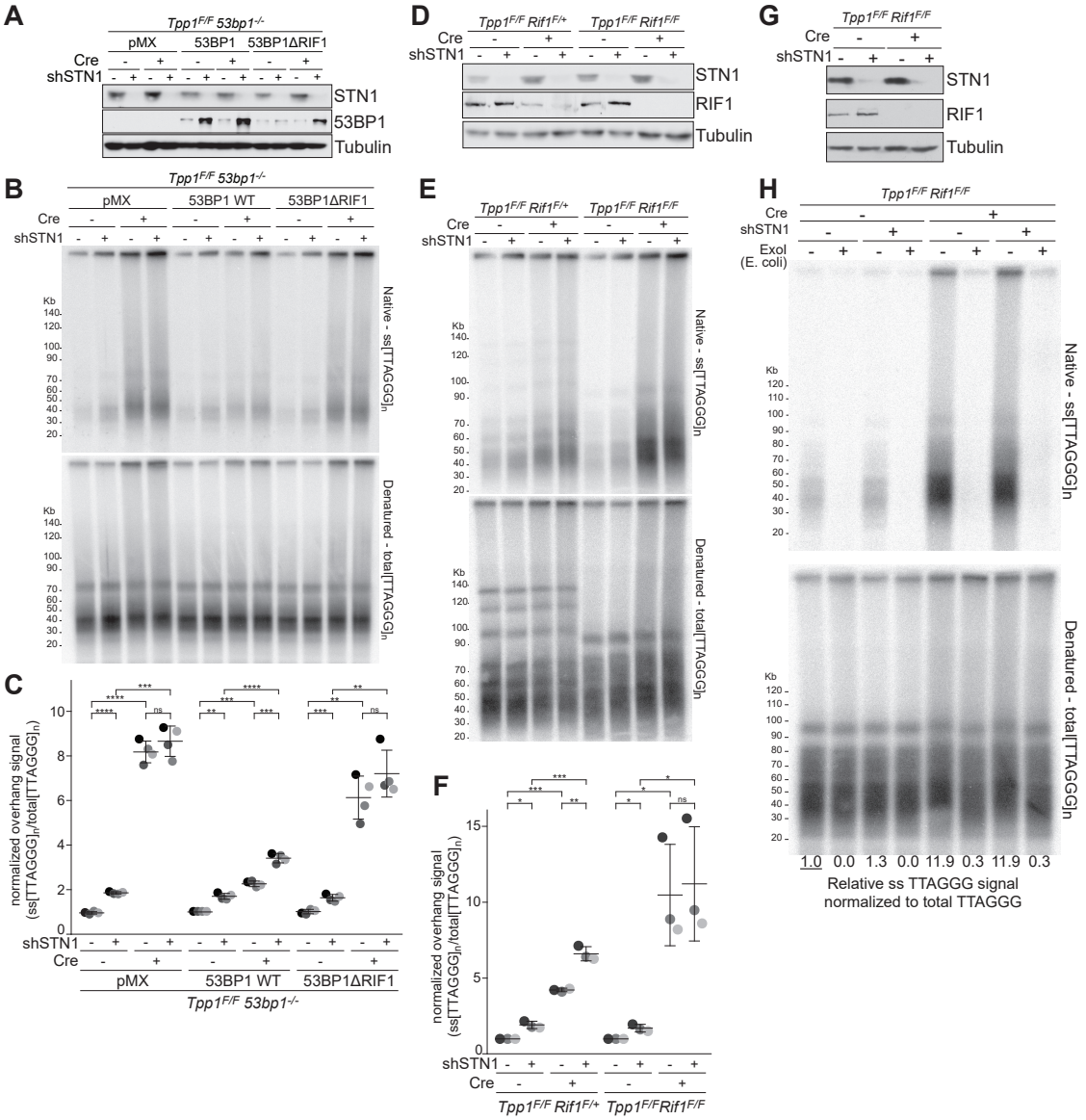

Figure 2.3. CST and RIF1 act together at dysfunctional telomeres. A, *Tpp1*$^{F/F}$ *53bp1*$^{-/-}$ cells were complemented with wt 53BP1 or a mutant 53BP1 lacking the ability to interact with RIF1, treated with a STN1 shRNA as indicated, and analyzed by immunoblotting for 53BP1 and STN1. **B**, Quantitative analysis of telomeric overhangs as in Figure 2.1**C**. **C**, Quantification of the resection at telomeres lacking TPP1 in four independent experiments performed as in Figure 2.1**D**. **D**, Immunoblots showing loss of RIF1 and STN1 in the indicated *Tpp1*$^{F/F}$ *Rif1*$^{F/+}$ and *Tpp1*$^{F/F}$ *Rif1*$^{F/F}$ MEFs treated with Cre (96 h) as indicated and with or without STN1 shRNA. Note diminished RIF1 levels after Cre due to heterozygosity in the *Tpp1*$^{F/F}$ *Rif1*$^{F/+}$ cells. **E**, Quantitative analysis of telomeric overhangs as in Figure 2.1**C**. **F**, Quantification of the extent of resection detected as in **C**, determined from three independent experiments (indicated by different shades of gray) showing means (center bars) and SDs (error bars). Each experiment involved all indicated samples analyzed in parallel. **G, H,** Experiments to verify that the ssDNA signal derives from a 3' overhang. **G**, Immunoblot for STN1 and γtubulin in *Tpp1*$^{F/F}$ *Rif1*$^{F/F}$ cells treated with STN1 shRNA and/or Cre. Representative of two experiments. **H**, Quantitative assay for telomeric overhangs as in Figure 2.1**C**. Plugs in the ExoI lanes were treated with the 3' exonuclease from E. coli. All statistical analyses as in Figure 2.1. Experiments performed by Tatsuya Kibe and Francisca Lottersberger.

the case for resection at telomeres lacking TPP1, resection at telomeres lacking TRF2 was not affected by STN1 knockdown when the shieldin component REV7 was absent (Figure 2.4B-D). Thus, CST also counteracts resection in a shieldin-dependent manner at dysfunctional telomeres that activate the ATM kinase.

2.4 53BP1- and shieldin-dependent localization of CST to dysfunctional telomeres

To further validate these results, we determined whether CST localized to damaged telomeres in a 53BP1- and shieldin-dependent manner. As expected, myc-tagged CTC1 was detectable at telomeres in mouse cells with functional shelterin (Figure 2.5A, B). In POT1b-deficient cells, which show extended telomeric 3' overhangs but no DNA damage signaling[165], the localization of CTC1 to telomeres was minimal (Figure 2.5A, B), consistent with POT1b-dependent CST recruitment[83]. When ATR signaling was activated at telomeres by deletion of TPP1 (Figure 2.5A; right panel), CTC1 was again

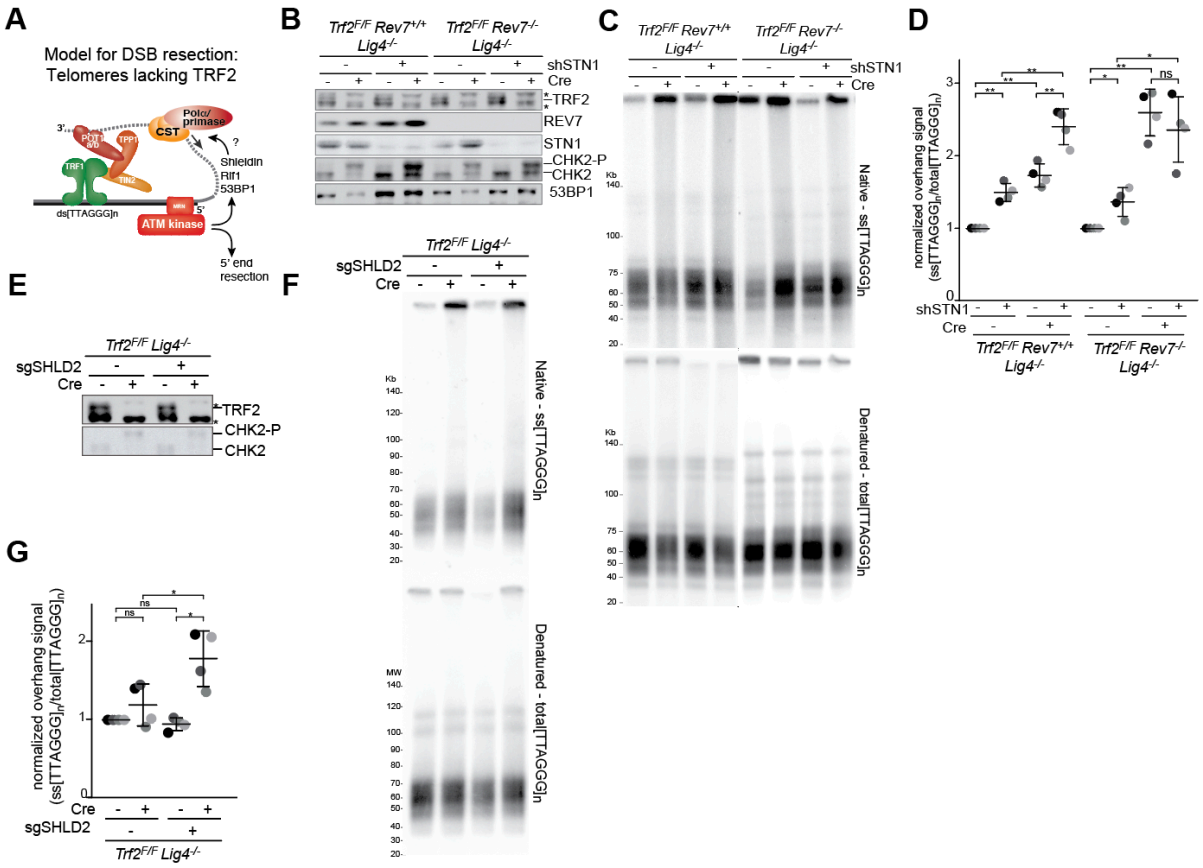

Figure 2.4. Shieldin and CST counteract resection at telomeres lacking TRF2. **A**, Depiction of telomeres lacking TRF2 as a model for resection at ATM-activating DSBs. **B**, Immunoblots showing Cre-mediated deletion of TRF2 from *Trf2*$^{F/F}$ *Lig4*$^{-/-}$ cells, CRISPR deletion of *REV7*, shRNA-mediated reduction of STN1, and CHK2 phosphorylation. Asterisk: non-specific. **C and D**, Telomere end resection analysis on the cells in **B** as in Figure 2.1**C, D**. Means and SDs from four independent experiments using two clones of each genotype. Note that the order of the samples is different in **D** versus **B** and **C**. **E**, Immunoblots for TRF2 deletion and CHK2 phosphorylation in *Trf2*$^{F/F}$ *Lig4*$^{-/-}$ MEFs with and without bulk population treatment with an sgRNA to *Shld2* and/or Cre. Asterisk: non-specific band. **F**, Quantitative analysis of telomere end resection as in Figure 2.1**C** using the cells shown in **E**. **G**, Quantification of the extent of resection detected in **F** as in Figure 2.1**D**. Means (center bars) and SDs (error bars) from three independent experiments. All statistical analysis as in Figure 2.1. Experiments performed Francisca Lottersberger.

detectable at a subset of dysfunctional telomeres (Figure 2.5A, B), despite the absence of POT1b from these telomeres. Recruitment of CTC1 to the dysfunctional telomeres

depended on ATR kinase activity and 53BP1 (Figure 2.5B). Importantly, recruitment of CST was abrogated in cells lacking the REV7 or SHLD2 components of shieldin (Figure 2.5B, C), indicating that shieldin is required for CST recruitment at dysfunctional telomeres. Similarly, Cre-mediated deletion of the single human POT1 protein using POT1 conditional KO HT1080 cells[84] led to accumulation of STN1 at telomeres (Figure

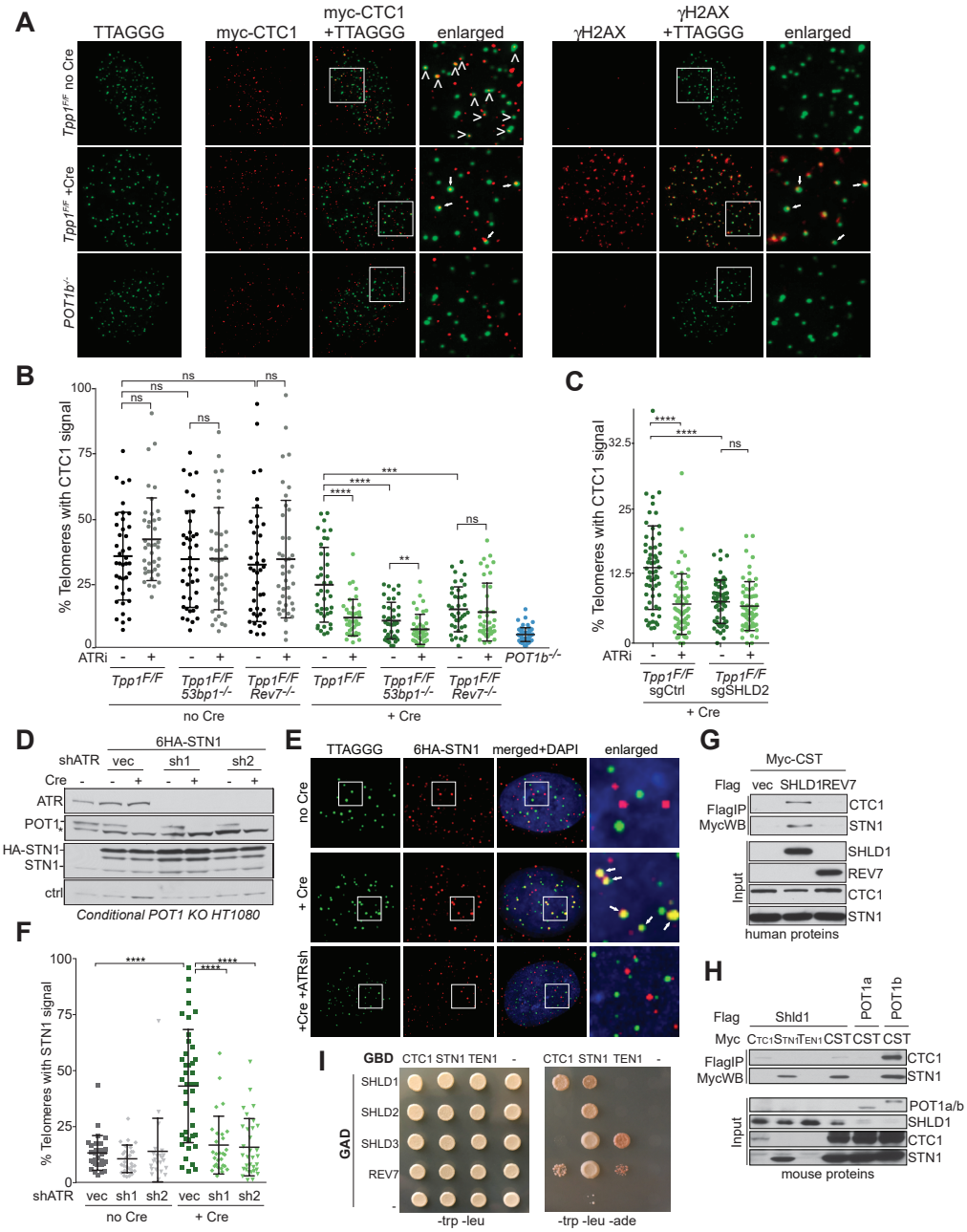

Figure 2.5. 53BP1- and shieldin-dependent localization of CST to dysfunctional telomeres. A, Left: Representative IF-FISH for 6xmyc-tagged CTC1 (red) at telomeres (false-colored in green) in *Tpp1*$^{F/F}$ MEFs with or without Cre treatment (96 h). Arrowheads highlight CTC1 at telomeres. *POT1b*$^{-/-}$ cells serve as a control for spurious telomere-CTC1 co-localization. Right: The same nuclei showing γH2AX (red) at telomeres lacking TPP1. For clarity, the γH2AX signals and the CTC1 signals are both false-colored in red. Arrows highlight telomeres containing both CTC1 and γH2AX. **B**, Quantification of the % of telomeres co-localizing with CTC1 detected as in **A**. Each dot represents one nucleus from the indicated *Tpp1*$^{F/F}$ cell lines with and without Cre and/or ATR inhibition. Means and SDs from three independent experiments. **C**, As in **B** but using *Tpp1*$^{F/F}$ cells treated with an sgRNA for *Shld2* or a control sgRNA. **D**, Immunoblots for POT1 deletion, ATR knockdown, and expression of HA-STN1 in conditional *POT1 KO* HT1080 cells. Asterisk: non-specific band. **E**, IF-FISH showing telomeric DNA co-localizing with HA-tagged human STN1 in human conditional *POT1 KO* HT1080 cells treated with Cre (96 h) and treated with two independent ATR shRNAs. **F**, Quantification of STN1 localization at telomeres before and after POT1 deletion with or without ATR shRNAs as in **E**. Means and SDs from three independent experiments. Each symbol represents one nucleus. **G**, Immunoprecipitation of human CST (each subunit bearing a Myc-tag) with Flag-tagged human SHLD1 or REV7 co-expressed in 293T cells. TEN1 is not shown. Experiments in **D-G** performed by Hiro Takai **H**, Immunoprecipitation of individual mouse CST subunits or the three-subunit complex (each subunit bearing a myc-tag) with Flag-tagged mouse SHLD1 co-expressed in 293T Flag-tagged POT1b and POT1a serve as positive and negative controls for CST binding, respectively. Experiment performed by Kaori Takai. **I**, Yeast two-hybrid assay for interaction between CST and shieldin subunits fused to the Gal4 DNA binding domain (GDB) and the Activation domain (GAD), respectively. Experiment performed by Alessandro Bianchi. All means are indicated with center bars and SDs with error bars. Statistical analysis as in Figure 2.1.

2.5D-F) and this accumulation was dependent on the ATR signaling unleashed by the absence of POT1[84] (Figure 2.5D-F). Thus, the CTC1 and STN1 components of CST localize to damaged telomeres in a manner that is dependent on ATR signaling, 53BP1, and shieldin.

Consistent with the shieldin-dependent localization of CST, co-IP experiments in human and mouse cells showed that the SHLD1 component of shieldin could interact with CTC1 and STN1, whereas REV7 did not show a robust interaction (Figure 2.5G, H). We further analyzed the interactions between CST and shieldin using a yeast two-

hybrid assay (Figure 2.5I). According to this analysis, CTC1 robustly interacted with SHLD1, and STN1 did so with SHLD3 (Figure 2.5I). Weaker interactions were also detectable between TEN1 and SHLD3; STN1 and SHLD1, SHLD2, and REV7; and CTC1 and REV7 (Figure 2.6). These data show that the shieldin complex binds CST through multiple direct interactions between the subunits. Therefore, recruitment of CST to dysfunctional telomeres can be explained by the binding of CST to shieldin, raising the possibility that CST might act at genome-wide at DSBs through shieldin-dependent recruitment.

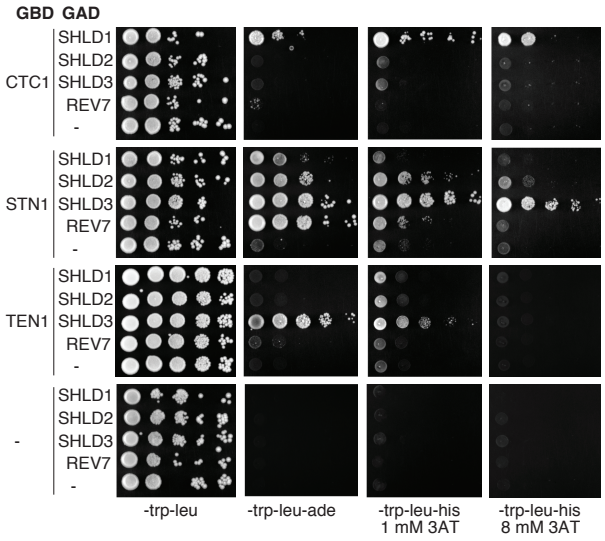

Figure 2.6. CST makes multiple direct interactions with shieldin. Two-hybrid analysis of CST-shieldin interaction. Yeast cultures were grown overnight in synthetic complete medium lacking tryptophan and leucine to a density of $5*10^7$ cells/ml. Serial 10-fold dilutions were generated and 4 ul of each dilution was spotted on synthetic complete media lacking the nutrients tryptophan, leucine, adenine, histidine, and containing 3-aminotriazole (3-AT) as indicated. Plates were then incubated for 5 days at 30ºC before imaging. Experiment performed by Alessandro Bianchi.

2.5 CST localizes to DSBs and represses formation of single-stranded DNA

In agreement with the idea that CST has a role at non-telomeric sites of DNA damage, ionizing radiation (IR)-induced DSBs in human cells showed STN1 co-localizing with 53BP1 (Figure 2.7A, B) and this localization of STN1 to DSBs was dependent on the REV7 and SHLD2 components of shieldin (Figure 2.7B). Furthermore, STN1 was detectable at FOKI-induced DSBs in U2OS cells and this

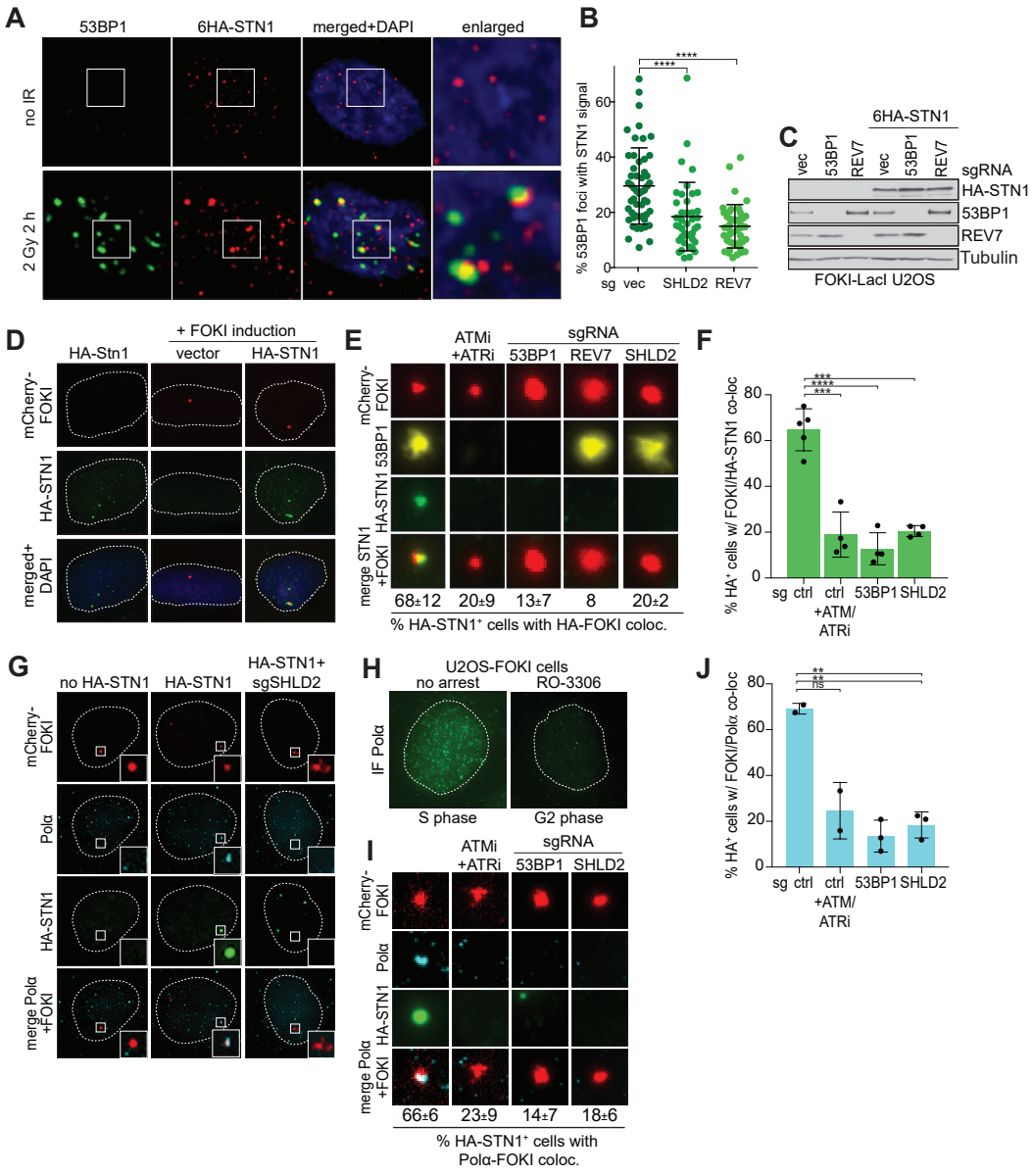

Figure 2.7. CST and Polα localize to DSBs. A, IF for 53BP1 and HA-STN1 in irradiated HT1080 cells. **B**, Quantification of 53BP1/STN1 co-localization as in **A** in cells with the indicated sgRNAs. Means and SDs from three independent experiments with >15 nuclei (symbols) analyzed for each experimental setting. Experiment performed by Hiro Takai. **C**, Immunoblots for the indicated proteins in FOKI-LacI U2OS cells treated with the indicated sgRNAs. **D**, IF for mCherry-FOKI (red), and HA-STN1 (green) in FOKI-LacI U2OS cells as in **C**. **E**, Examples of HA-STN1 co-localizing with FOKI foci in cells as in **D** treated with ATM and ATR inhibitors, or the indicated sgRNAs and quantification of STN1/FOKI co-localization. Means and SDs three independent experiments with >80 induced nuclei analyzed for each condition. **F**, Quantification of HA-STN1 localization to FOKI-induced DSBs as in **E**. **G**, Examples of HA-STN1 and Polα localization at FOKI-induced DSBs in G2 arrested FOKI-LacI U2OS cells. **H**, IF for endogenous Polα in FOKI-LacI U2OS cells in S phase and after RO-3306 treatment (G2). Dotted line: outline of the nucleus. **I,** Quantification of colocalization as in **E** but monitoring Polα at DSBs in G2-arrested cells expressing HA-STN1. **J**, Quantification of co-localization of Polα with FOKI-induced DSBs as in **K**. Means (center bars) and SDs (error bars) from three independent experiments unless otherwise indicated. All statistical analysis as in Figure 2.1.

localization was diminished by addition of ATM and ATR inhibitors, and by loss of 53BP1, REV7, or SHLD2 (Figure 2.7C-F), indicating that CST behaves as a DNA damage response factor at DSBs.

Given that the only known function of CST is to promote Polα/primase-mediated fill-in, we examined the localization of Polα to DSBs. To detect Polα at DSBs in a manner that is not confounded by the many S phase foci formed by Polα, we arrested cells in G2 using the RO-3306 CDK1 inhibitor, resulting in nuclei with a modest number of spontaneous Polα foci (Figure 2.7G,H). In G2 cells expressing HA-STN1, Polα co-localized with STN1 at FOKI-induced DSBs (Figure 2.7G, I). Localization of Polα to DSBs required ATM/ATR signaling, 53BP1, and SHLD2 (Figure 2.7G-J), indicating that Polα requires the same factors as CST for its localization to DSBs.

To determine the effect of CST on the processing of genome-wide DSBs, we monitored the formation of foci of the ssDNA binding protein RPA at IR-induced DSBs.

Consistent with a role for CST in counteracting resection, two STN1 shRNAs induced a significant increase in the percent of cells containing RPA foci after IR (Figure 2.8A-C). The RPA foci in cells with diminished CST had greater signal intensity (Figure 2.8B) and the overall RPA signal intensity per nucleus was elevated (Figure 2.8D). Furthermore,

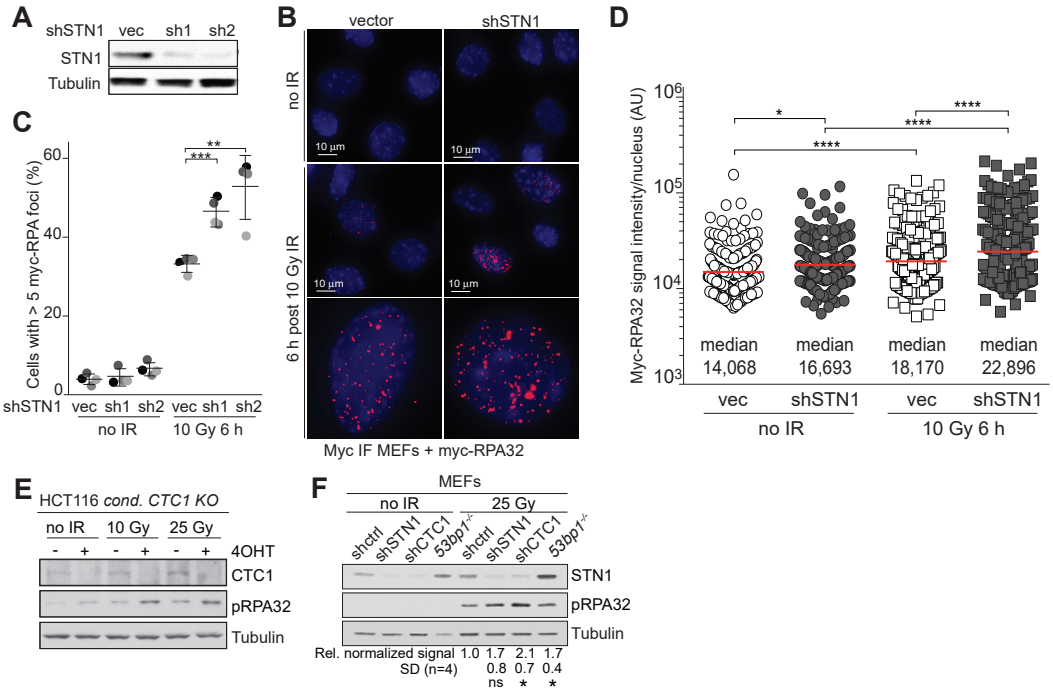

Figure 2.8. Effect of CST loss on IR-induced RPA. A, Immunoblot for STN1 knockdown in Myc-RPA32-expressing MEFs. **B**, IF for myc-RPA32 6 h after 10 Gy IR. **C**, Quantification of cells with RPA foci as in **B** in >30 nuclei for each condition in three independent experiments (grey shading) with means and SDs. **D,** Quantification of myc-RPA32 intensity per nucleus in cells as in **B**. Medians (center bars and numbers below) obtained from four independent experiments with >20 nuclei for each experimental condition in each experiment. Each symbol represents one nucleus. Statistical analysis as in Figure 2.1. Experiments in **A-D** performed by Yi Gong. **E**, Immunoblots for IR-induced RPA phosphorylation (pS4/S8) after CTC1 deletion. Experiment performed by Hiro Takai. **F,** Immunoblots for IR-induced RPA phosphorylation (pS4/S8) after depletion of STN1, CTC1, or 53BP1.

conditional deletion of CTC1 from a human CTC1 KO HCT116 cell line[163] led to an increase in the phosphorylation of RPA upon irradiation (Figure 2.8E), consistent with

CST modulating the formation of ssDNA at DSBs. Increased phosphorylation of RPA was also observed in irradiated MEFs when CST was depleted with an shRNA to STN1 or CTC1 and the effect of CST depletion was similar to the effect of 53BP1 loss in these cells (Figure 2.8F). Consistent with a role in counteracting resection, depletion of CST resulted in an increase of IR-induced RAD51 foci in cells lacking BRCA1 (Figure 2.9A, B), suggesting that CST depletion can restore HDR. Conversely, depletion of CST diminished cNHEJ based on an assay for the fusion of telomeres that lack TRF2[66] (Figure 2.9C, D).

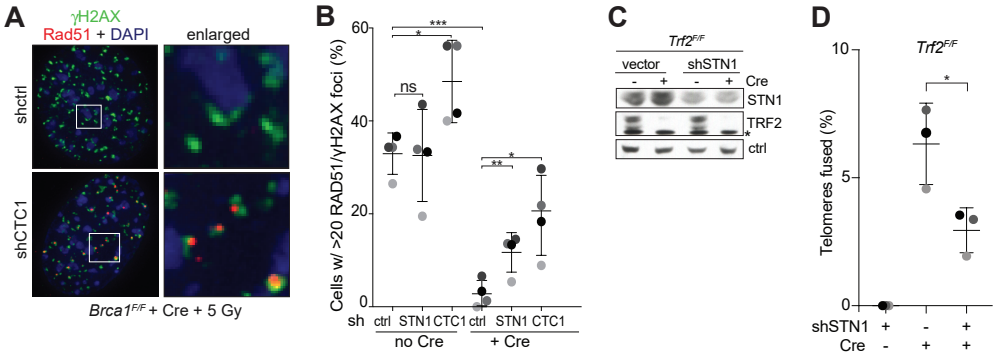

Figure 2.9. Effect of CST on RAD51 loading and fusion of telomeres lacking TRF2. A, IF for RAD51/γH2AX co-localization at IR-induced DSBs in BRCA1-deficient cells treated with CTC1 shRNA. **B**, Quantification of data as in **A**. Means and SDs from >15 nuclei analyzed for each experimental setting in four independent experiments (grey shading). **C**, Immunoblot for STN1 knockdown and TRF2 deletion from induced *Trf2*$^{F/F}$ RosaCre MEFs (72 h). Asterisk: non-specific. **D**, Effect of STN1 shRNA knockdown on telomere-telomere fusions. Means and SDs from three independent experiments (>6000 telomeres for each condition). Experiment in **C, D** performed by Kaori Takai and Titia de Lange. All IF and immunoblots shown are representative of three experiments. All means are indicated with center bars and SDs with error bars. Statistical analysis as in Figure 2.1.

2.6 CST and Polα affect the outcome of PARPi in BRCA1-deficient cells

BRCA1-deficient cells become resistant to PARPi treatment when 53BP1, RIF1, or shieldin components are absent[25–27,87,88,91,103,104]. To determine whether CST has the same effect, STN1 or CTC1 were depleted from *Brca1*$^{F/F}$ MEFs and PARPi sensitivity was evaluated based on colony formation after Cre treatment. CTC1 or STN1 depletion reduced the lethality of PARPi in BRCA1-deficient cells (Figure 2.10A-D). In contrast, in *Brca1*$^{F/F}$ subclones lacking either 53BP1 or REV7 generated by CRISPR/Cas9 gene disruption, depletion of CTC1 or STN1 did not affect PARPi resistance (Figure 2.10E-I). Consistent with these results, the occurrence of PARPi-induced radial chromosomes in BRCA1-deficient cells was diminished by CTC1 or STN1 depletion (Figure 2.10J, K). Importantly, CST depletion had no effect on radial chromosome formation in 53BP1- or REV7-deficient cells (Figure 2.10K). These data are consistent with CST acting with 53BP1 and shieldin to minimize formation of ssDNA at DSBs.

As Polα was detectable at DSBs in G2, we examined the role of Polα in DSB processing in PARPi-treated BRCA1-deficient cells. To avoid the confounding effects of Polα inhibition in S phase, PARPi-treated BRCA1-deficient cells were first arrested in G2 (Figure 2.10L). The resulting population of G2 cells was then treated with Polα inhibitors (Aphidicolin or CD437[166]), on the assumption that the repair of PARPi-induced DSBs largely takes place in late S/G2 (also, see Figure 3.7). Upon release into mitosis, cells that had experienced Polα inhibition in G2 showed a significant reduction in the formation of radial chromosomes (Figure 2.10L). At the highest dose of CD437, the effect of Polα inhibition was not exacerbated by shRNAs to CTC1 or STN1, consistent

Figure 2.10. CST and Polα affect the outcome of PARPi in BRCA1-deficient cells. A, Colonies detected in a PARPi survival assay using *Brca1*$^{F/F}$ MEFs with or without Cre treatment and infection with the indicated CST subunit shRNAs. **B**, Graphical representation of data as in **A** from three independent experiments. **C**, **D**, Immunoblots on the MEFs used **A, B** to verify the absence of deleted proteins and efficacy of the shRNAs. Reduction in STN1 expression is used as a proxy for the efficacy of the CTC1 shRNA since no antibody to mouse CTC1 is available. **E**, Epistasis analysis of PARPi resistance induced by absence of 53BP1 or REV7 and depletion of CST subunits. Means (symbol) and SEMs (error bars) from three independent experiments. **F-I**, Immunoblots on the MEFs used **E** to verify the absence of deleted proteins and efficacy of the shRNAs. Reduction in STN1 expression is used as a proxy for the efficacy of the CTC1 shRNA since no antibody to mouse CTC1 is available. **J**, Metaphases (DAPI) showing radial chromosomes induced by PARPi treatment of BRCA1-deficient cells. **K**, Means (center bar) and SDs (error bars) of % of misrejoined (radial) chromosomes in >10 metaphases per experimental setting for each of three independent experiments. Each dot represents one metaphase. **L**, Effect of Polα inhibition on radial formation in PARPi-treated *Brca1*$^{-/-}$ cells. Radial assays were performed on BRCA1-deficient cells (expressing the indicated shRNAs) treated according to the experimental timeline shown. Means (center bar) and SDs (error bars) of % of misrejoined (radial) chromosomes in >10 metaphases per experimental setting for each of three independent experiments. Each dot represents one metaphase. **M, N,** Control experiment to assess that cells analyzed in **L** progressed through S phase during PARPi treatment. **M**, Example of the assay for the presence of BrdU (IF) in metaphases harvested after the experimental timeline as in **L** but with BrdU added during PARPi treatment. **N**, Quantification of the BrdU incorporation into metaphase chromosomes as in **M** (n=10) in one experiment.

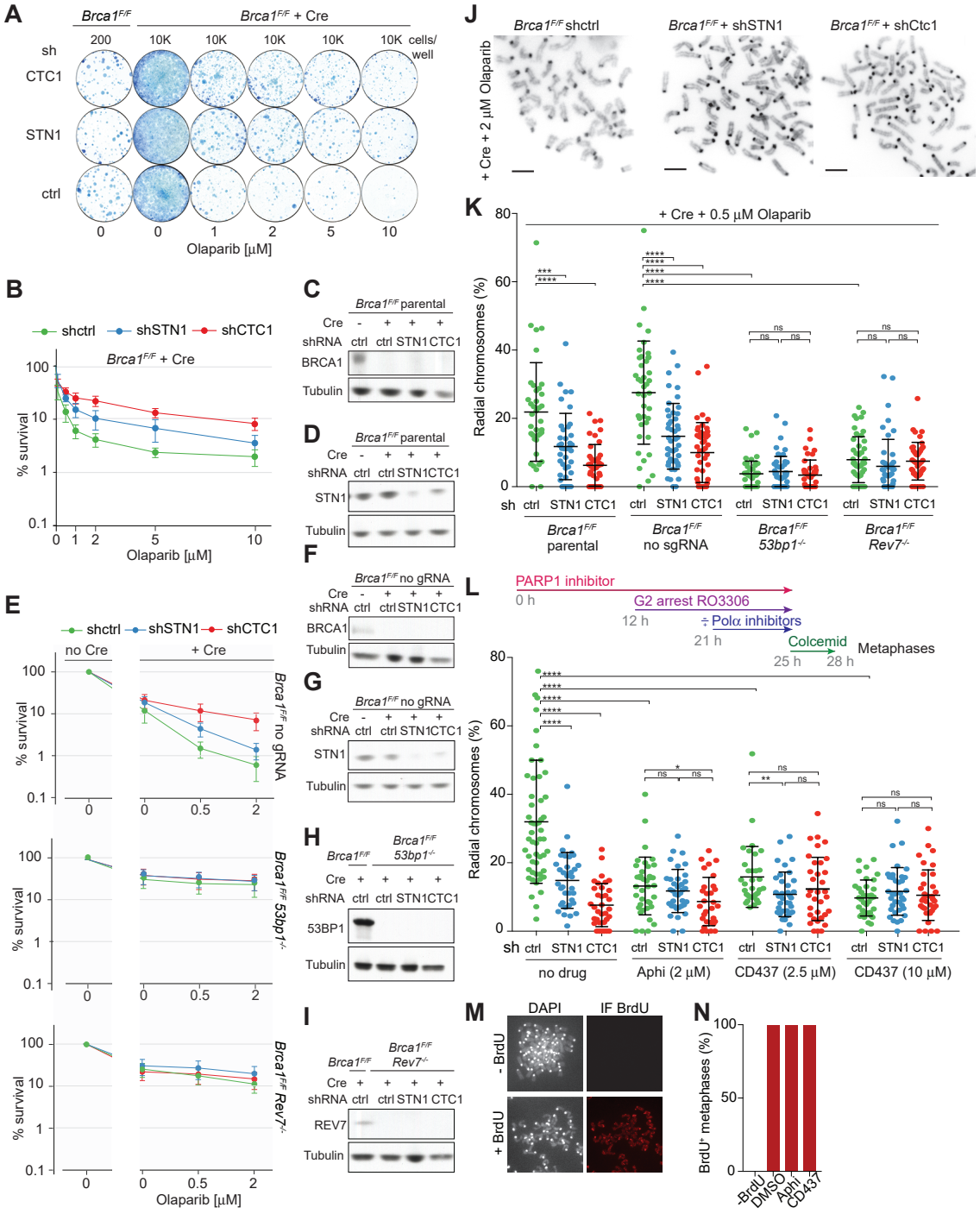
A
Brca1F/F
Brca1F/F + Cre
sh
200
10K
10K
10K
10K
10K cells/well
CTC1
STN1
ctrl
0
0
1
2
5
10
Olaparib [μM]
B
shctrl
shSTN1
shCTC1
Brca1F/F + Cre
% survival
100
10
1
0.1
0 1 2 5 10
Olaparib [μM]
C
Brca1F/F parental
Cre - + + +
shRNA ctrl ctrl STN1 CTC1
BRCA1
Tubulin
D
Brca1F/F parental
Cre - + + +
shRNA ctrl ctrl STN1 CTC1
STN1
Tubulin
E
shctrl
shSTN1
shCTC1
no Cre
+ Cre
Brca1F/F no gRNA
Brca1F/F 53bp1-/-
Brca1F/F Rev7-/-
% survival
100
10
1
0.1
0
0
0.5
2
Olaparib [μM]
F
Brca1F/F no gRNA
Cre - + + +
shRNA ctrl ctrl STN1 CTC1
BRCA1
Tubulin
G
Brca1F/F no gRNA
Cre - + + +
shRNA ctrl ctrl STN1 CTC1
STN1
Tubulin
H
Brca1F/F
Brca1F/F 53bp1-/-
Cre + + + +
shRNA ctrl ctrl STN1 CTC1
53BP1
Tubulin
I
Brca1F/F
Brca1F/F Rev7-/-
Cre + + + +
shRNA ctrl ctrl STN1 CTC1
REV7
Tubulin
J
Brca1F/F shctrl
Brca1F/F + shSTN1
Brca1F/F + shCtc1
+ Cre + 2 μM Olaparib
K
+ Cre + 0.5 μM Olaparib
Radial chromosomes (%)
80
60
40
20
0
sh ctrl STN1 CTC1 ctrl STN1 CTC1 ctrl STN1 CTC1 ctrl STN1 CTC1
Brca1F/F parental
Brca1F/F no sgRNA
Brca1F/F 53bp1-/-
Brca1F/F Rev7-/-
L
PARP1 inhibitor
0 h
G2 arrest RO3306
12 h
÷ Polα inhibitors
21 h
Colcemid
25 h
28 h
Metaphases
Radial chromosomes (%)
80
60
40
20
0
sh ctrl STN1 CTC1 ctrl STN1 CTC1 ctrl STN1 CTC1 ctrl STN1 CTC1
no drug
Aphi (2 μM)
CD437 (2.5 μM)
CD437 (10 μM)
M
DAPI
IF BrdU
- BrdU
+ BrdU
N
BrdU+ metaphases (%)
100
50
0
-BrdU
DMSO
Aphi
CD437

with Polα being dependent on CST (Figure 2.10L). Incorporation of BrdU during the PARPi treatment showed that the harvested metaphase chromosomes had progressed through S phase during Polα inhibition (Figure 2.10M, N). Collectively, these data indicate that CST acts with Polα to limit formation of recombinogenic 3' overhangs at DSBs in BRCA1-deficient cells (Figure 2.11).

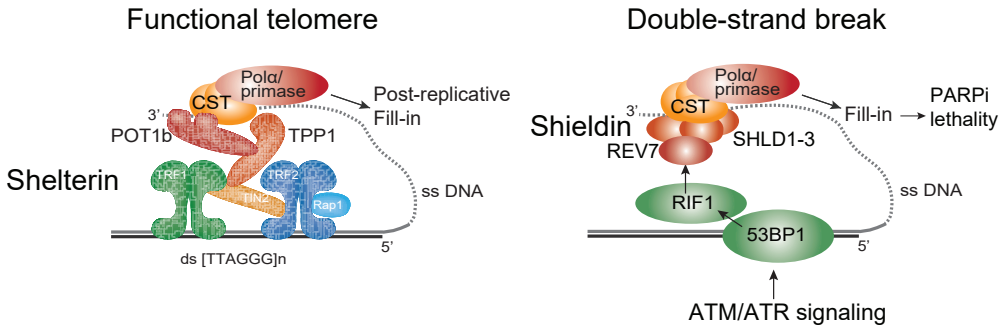

Figure 2.11. Model for analogous role of fill-in synthesis at telomeres and DSBs Graphical representation of the similar mechanisms by which resection is counteracted at functional telomeres (left) and at DSBs (right). For further discussion, see Chapter 1.

2.7 Discussion

These findings suggest that the role of CST at telomeres reflects a more general function of CST at sites of DNA damage (Figure 2.11). At telomeres, the POT1/TPP1 heterodimer recruits CST/Polα/primase to fill in the 3' overhang formed after extensive resection of newly-replicated telomeres. We propose that at sites of DNA damage, the shieldin complex recruits CST/Polα for the similar purpose of filling in resected DSBs. In both settings, CST is tethered to proteins that are locally bound, allowing CST to engage ssDNA despite its modest affinity[145] and enabling regulation of the fill-in reaction

through the recruitment of CST/Polα. Recent data showed that 53BP1 represses mutagenic Single Strand Annealing (SSA) possibly by preventing excessive resection[156]. The involvement of CST/Polα could explain this finding. At telomeres, partial fill-in by CST/Polα counteracts hyper-resection but leaves a 3' overhang for the formation of t-loops, a process similar to the initiation of HDR[71,72]. At DSBs, CST/Polα could similarly counteract hyper-resection, and thus SSA, while generating a 3' overhang sufficient for the initiation of HDR. We speculate that in BRCA1-deficient cells, this fill-in reaction and/or the persistence of CST/shieldin at the ends, blocks HDR and results in mis-repair of DSBs. For a full discussion of this idea, see Chapters 1[136] and 5, and the appendix. Although it was generally anticipated that 53BP1 functioned to prevent resection, our data suggest a sophisticated mechanism by which 53BP1 acts with shieldin, CST, and Polα to fill-in resected regions at DSBs.

CHAPTER 3. 53BP1/shieldin DSB processing in BRCA1-deficient cells requires CST/Polα/primase fill-in synthesis

3.1 Abstract

PARPi efficacy in BRCA1-deficient cells depends on 53BP1 and shieldin, which have been proposed to limit single-stranded DNA at DSBs by blocking resection and/or through CST/Polα/primase-mediated fill-in. Here we show that—like 53BP1/shieldin and CST/Polα—primase promotes radial chromosome formation in PARPi-treated BRCA1-deficient cells and demonstrate shieldin/CST/Polα/primase-dependent incorporation of BrdU at DSBs. In the absence of 53BP1/shieldin, radial formation in BRCA1-deficient cells was restored by tethering of CST near DSBs, arguing that 53BP1/shieldin acts primarily by recruiting CST. Furthermore, a SHLD1 mutant defective in CST binding (SHLD1Δ) was non-functional in BRCA1-deficient cells and its function was restored upon reconnecting SHLD1Δ to CST. Interestingly, at dysfunctional telomeres and DNA breaks in class switch recombination where CST has been implicated, SHLD1Δ was fully functional, perhaps because these DNA ends carry CST recognition sites that afford SHLD1-independent binding of CST. The data establish that in BRCA1-deficient cells, CST/Polα/primase is the major effector of shieldin-dependent DSB processing.

3.2 Introduction

53BP1 and BRCA1 are multifaceted DNA damage response proteins that participate in the repair of double-strand breaks (DSBs), in part by affecting the length of 3' single-stranded (ss) DNA overhangs[136]. In classical non-homologous end-joining (cNHEJ), minimally-processed ends are ligated by Ligase 4, a rapid and largely accurate process which is active throughout the cell cycle[6]. Homology-directed repair (HDR), in contrast, requires a 3' ss overhang and its coating by RAD51 for strand invasion of a homologous template[4,12]. BRCA1-deficient cells show minimal RAD51 loading at DSBs and are sensitive to poly(ADP)-ribose polymerase 1 inhibition (PARPi)[13,107,167]. In the absence of BRCA1-mediated HDR, some PARPi-induced DSBs are mis-rejoined into characteristic "radial" chromosomes through the action of 53BP1[25,26].

53BP1 has been proposed to control DSB repair pathway choice and/or the fidelity of DSB repair[134,136]. The role of 53BP1 in limiting the formation of 3' overhangs depends on RIF1 and the shieldin complex (REV7, SHLD1, SHLD2, and SHLD3)[27,28,35,87–89,91,92,103–105,119]. As with loss of 53BP1 or RIF1, disruption of shieldin components reverses the hallmarks of PARPi in BRCA1-deficient cells. Purified SHLD2/SHLD1 complexes can bind ssDNA oligos of 60-100 nt[91,92,120,135], an activity which has been proposed to underlie the ability of the 53BP1 pathway to limit the formation of ssDNA overhangs by blocking nucleases that attack the 5' end[91,134]. Nevertheless, direct evidence that shieldin blocks 5' end resection is lacking (but see Chapter 5 for further discussion).

In a second model, shieldin limits ssDNA at DSBs by recruiting CST/Polα/primase to counteract resection via fill-in synthesis. Supporting this model,

shieldin directly interacts with CST (CTC1, STN1, and TEN1), a Polα-associated complex. Furthermore, depletion of CST or pharmacological inhibition of Polα reduced the formation of radial chromosomes in BRCA1-deficient cells treated with PARPi (Chapter 2)[35].

We set out to distinguish between these two models in BRCA1-deficient cells. We demonstrate a role for primase in promoting PARPi-induced radial chromosomes using auxin-induced degradation of PRIM1. Consistent with fill-in synthesis, incorporation of bromodeoxyuridine (BrdU) occurred at FOKI-induced DSBs and a proximity ligation assay (PLA) for BrdU and γH2AX allowed direct visualization of shieldin/CST/Polα/primase-mediated fill-in synthesis at chromosome breaks in BRCA1-deficient cells. Artificially targeting the STN1 subunit of CST to DSBs induced radial chromosome formation in PARPi-treated BRCA1-deficient cells despite the absence of 53BP1 and shieldin. To further test the involvement of CST downstream of shieldin, we generated a separation of function mutation in SHLD1 that disrupts its interaction with CTC1 and its ability to recruit CST to DSBs. This SHLD1Δ mutant completely abrogated the function of shieldin in BRCA1-deficient cells and its function could be restored by SNAP-HALO tagging of SHLD1Δ and CTC1 and forcing their interaction by chemical-induced dimerization. Remarkably, SHLD1Δ appeared fully functional in processing DSBs in class switch recombination (CSR) and at dysfunctional telomeres, a result we explain based on the unique feature of these DNA ends in that they carry CST recognition sites. These results demonstrate that CST/Polα/primase fill-in synthesis is a major determinant of PARPi efficacy in BRCA1-deficient cells.

3.3 Primase affects radial formation and RAD51 loading in BRCA1-deficient cells

To determine whether primase, like CST and Polα, is involved in the processing of DSBs downstream of 53BP1/shieldin, we generated p53/Rb-deficient RPE1 cells in which the endogenous PRIM1 subunit of primase can be degraded rapidly using the

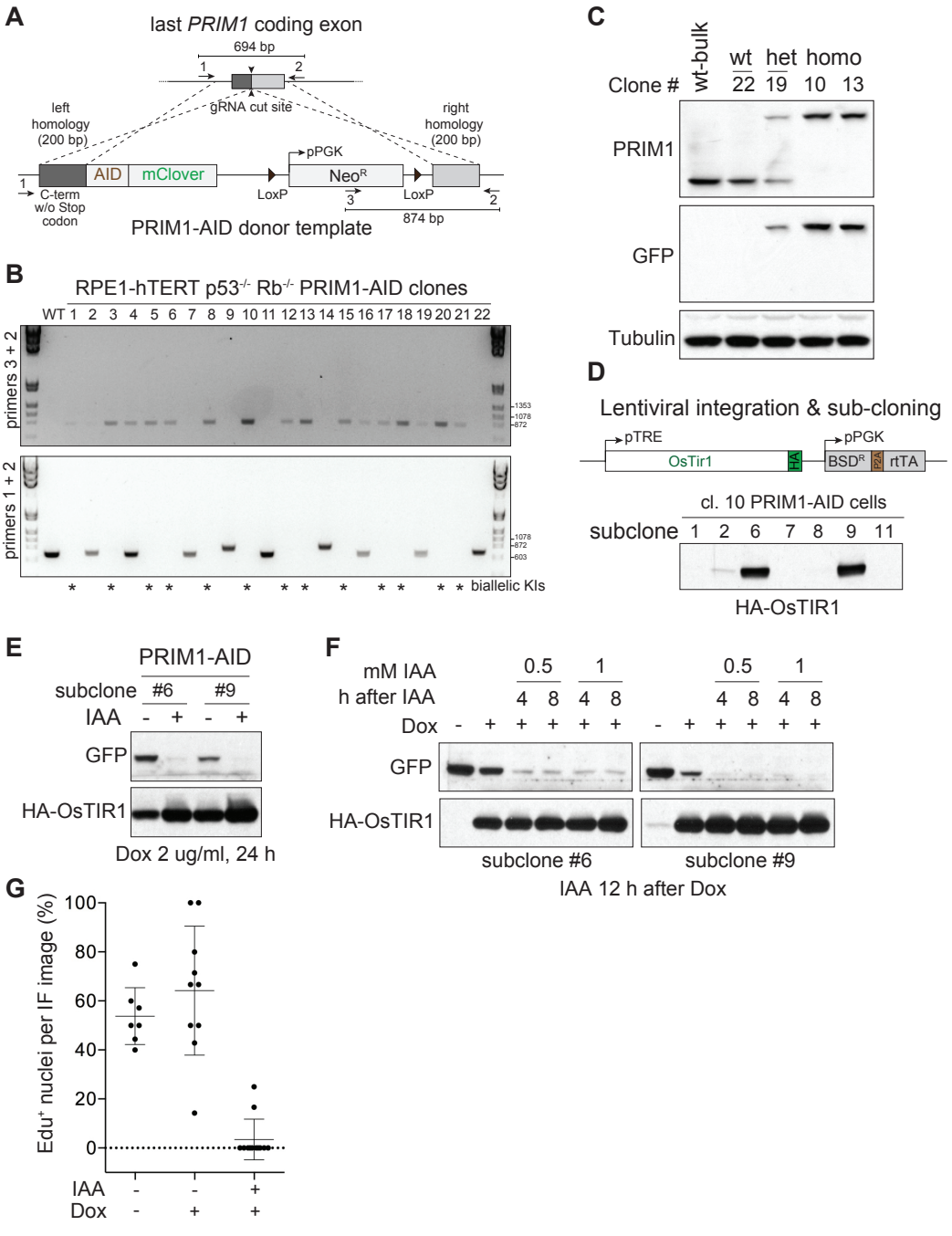

Figure 3.1. Generation and validation of p53/Rb-deficient RPE1 cells with mAID knocked into both PRIM1 loci. A, Experimental scheme used to tag endogenous PRIM1 with mAID-mClover. **B**, PCR genotyping of mClover-positive clones. Location of primer sets and the expected PCR band sizes are shown in **A**. **C**, Immunoblot for mClover-PRIM1 with PRIM1 or anti-GFP antibody. Clone #10, with both copies of PRIM1 tagged with mAID-mClover, was selected for the experiments. **D**, Schematic of HA-OsTIR1 and immunoblot confirming dox-induced HA-OsTIR1 in subclones of PRIM1-AID-mClover clone #10. **E**, Immunoblot for GFP showing efficient PRIM1 degradation after the indicated IAA (auxin)/dox treatments in two subclones. **F**, Immunoblot as in **E** but testing timing and concentration of auxin. **G**, IF showing loss of EdU incorporation in subclone #6 after auxin/dox-induced PRIM1-AID degradation indicating the expected inhibition of DNA replication. Data from one experiment. Experiments performed by Nanda Sasi

TIR/auxin system[168](Figure 3.1). The endogenous *PRIM1* gene was targeted at the C-terminus for fusion with the mAID degron and mClover (Figure 3.1A). After isolation of mClover-positive cells and verification by PCR and immunoblotting (Figure 3.1B, C), a clone that had only the modified PRIM1 but not the wild type protein was chosen for further experimentation. Doxycycline-inducible TIR1 was introduced into this clone and the loss of PRIM1-mClover (detected with a GFP antibody) was verified (Figure 3.1D-F). As expected, degradation of PRIM1 in these cells led to a complete loss of EdU incorporation (Figure 3.1G).

After CRISPR targeting of *BRCA1* in PRIM1-mAID-mClover cells, PRIM1 was degraded in G2-arrested cells (Figure 3.2A). BRCA1-deficient cells, but not the luciferase CRISPR-targeted control, showed characteristic PARPi-induced radial

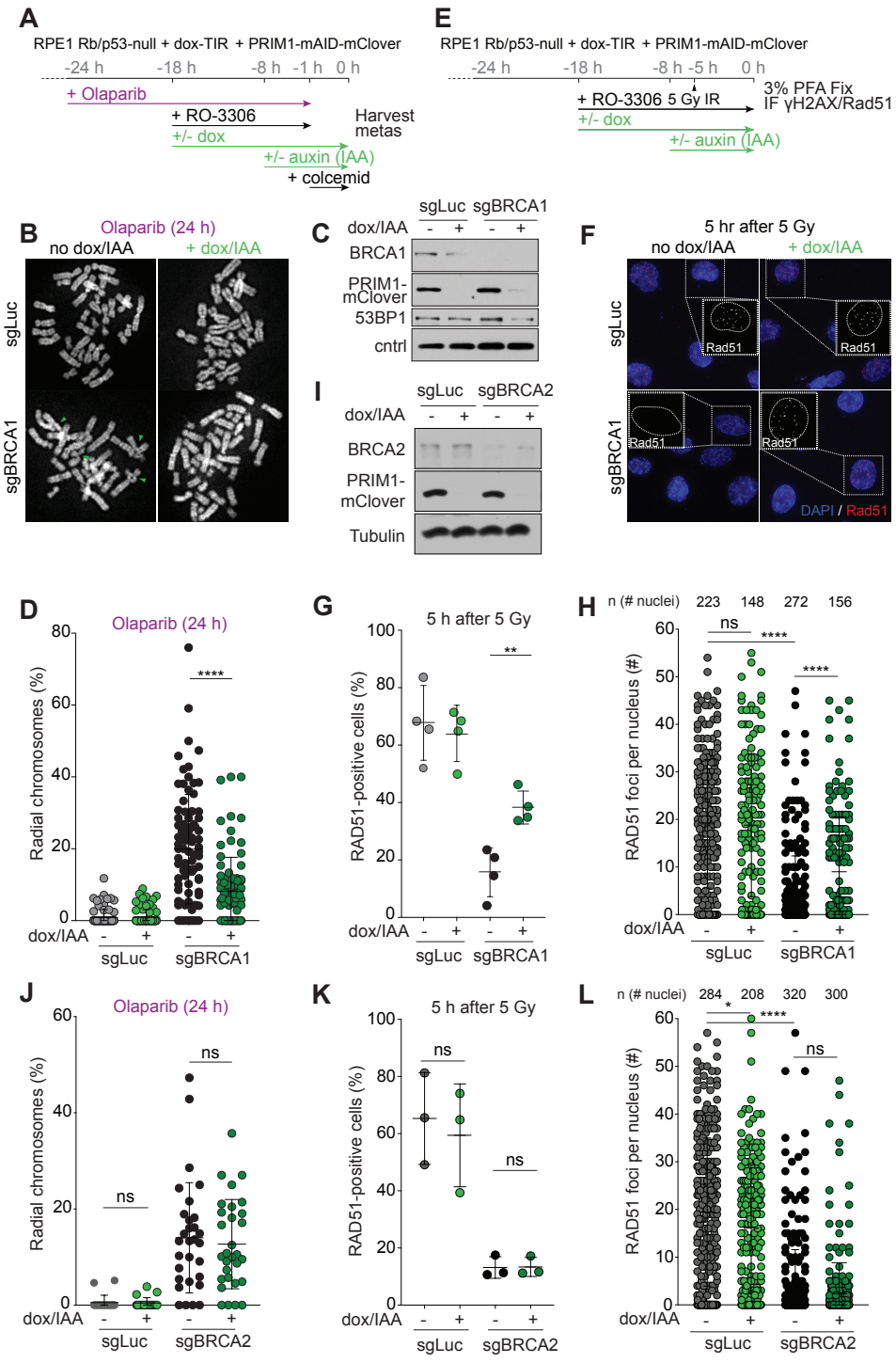

Figure 3.2. Primase promotes radials and blocks RAD51 loading in BRCA1-deficient cells. A, Schematic of the timeline of auxin-induced degradation of PRIM1 in G2-arrested RPE1 cells treated with PARPi. **B**, Representative images of DAPI-stained metaphase spreads from RPE1 PRIM1-mAID-mClover cells with the indicated treatments. Green arrows: aberrant radial chromosomes. **C,** Immunoblot for BRCA1 and GFP (mClover-PRIM1) in cells as in **A** treated with control (sgLuc) or BRCA1 (sgBRCA1) bulk CRISPR KO. ctrl, non-specific band from GFP blot. **D**, Quantification of the percent of chromosomes involved in radial structures. Each dot represents a metaphase spread. Data from at least four independent experiments with at least 75 metaphases per condition. **E**, Experimental timeline of auxin-induced degradation of PRIM1 in G2-arrested RPE1 cells. 5 hr after 5 Gy IR, cells were harvested for RAD51 IF. **F**, Representative images of IF for RAD51 in cells as in **E** with the indicated treatments. **G**, Quantification of the percent of RAD51-positive cells (with 10 or more RAD51 foci per nucleus) 5 h after 5 Gy. Data from four independent experiments with at least 225 nuclei per condition. **H,** Quantification of number of RAD51 foci per nucleus for the cells in **G**. **I**, Immunoblot for BRCA2 and GFP (mClover-PRIM1) in cells as in **A** treated with control (sgLuc) or BRCA2 (sgBRCA2) bulk CRISPR KO. **J**, Quantification of the percent of chromosomes involved in radial structures (as in **D**). Data from three independent experiments with at least 10 metaphases per experiment. **K**, Quantification of the percent of RAD51-positive cells as in **G**, in the indicated cells. Data from three independent experiments with at least 245 nuclei per condition. **L,** Quantification of number of RAD51 foci per nucleus for the cells in **K**. All statistical analysis based on two-tailed Welch's t-test. *, $p<0.05$; **, $p<0.01$; ***, $p<0.001$; ****, $p<0.0001$; ns, not significant. All means are indicated with center bars and SDs with error bars.

chromosomes. PRIM1 degradation significantly diminished radial formation in the BRCA1-deficient cells (Figure 3.2B-D) and restored their ability to form RAD51 foci after ionizing radiation (IR) (Figure 3.2E-H). As a control, we monitored the effect of PRIM1 degradation in the setting of BRCA2 deficiency, where 53BP1 deletion does not reverse the effects of BRCA2 loss[26]. While PARPi treatment induced radial chromosomes in BRCA2-deficient cells, these were not diminished by loss of PRIM1 (Figure 3.2I, J). Furthermore, PRIM1 degradation did not restore RAD51 loading in BRCA2-deficient cells (Figure 3.2K, L). These results establish that primase, like CST/Polα, contributes to the processing of DSBs in BRCA1-deficient cells.

3.4 Direct evidence for shieldin/CST/Polα/primase-dependent fill-in synthesis

A prediction of the fill-in model is that nucleotides are incorporated at DSBs (Figure 3.3A). To test this prediction, we used the inducible mCherry-FOKI-LacI nuclease targeting a LacO array in U2OS cells[169]. Using this system, we previously observed recruitment of CST and Polα to DSBs in G2-arrested cells (Chapter 2; Figures 2.7[35]). Incubation with BrdU during DSB induction in G2-arrested cells (Figure 3.3B) followed by denaturation and IF for BrdU revealed incorporation of nucleotides at DSBs marked by mCherry-FOKI and 53BP1 (Figure 3.3C). S phase cells were easily distinguished by their global BrdU incorporation and excluded from this analysis (Figure 3.3D). The

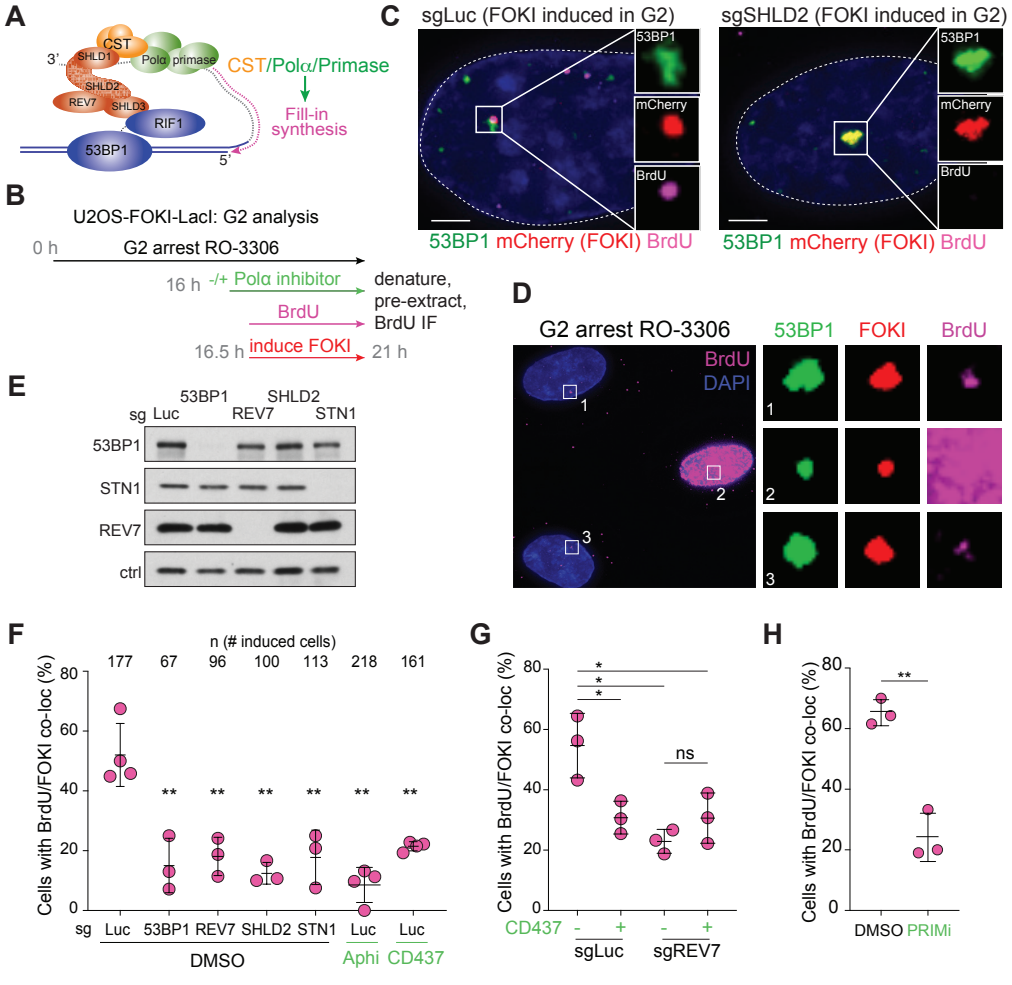

Figure 3.3. 53BP1/shieldin/CST/Polα/primase-dependent fill-in synthesis at FOKI-induced DSBs. A, Schematic of the fill-in synthesis model. Shieldin recruits the CST complex and Polα/primase to counteract resection by copying the 3' overhang. **B,** Experimental timeline for IF to detect BrdU incorporation at DSBs in G2-arrested U2OS cells. **C**, Representative IF of U2OS-FOKI-LacI cells with control (sgLuc) or SHLD2 (sgSHLD2) CRISPR knockout. Cells were arrested in G2 with RO-3306 (9 μM overnight). Scale bars, 5 μm. **D**, Representative IF images of cells as in **a** visualizing DAPI, 53BP1, mCherry-FOKI, and BrdU. The middle cell displays a global BrdU incorporation pattern, indicative of S phase. **E**, Immunoblots showing bulk CRISPR-mediated disruption of the indicated 53BP1 pathway components. No validated antibody to SHLD2 is available. ctrl, non-specific band from REV7 blot. **F**, Quantification of BrdU colocalization with FOKI-induced DSBs as in **E**, in cells treated with the indicated bulk CRISPR or Polα inhibitors, aphidicolin (Aphi) or CD437. Data from three or four independent experiments. S phase cells, identified based on BrdU labeling pattern, were excluded (see **D**). **G**, Quantification of BrdU colocalization with FOKI-induced DSBs as in **F** to determine epistasis of REV7 knockout and Polα inhibition. **H**, Quantification of BrdU colocalization with FOKI-induced DSBs as in **F** upon inhibition of primase with vidarabine triphosphate. Data from three or four independent experiments with at least 30 induced nuclei per experiment. Statistical analyses as in Figure 3.2.

incorporation of BrdU at DSBs depended on the 53BP1/shieldin/CST/Polα axis (Figure 3.3E, F) as revealed by CRISPR bulk targeting or inhibition of Polα by aphidicolin (a B-family polymerase inhibitor) or CD437 (a specific Polα inhibitor[166]). Polα inhibition did not further reduce BrdU incorporation when REV7 was targeted (Figure 3.3G), consistent with BrdU incorporation reflecting 53BP1/shieldin/CST-dependent fill-in synthesis by Polα. In addition, treatment with a selective inhibitor of primase, vidarabine triphosphate[170], strongly reduced BrdU incorporation at FOKI-induced DSBs (Figure 3.3H).

Although global BrdU incorporation during DNA synthesis prevents testing whether fill-in synthesis occurs at DSBs in S phase, we tested whether it can occur in G1. HA-STN1 localized to FOKI-induced DSBs in cells released from CDKi into G1 (Figure 3.4A-C). Cells released into G1—but not yet displaying the BrdU pattern of S

phase cells—showed BrdU enrichment at FOKI-induced DSBs in a manner dependent on Polα (Figure 3.4D, E). The level of incorporation of BrdU at DSBs in this G1-enriched population was slightly lower than in G2-arrested cells (Figure 3.4E). Analysis of Cyclin A-negative cells revealed that a majority of G1 cells display BrdU/FOKI colocalizations and this BrdU incorporation was suppressed by treatment with CD437 (Figure 3.4F, G).

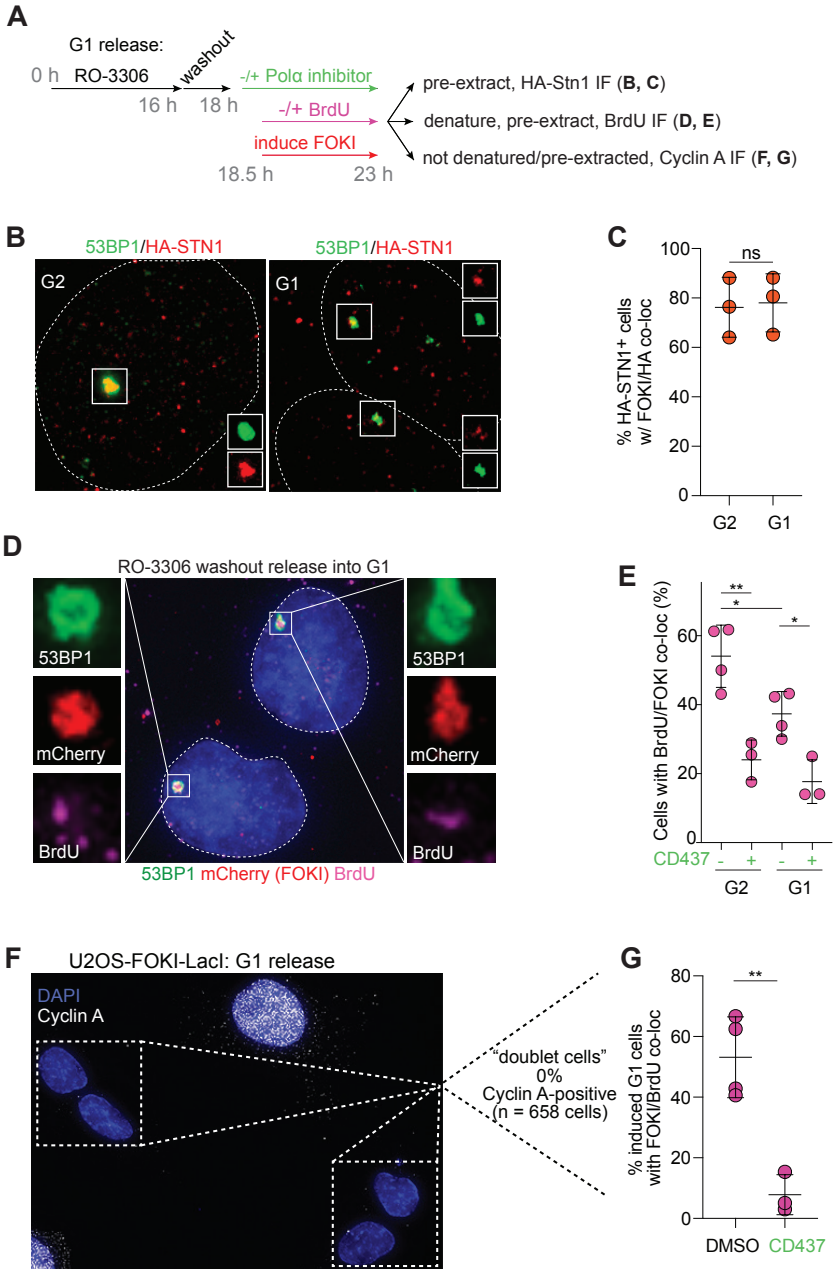

Figure 3.4. Detection of fill-in synthesis in G1 in U2OS-FOKI cells. A, Experimental timeline and IF protocols for U2OS-FOKI-LacI cells released into G1. **B**, Representative IF images of HA-STN1 detected in U2OS-FOKI-LacI cells arrested in G2 with RO-3306 or released into G1 (9 μM RO-3306 overnight followed by washout into fresh media for 2 h before induction of FOKI). Nuclear outlines are demarcated by dashed white lines. **C**, Quantification of HA-STN1 colocalization with FOKI/53BP1 foci in cells as in **B**. Data from three independent experiments. **D**, Representative IF of U2OS cells with FOKI-induced DSB in G2-arrested cells (9 μM RO-3306 overnight) or cells released from RO-3306 into G1 (2 h washout before induction of FOKI, see **A**)**. E**, Quantification of BrdU colocalization with FOKI-induced DSBs as in **D**, with or without Polα inhibitor. **F,** Representative IF for Cyclin A in cells as in **A, D**. Note the two pairs of small, neighboring, "doublet" cells, which in all cases were Cyclin A-negative. Such cell pairs are likely to represent the two daughter cells from a recent mitosis. **G,** Quantification of FOKI/BrdU colocalizations in induced, non-S-phase, "doublet" cells as in **F** after CDKi washout with or without Polα inhibitor. Statistical analyses as in Figure 3.2.

Given the strong suppression of fill-in in G1 by CD437, we infer that some of the residual BrdU signal in G2-arrested cells treated with CD437 (Figure 3.4E) is likely due to other DNA repair pathways (e.g., HDR) that are inactive in G1.

We next aimed to detect BrdU incorporation at chromosome breaks in metaphase spreads of BRCA1-deficient, PARPi-treated cells. To this end, we combined a protocol for γH2AX IF on metaphase spreads[171–173] with PLA for detecting γH2AX and BrdU antibodies in close proximity (< 40 nm). To test this "metaPLA" protocol, we used the induction of γH2AX foci at dysfunctional telomeres in *Trf2*$^{F/F}$ *Lig4*$^{-/-}$ MEFs treated with Cre[66]. After BrdU incubation for 24 h to label all DNA, numerous BrdU-γH2AX PLA foci were observed at chromosome ends (Figure 3.5A, B), demonstrating that this assay is specific for sites of DNA damage and does not yield false positive signals in MEFs.

To monitor fill-in at DSBs in PARPi-treated BRCA1-deficient cells, metaphases were harvested after a short pulse (1 h) of BrdU, thereby avoiding confounding signals derived from S phase cells. BRCA1-deficient PARPi-treated metaphase spreads

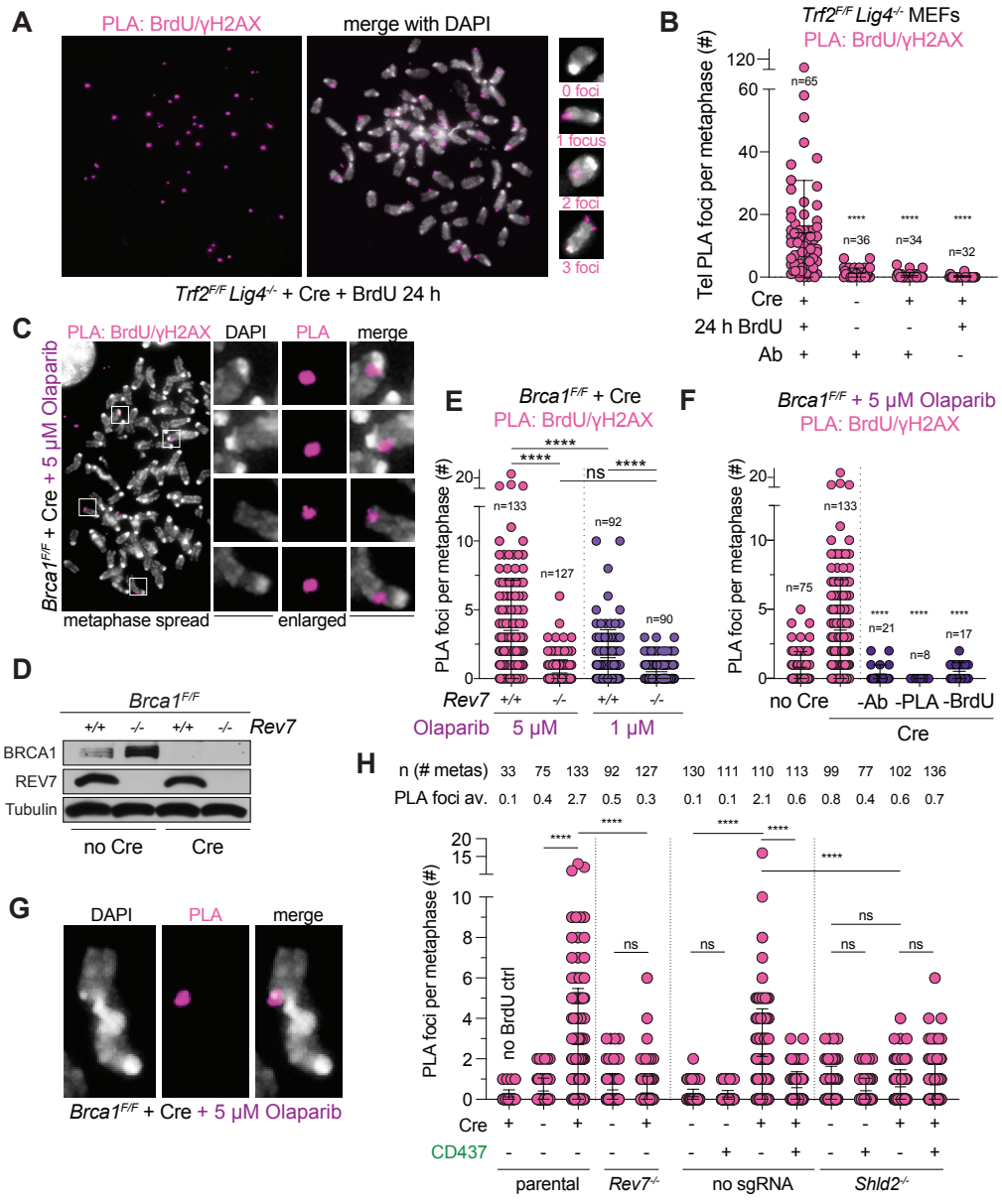

Figure 3.5. MetaPLA for detection of fill-in synthesis in BRCA1-deficient mouse cells. A, B, Experiments to validate the BrdU/γH2AX metaPLA protocol in MEFs. **A,** Representative images from metaPLA of BrdU/γH2AX on metaphase spreads in *Trf2*$^{F/F}$ *Lig4*$^{-/-}$ MEFs with the indicated treatment that were used to validate the technique. **B**, Quantification of terminal, chromatin-associated BrdU/γH2AX PLA foci for cells as in **A**. Number of metaphases scored in each condition is indicated (n). Data from three independent experiments. **C**, Representative image from metaPLA of BrdU/γH2AX on metaphase spreads in *Brca1*$^{F/F}$ MEFs treated as indicated. **D**, Immunoblot for BRCA1 and REV7 in the indicated cells with or without Cre treatment. **E**, Quantification of chromatin-associated BrdU/γH2AX PLA foci on metaphase spreads in *Brca1*$^{F/F}$ MEFs of the indicated genotype, with 5 or 1 μM Olaparib. **F**, BrdU/γH2AX PLA controls quantified as in **E**. **G**, Example of a dicentric chromosome from a metaphase spread showing a PLA signal at a break. **H**, Quantification of BrdU/γH2AX metaPLA foci at chromatin breaks from cells with the indicated genotypes and treatments. Data from three independent experiments. Number of metaphases analyzed per condition (n) and the average number of PLA foci at breaks per metaphase are indicated. Statistical analysis as in Figure 3.2, except in panel **H**, where ordinary one-way ANOVA with Tukey's multiple comparisons test was used. p values are as in Figure 3.2.

showed BrdU-γH2AX PLA foci co-localizing with DAPI-stained chromosomal material (Figure 3.5C, D). PLA foci were dependent on the PARPi dose, BrdU, primary antibodies, and PLA probes (Figure 3.5E, F). Many PLA foci co-localized with gaps in DAPI staining or were present at the ends of broken chromosomes (Figure 3.5G). BrdU-γH2AX metaPLA foci did not form in cells lacking REV7 or SHLD2 or when Polα was inhibited (Figure 3.5D, E, H). Similarly, BrdU-γH2AX metaPLA foci at breaks and gaps were eliminated by auxin-mediated degradation of primase in human cells (Figure 3.6).

These results indicate that shieldin and its downstream effectors CST/Polα/primase mediate the incorporation of nucleotides at FOKI- and PARPi-induced DSBs.

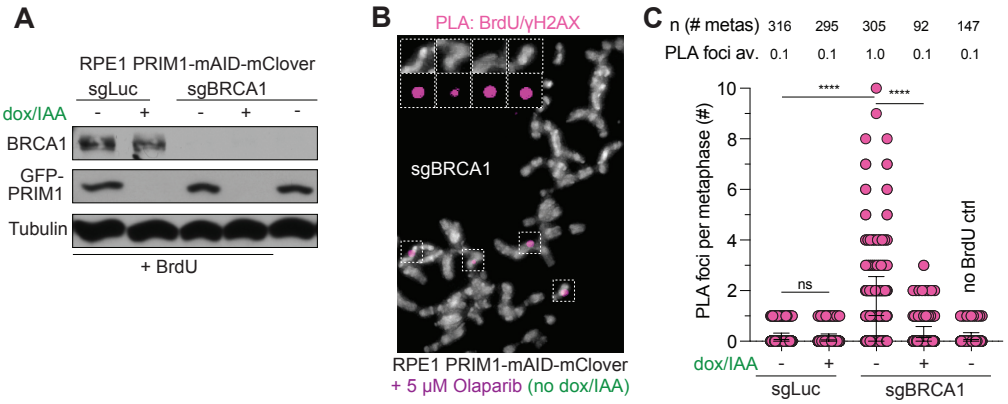

Figure 3.6. Detection of primase-dependent fill-in synthesis in BRCA1-deficient human cells. **A**, Immunoblots for BRCA1 and GFP (mClover-PRIM1) in the indicated cells lines. **B,** Representative image from metaPLA of BrdU/γH2AX on metaphase spreads in RPE1 PRIM1-mAID-mClover cells treated with sgBRCA1, BrdU, and Olaparib. **C**, Quantification of BrdU/γH2AX metaPLA foci at chromatin breaks in cells as in **B** with the indicated genotypes and treatments. Data from three independent experiments. Number of metaphases analyzed per condition (n) and the average number of PLA foci at breaks per metaphase are indicated. Statistical analyses as in Figure 3.2.

The incorporation of BrdU at chromosome breaks in the 1 h time interval before metaphase indicated that fill-in synthesis occurs in late G2 or early M. We previously determined that inhibition of Polα *during* G2 arrest by CDKi reduced radial chromosome formation (Figure 2.10). Building on this finding, Polα inhibition *after* CDKi removal significantly diminished the formation of radial chromosomes (Figure 3.7A, B). We next determined whether Polα acts before or after nuclear envelope (NE) breakdown, which, based on IF for laminA/C, reaches a plateau at 30 min after release from CDKi (Figure 3.7C, D) as did the formation of RAD51 foci in cells treated with CD437 (Figure 3.7C-E).

This suggests that most cells that exit G2 arrest in this protocol do so within 30 min after release from CDKi. Polα inhibition within this short window reduced radial chromosome formation, while Polα inhibition after NE breakdown had no effect on radial chromosome

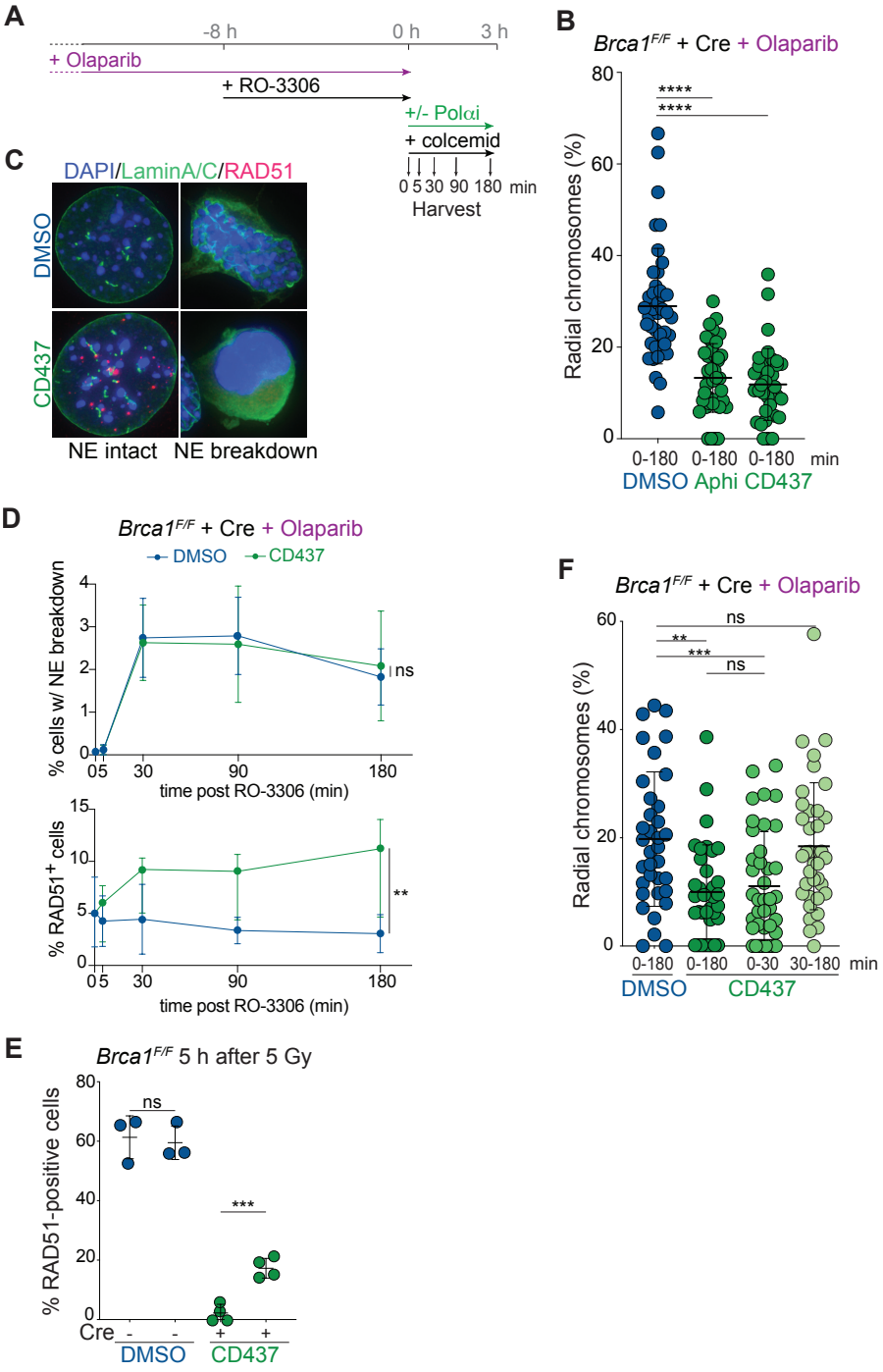

Figure 3.7. Fill-in synthesis occurs late in G2 in BRCA1-deficient cells. A, Experimental timeline for Polα inhibition in PARPi-treated, BRCA1-deficient MEFs released from G2 into prolonged (180 min) metaphase arrest. **B**, Quantification of the percent of chromosomes involved in radial structures. Each dot represents a metaphase spread in three independent experiments with at least 12 metaphases analyzed per experiment. **C**, Representative sample images of nuclei with intact or broken-down nuclear envelopes (NE) as assessed by Lamin A/C IF. **D**, Top, analysis of NE breakdown timing after release from G2 in cells as in **A** and **C** assessed at the indicated time points. Bottom, analysis of RAD51 foci formation in the same population of cells. Data from three independent experiments. For NE breakdown, Lamin A/C integrity was visually assessed in at least 800 cells per condition per experiment. **E**, Quantification of RAD51-positive nuclei in *Brca1*$^{F/F}$ MEFs following treatment with Cre and IR. Data from three or four independent experiments. **F**, Quantification of percent of chromosomes involved in radial structures after the indicated treatment. Data from three or four independent experiments with at least 12 metaphases analyzed per experiment. Statistical analyses as in Figure 3.2.

formation (Figure 3.7F), indicating that the Polα-dependent DNA repair steps take place in G2 right before or during NE breakdown, but not after.

3.5 Tethering of CST to DSBs can bypass the requirement for 53BP1/shieldin in BRCA1-deficient cells

It was previously shown that targeting human SHLD2 to DSBs using the forkhead-associated (FHA) domain of RNF8 (which targets proteins to phosphorylated MDC1 at DSBs) could bypass the need for recruitment of shieldin by 53BP1[91]. We first confirmed that tethered shieldin can function in the absence of 53BP1 in BRCA1-deficient MEFs. As expected, FHA-tethering of SHLD1 induced radial formation in BRCA1/53BP1 double-deficient cells, and this effect was abolished when the FHA domain was mutated (R61Q) to abrogate the interaction with MDC1 (Figure 3.8A-C). Strikingly, Polα inhibition completely reversed the radial chromosomes induced by FHA-SHLD1 (Figure 3.8D, E).

Next, we tested whether CST could promote radial formation in BRCA1-deficient cells independently of 53BP1/shieldin. Expression of FHA-STN1, which localized to

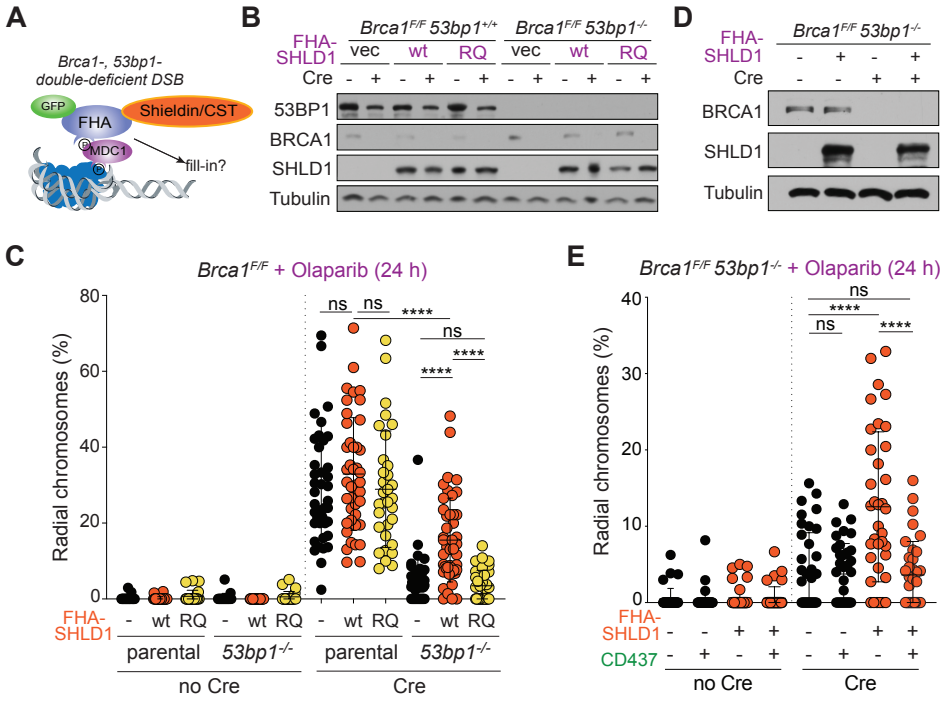

Figure 3.8. Bypass of 53BP1 by artificial tethering of SHLD1. A, Schematic of 53BP1/shieldin-independent recruitment of FHA-fusions to phosphorylated MDC1 at DSBs. **B**, Immunoblots for BRCA1, 53BP1, and SHLD1 detecting FHA-SHLD1 in the indicated MEFs expressing FHA-R61Q-SHLD1 (RQ) corresponding to **C**. **C**, Quantification of the percent of chromosomes involved in radial structures in the indicated cell lines with wt FHA-SHLD1 or FHA-SHLD1 with an FHA domain mutation (R61Q) which prohibits recruitment to DSBs. Each dot represents a metaphase spread. **D**, Immunoblots for BRCA1 and SHLD1 detecting FHA-SHLD1 in the indicated MEFs, corresponding to **E**. **E**, Quantification as in **C** in *Brca1*$^{F/F}$ *53bp1*$^{-/-}$ cells with or without FHA-SHLD1 and Polα inhibitor. Data is from at least three independent experiments with at least 5 metaphases analyzed for each no Cre condition, and at least 10 metaphases analyzed for each + Cre condition per experiment. Statistical analyses as in Figure 3.2.

DSBs (Figure 3.9), restored radial formation in PARPi-treated *Brca1*$^{-/-}$ *53bp1*$^{-/-}$ and *Brca1*$^{-/-}$ *Shld2*$^{-/-}$ clones, indicating the CST can function independently of 53BP1 and shieldin (Figure 3.10A, B). FHA-STN1 also sensitized these cells to PARPi and suppressed RAD51 loading (Figure 3.10C, D). Shieldin-independent radial formation by FHA-STN1 was fully dependent on Polα activity (Figure 3.10E-G). The frequency of

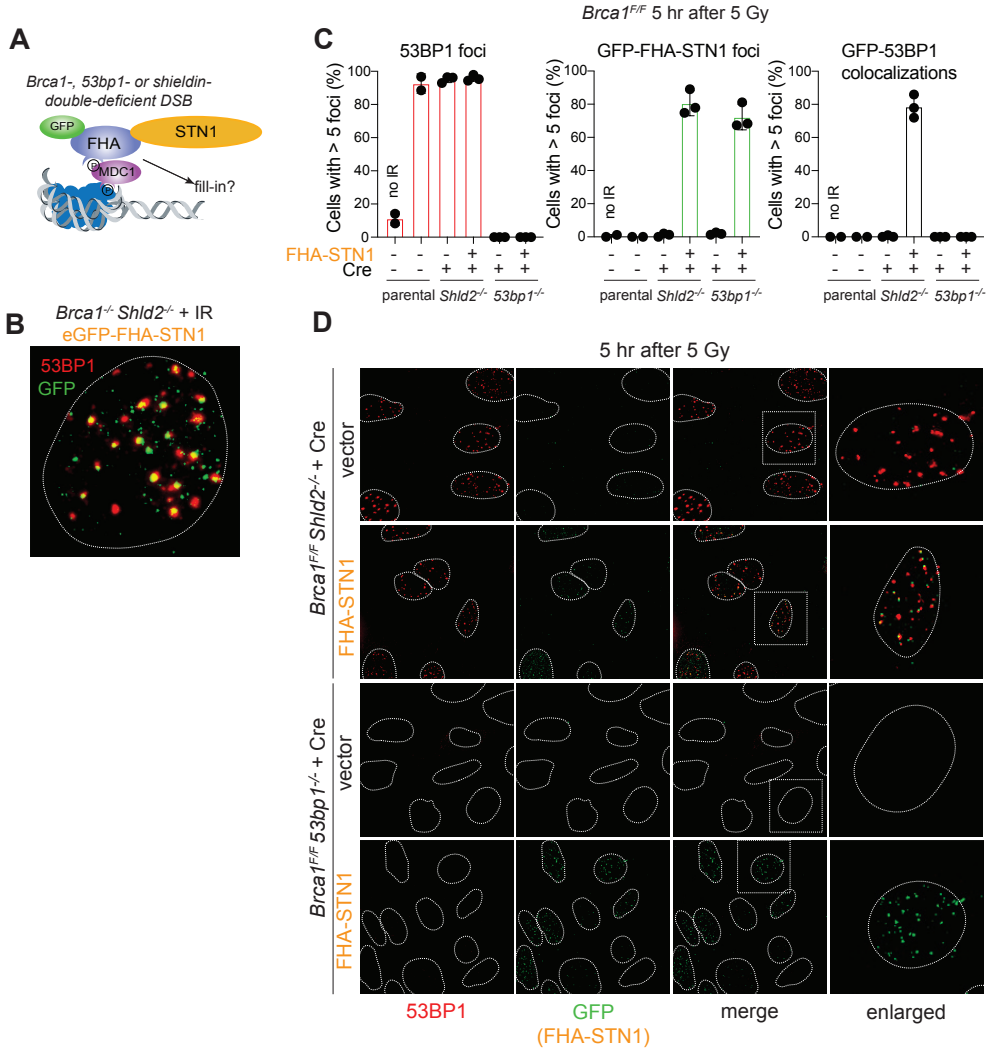

Figure 3.9. FHA-STN1 localizes to IR-induced DSBs independently of 53BP1/shieldin. A, Schematic of 53BP1/shieldin-independent recruitment of FHA-STN1 to phosphorylated MDC1 at DSBs. **B,** Representative image of irradiated *Brca1*$^{-/-}$ *Shld2*$^{-/-}$ cells harboring eGFP-FHA-STN1, which colocalizes with 53BP1 IR-induced foci. The nucleus is demarcated by the dashed white line. **C,** Quantification of 53BP1 and GFP-FHA-STN1 foci at DSBs in the indicated MEFs after IR. **D,** Representative images of irradiated *Brca1*$^{F/F}$ *Shld2*$^{-/-}$ or *Brca1*$^{F/F}$ *53BP1*$^{-/-}$ MEFs as in **C**. Nuclear outlines are demarcated by dashed white lines. An additional enlarged and merged image is shown in **B**.

radials induced by both FHA-STN1 and FHA-SHLD1 in these experiments was slightly lower than what is observed when the endogenous 53BP1, shieldin, and CST were present (Figure 3.8C; Figure 3.10B). This may indicate that the FHA fusion proteins are

somewhat impaired in their function and/or recruitment. Collectively, the FHA-tethering experiments show that CST/Polα/primase can promote DSB processing in the absence of 53BP1 and shieldin.

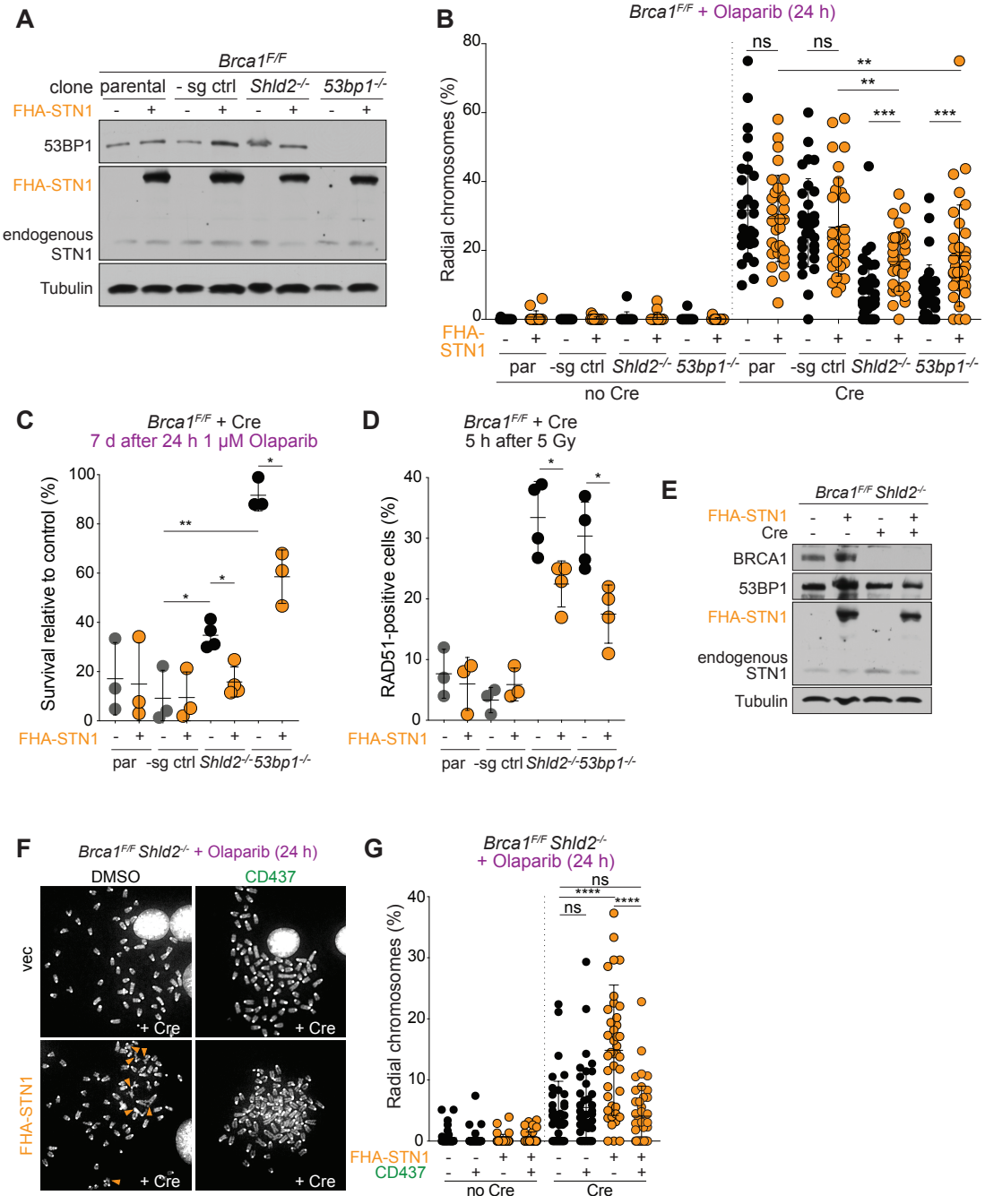

Figure 3.10. Bypass of 53BP1/shieldin by artificial tethering of CST. A, Immunoblots for BRCA1, 53BP1, and (FHA-)STN1 in the indicated MEFs. **B,** Quantification of the percent of chromosomes involved in radial structures in the indicated cell lines with or without FHA-STN1. **C,** Quantification of colony formation by MEFs of the indicated genotype with or without FHA-STN1 and treated with 1 μM Olaparib for 24 h. Survival after PARPi was compared to undrugged cells. **D,** Quantification of the percent of RAD51-positive cells in irradiated MEFs of the indicated genotype with or without FHA-STN1. **E**, Immunoblots for BRCA1, 53BP1, and STN1 detecting endogenous and FHA-STN1 in *Brca1*$^{F/F}$ *Shld2*$^{-/-}$ MEFs. **F,** Representative images of DAPI-stained metaphase spreads from cells as in **E** corresponding to data in **G**. **G**, Quantification of radial chromosome formation as in **B** in *Brca1*$^{F/F}$ *Shld2*$^{-/-}$ cells with or without FHA-STN1 and Polα inhibitor. In **B** and **G,** data is from at least three independent experiments with at least 5 metaphases analyzed for each no Cre condition, and at least 10 metaphases analyzed for each + Cre condition per experiment. Statistical analyses as in Figure 3.2.

3.6 SHLD1 function in BRCA1-deficient cells requires its interaction with CTC1

To determine the importance of the shieldin-CST interaction in BRCA1-deficient cells, we used a yeast two-hybrid random mutagenesis screen to identify a human SHLD1 mutant defective for the interaction with CTC1(Figure 3.11A), a major interface between CST and shieldin (Chapter 2, Figure 2.6[35]). A Gal4 activation domain (GAD)-SHLD1 vector[35] was modified to contain scUra3 in frame with the C-terminus of SHLD1 so that only full-length variants of SHLD1 would be recovered after growth on media lacking uracil. A library of SHLD1 ORFs generated by error-prone PCR was screened for SHLD1 mutants that failed to interact with CTC1 (Figure 3.11B), yielding a clear mutation hotspot of conserved residues (aa 18-21 LDLP) in the N-terminus of SHLD1 (Figure 3.11B, C). Additionally, deletion of nearby A23, the mutations A119V or Q127L, or the L20P mutation alone abrogated the SHLD1-CTC1 interaction (Figures 3.11B; 3.12A). Since L20 resides in a conserved patch of four residues, LDLP (Figure 3.11C), we deleted this motif in subsequent experiments.

SHLD1ΔLDLP (hereafter SHLD1D) was expressed at the same level as wild-type (wt) SHLD1 (Figure 3.12B, C), was recruited to IR-induced DSBs equally (Figure 3.12D),

Figure 3.11. Identification of a SHLD1 mutant with impaired CTC1 interaction. **A**, Schematic of 53BP1 and its downstream effectors. Interactions (lines) based on previous reports[35, 89, 91, 92, 105, 119, 120]. Black lines, interactions demonstrated by coimmunoprecipitation; purple lines, interactions demonstrated by yeast two-hybrid (Figure 2.5, 2.6)[35]. Asterisk denotes the SHLD1-CTC1 interaction targeted for disruption in the random mutagenesis screen in **B**. **B**, Mutants identified in a yeast two-hybrid screen for loss of CTC1 binding executed with a randomly mutagenized human SHLD1 ORFs. Left, candidate GAD-SHLD1-URA3 variants (red numbers) grow on permissive (-leucine, -tryptophan, -uracil) media. Expression of full-length SHLD1 variants is ensured by growth on media lacking uracil. Several controls are also shown (black numbers, e.g., c1a). Variants that fail to grow on selective (-leucine, -tryptophan, -uracil, -adenine) media are indicated with a green circle (or triangle for deletion). Five sequenced variants were attributable to a single mutation (green shape with magenta border). Right, sequence alignment of human and mouse SHLD1 with conserved residues highlighted in yellow. SHLD1 sequence variants are represented graphically by shapes above the sequence (see legend at bottom). **C**, Multiple sequence alignment of SHLD1. Conservation symbols are according to Uniprot: asterisks, fully conserved; colon, strong similarity; period, weak similarity. The orange outline highlights the conserved LDLP motif deleted in the SHLD1Δ mutant used in the following figures.

and retained its interaction with the C-terminus of SHLD2[91](Figure 3.12E). SHLD1Δ showed a diminished interaction with CTC1 by co-immunoprecipitation (Figure 3.12E). To test whether SHLD1Δ is defective in the recruitment of CST to DSBs, the colocalization of HA-tagged STN1 with γH2AX after IR was monitored. When SHLD1-deficient cells were complemented with SHLD1Δ, CST recruitment to IR-induced DSBs was diminished (Figure 3.12G, H). This effect was seen in a BRCA1-proficient clone lacking SHLD1 but was more pronounced in a clonal *BRCA1/SHLD1* DKO RPE1 cell line (Figure 3.12G, H). SHLD1 KO clones were generated by CRISPR and confirmed by Sanger sequencing (data not shown). The formation of γH2AX foci was similar in all conditions, indicating that the upstream steps in DSB signaling were unaffected (Figure 3.12I).

To determine whether shieldin was able to function normally at DSBs in BRCA1-deficient cells when its interaction with CST was severed, the formation of RAD51 foci was monitored in cells expressing SHLD1Δ. As expected, RAD51 loading was not affected upon expression of wt SHLD1 or SHLD1Δ in BRCA1-proficient cells or in

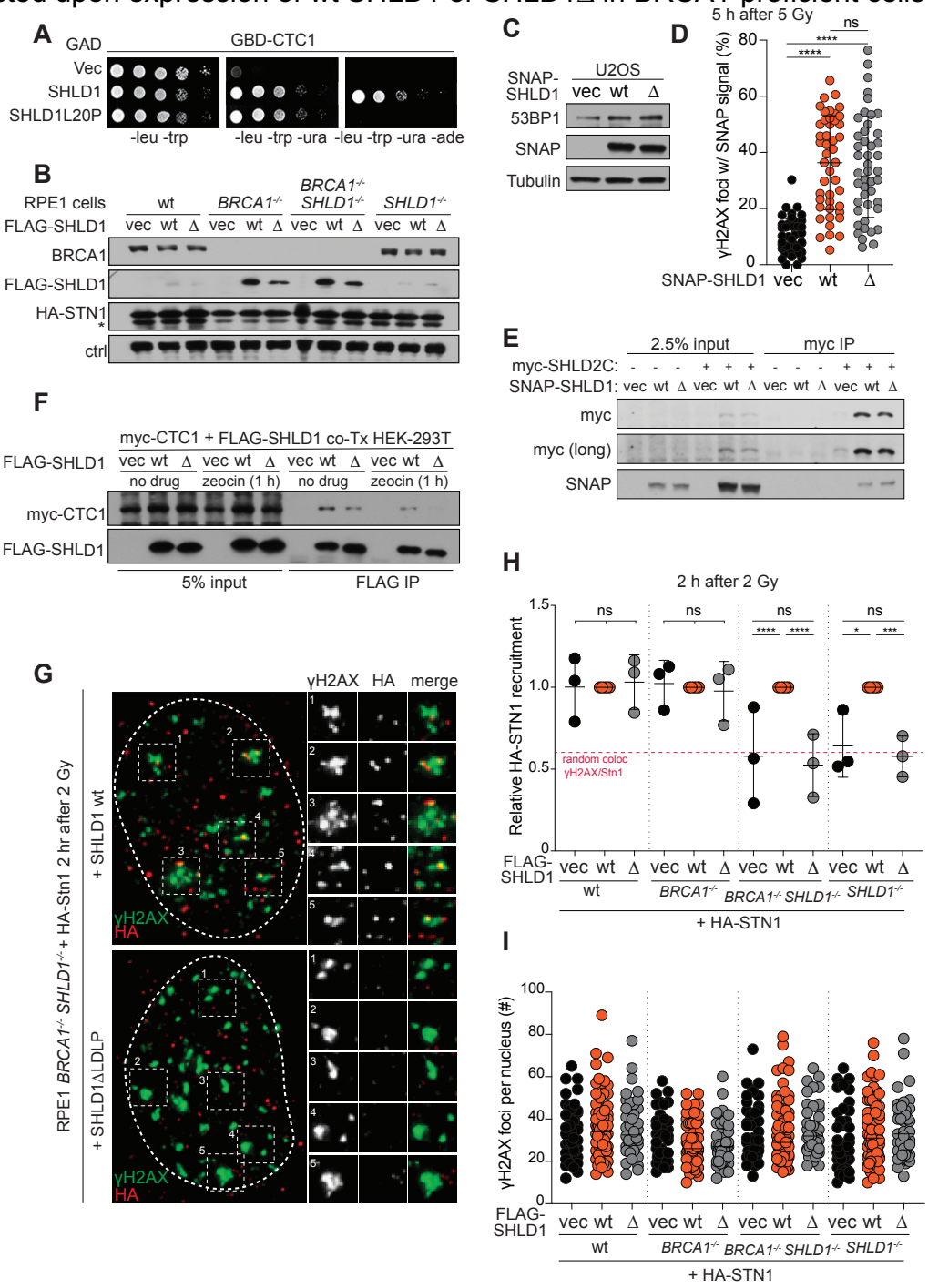

Figure 3.12. Characterization of SHLD1Δ. A, Yeast-two hybrid assay demonstrating lack of interaction between human SHLD1L20P and CTC1 proteins. Colony growth on permissive (-leucine, -tryptophan, -uracil) media, but not on selective (-leucine, -tryptophan, -uracil, -adenine) media indicates lack of interaction. **B**, Immunoblots showing expression of SNAP-SHLD1 or SNAP-SHLD1ΔLDLP (Δ) in U2OS cells. **C**, Quantification of SNAP-SHLD1 localization to IR-induced γH2AX foci in cells as in **B**. **D**, Immunoblots in RPE1 cells of the indicated genotypes with the indicated FLAG-SHLD1 constructs. SHLD1Δ (Δ) has a deletion of aa 18-21 (LDLP). ctrl, non-specific band from STN1 blot. **E**, Immunoprecipitation of FLAG-SHLD1 and immunoblot for myc-CTC1 co-expressed in 293T cells. **F,** Immunoprecipitation of myc-SHLD2C (aa 421-904) and immunoblot for SNAP-SHLD1 co-expressed in 293T cells. **G**, Representative IF images showing γH2AX co-localizing with HA-STN1 in irradiated *BRCA1/SHLD1* DKO cells complemented with wt SHLD1 or SHLD1Δ. Nuclear outlines are demarcated by dashed white lines. Five sample foci are shown for each nucleus. **H,** Quantification of recruitment of HA-STN1 to IR-induced γH2AX foci in the indicated RPE1 cells transfected with the indicated FLAG-SHLD1 constructs or vector (vec) control. Each dot represents one of three independent experiments. Red dotted line: the average background level across multiple conditions of random overlaps between γH2AX and HA foci (see Materials and Methods). The data from *BRCA1/SHLD1* DKO cells is reproduced in Figure 3.13**A**. **I**, Quantification of γH2AX foci in the indicated RPE1 cells with HA-STN1 as in **H**.

BRCA1-deficient cells with intact SHLD1 (Figure 3.13A). However, the formation of RAD51 foci in *BRCA1/SHLD1* DKO cells was fully repressed by expression of wt SHLD1, but SHLD1D failed to repress RAD51 loading (Figure 3.13B-D). Concordantly, wt SHLD1 induced radial chromosome formation while SHLD1Δ did not(Figure 3.13D, E). Finally, wt SHLD1 sensitized *BRCA1/SHLD1* DKO cells to PARPi, while SHLD1Δ did not (Figure 3.13F). To test whether SHLD1Δ was able to bypass the loss of 53BP1 as wt SHLD1 did (Figure 3.8), we introduced FHA-tagged mouse SHLD1 or SHLD1Δ into *Brca1*$^{-/-}$ *53bp1*$^{-/-}$ MEFs, and the constructs were expressed at similar levels (Figure 3.13G). Upon treatment with PARPi, FHA-SHLD1 induced radial chromosomes, whereas FHA-SHLD1Δ was completely deficient in promoting radials in this setting (Figure 3.13H).

To verify that the defect of SHLD1Δ in BRCA1-deficient cells is solely in the recruitment of CTC1, the interaction between CTC1 and SHLD1Δ was restored through a SNAP-HALO chemical-induced dimerization (CID) system[174](Figure 3.13I). Addition of

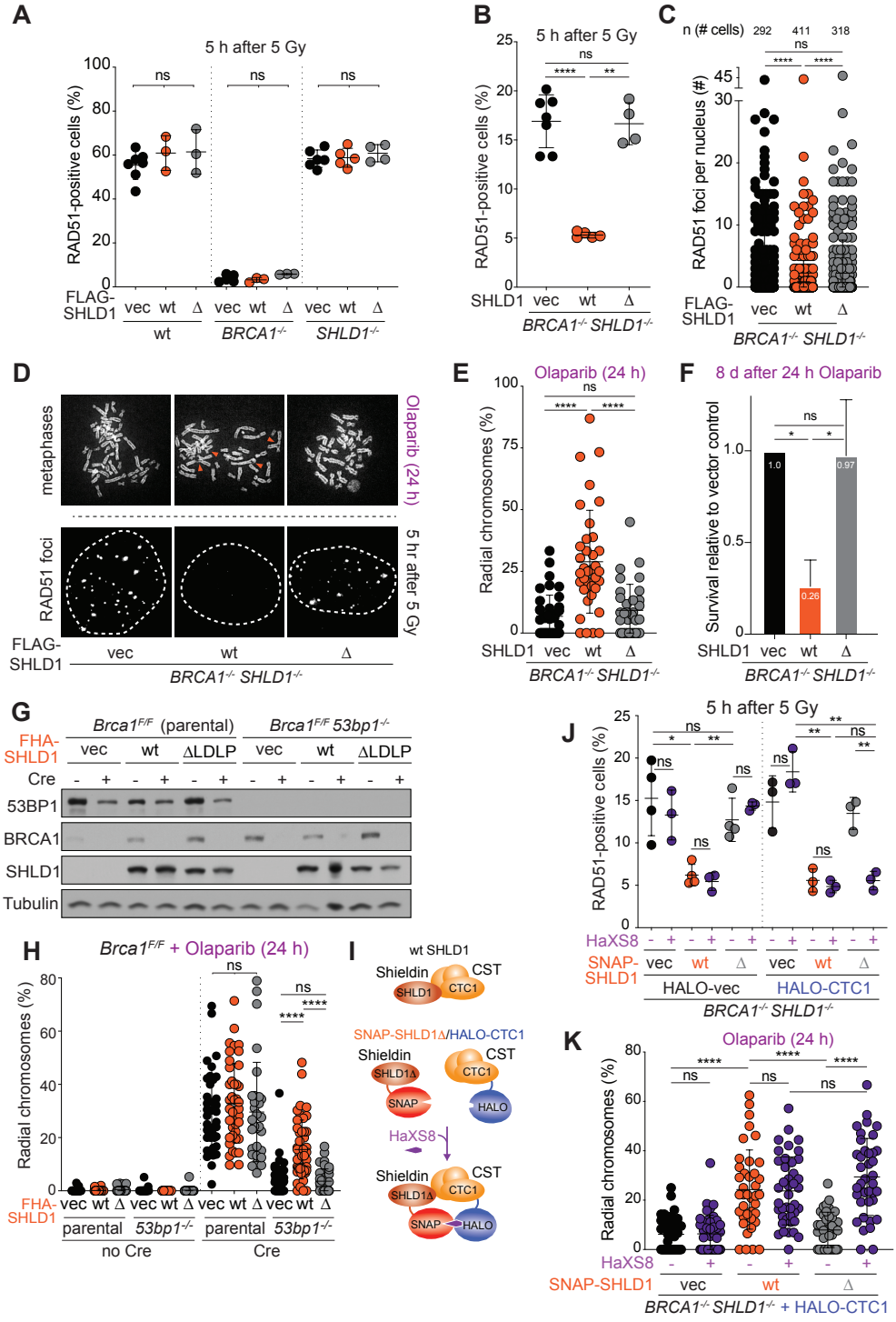

Figure 3.13. Shieldin function in BRCA1-deficient cells depends on CST/Polα/primase. A, Quantification of recruitment of HA-STN1 to IR-induced γH2AX foci in *BRCA1/SHLD1* DKO cells. **B**, Quantification of the percent of RAD51-positive cells in irradiated parental (wt), *BRCA1* KO, or *SHLD1* KO RPE1 cells, complemented with the indicated FLAG-SHLD1 construct or an empty vector. For **A** and **B**, ordinary one-way ANOVA was performed with Tukey's correction for multiple comparisons. Each dot represents one of three-five independent experiments. Red dotted line: the average background level across multiple conditions due to randomly overlapping γH2AX and HA foci (see Materials and Methods). **C**, Quantification of the percent of RAD51-positive cells in irradiated *BRCA1/SHLD1* DKO RPE1 cells, complemented with the indicated FLAG-SHLD1 construct or an empty vector. Each dot represents an independent experiment (four-seven experiments involving >60 cells each). **D,** Quantification of the number of RAD51 foci per nucleus for cells as in **C** with the indicated FLAG-SHLD1 constructs. **E,** Representative images of DAPI-stained metaphase spreads (top; orange arrows denote aberrant radial chromosomes) or RAD51 foci (bottom; nuclear outlines demarcated by dashed white lines) in *BRCA1/SHLD1* DKO cells complemented with an empty vector control, wt SHLD1, or SHLD1Δ. Data from three or more independent experiments for all panels. **F**, Quantification of the percent of chromosomes in radial structures in *BRCA1/SHLD1* DKO cells, complemented with the indicated SHLD1 construct or the empty vector (vec). Data from three experiments with 10-15 metaphases per experiment analyzed. **G,** Quantification of colony formation by *BRCA1/SHLD1* DKO cells, complemented with the indicated SHLD1 construct or an empty vector, and treated with 1 μM Olaparib for 24 h. Survival after PARPi was compared to undrugged cells and then normalized to empty vector. **H**, Immunoblot for BRCA1, 53BP1, and SHLD1 detecting FHA-tagged SHLD1 in the indicated cells. **I**, Quantification of the percent of chromosomes in radial structures in the indicated MEFs expressing FHA-SHLD1Δ (Δ). For reference, empty vector (vec) and FHA-SHLD1 (wt) conditions from Figure 3.8**C** are provided again here. Data from three or four independent experiments with at least 12 metaphases analyzed per condition per experiment. **J**, Schematic of HaXS8-induced dimerization of SNAP-SHLD1Δ with HALO-CTC1. **K,** Quantification of RAD51-positive cells in irradiated *BRCA1/SHLD1* DKO cells, complemented with the indicated SNAP-SHLD1 or an empty vector, and HALO-CTC1 or an empty vector, then treated with HaXS8 or vehicle prior to irradiation. **L**, Quantification of the percent of chromosomes in radial structures in *BRCA1/SHLD1 DKO* cells with the indicated treatments. Unless otherwise stated, statistical analyses as in Figure 3.2.

the chemical dimerizer (HaXS8) fully restored the ability of SNAP-SHLD1Δ to suppress RAD51 loading in *BRCA1/SHLD1* DKO cells expressing HALO-CTC1 and rescued PARPi-induced radial chromosome formation (Figure 3.13I-K). This result indicates that at DSBs in BRCA1-deficient cells, the primary function of SHLD1 is recruitment of

CTC1. The sufficiency of CST recruitment for radial formation (Figure 3.10) combined with these SHLD1 separation of function studies supports a central role for CST/Polα/primase downstream of 53BP1/shieldin in BRCA1-deficient cells.

53BP1/shieldin also promotes CSR[89,90,99,105]. We therefore introduced SHLD1Δ into SHLD1-deficient CH12F3 cells, a murine B cell lymphoma line that upon stimulation with anti-CD40 antibody, IL-4, and TGFβ1 undergoes efficient IgM to IgA class switching, detectable based on FACS for IgA (Figure 3.14A). Interestingly, expression of SHLD1Δ—or a large N-terminal truncation of SHLD1 that includes the LDLP motif deleted in SHLD1Δ—restored CSR to the same extent as the wt SHLD1 (Figure 3.14A, B). In this context, no interaction was detected between immunoprecipitated wt SHLD1 or SHLD1Δ and CST (Figure 3.14C). The immunoprecipitates were evaluated using a STN1 antibody because no validated antibody to mouse CTC1 is available (Figure 3.14C). REV7, a positive control for the interaction of shieldin proteins with SHLD1, was detected with each mutant (Figure 3.14C). Given the negative co-IP result for STN1 with wild type SHLD1, we have no information on whether the mutants abrogate the interaction of SHLD1 with CTC1 in these cells.

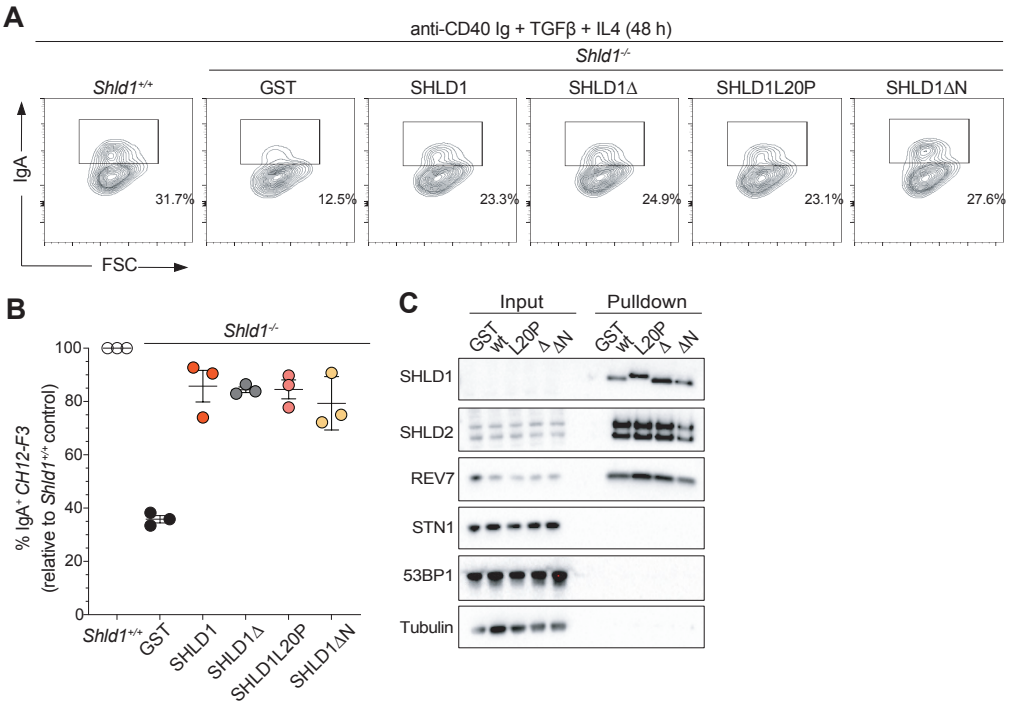

Figure 3.14. SHLD1Δ supports class switch recombination. A, Representative flow cytometry plots of IgM to IgA CSR in indicated parental *Shld1*$^{+/+}$, *Shld1*$^{-/-}$ and transgene-complemented *CH12-F3* cell line derivatives. **B,** Quantification of CSR in cells as in **A**. CSR efficiency is normalized to wild-type cells. **C,** TwinStrep-HA-SHLD1 wt, L20P, ΔLDLP, or ΔN immunocomplexes were isolated from whole cell extracts prepared from untreated *CH12-F3* cultures. Western blots were probed for the indicated targets. Data representative of three independent experiments. Experiments performed by Ashleigh King with supervision from Ross Chapman.

We next examined SHLD1Δ function at telomeres lacking the end-protection afforded by shelterin[65], where 53BP1/shieldin/CST have been shown to counteract 5' end resection (Chapter 2, Figures 2.1-2.4)[35]. In *Tpp1*$^{F/F}$ MEFs, wt SHLD1 and SHLD1Δ were expressed at similar levels after Cre-mediated TPP1 deletion and/or bulk sgRNA targeting of SHLD1 (Figure 3.15A). We then performed a quantitative in-gel hybridization assay for changes in the relative amount of ss telomeric DNA in clonal *Tpp1*$^{F/F}$, *Shld1*$^{+/+}$ *or Shld1*$^{-/-}$ MEFs. TPP1-deletion increased 3' overhang signal, which

was further increased in the SHLD1-deficient clone (Figure 3.15B, C) as expected (Chapter 2; Figure 2.1[35]). As was the case for CSR, introduction of SHLD1Δ into *Tpp1*$^{F/F}$ *Shld1*$^{-/-}$ cells appeared to have the same effect as wt SHLD1, suppressing the increase of the 3' overhang signal to the same extent (Figure 3.15B, C). In multiple independent

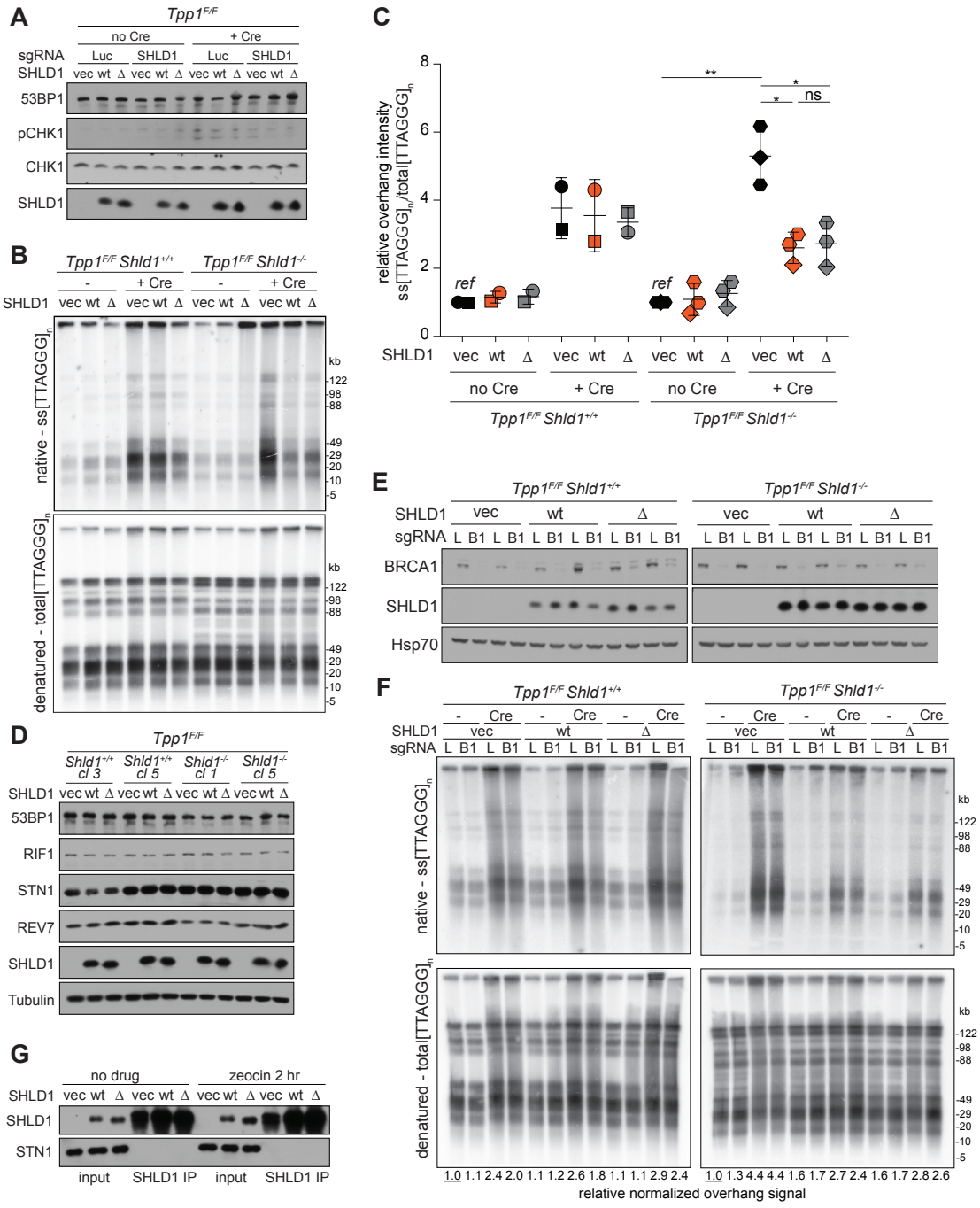

Figure 3.15. SHLD1Δ suppresses overhang increase at TPP1-deficient telomeres. A, Immunoblot showing CHK1 activation after *Tpp1* deletion and SHLD1 construct expression in the indicated cells. **B,** Quantitative analysis of telomeric ss overhang intensity using in-gel hybridization to detect the 3' overhang followed by rehybridization to the denatured DNA in the same gel, allowing the ratio of ss to total TTAGGG signal to be determined. **C,** Quantification of overhang intensity from cells as in **B** in two (*Shld1*$^{+/+}$) or three (*Shld1*$^{-/-}$) independent experiments using two independent clones for each genotype (represented by circle and square, diamond and hexagon symbols). Note different lane order in **A** versus **B** and **C**. **D,** Immunoblot showing expression of 53BP1 pathway components and SHLD1 construct expression in *Tpp1*$^{F/F}$ *Shld1*$^{+/+}$ *or Shld1*$^{-/-}$ clones. **E,** Immunoblot showing bulk CRISPR KO of BRCA1 and SHLD1 construct expression in cells of the indicated genotype with SHLD1 construct expression. **F,** Quantitative analysis of telomeric ss overhang intensity in cells as in **B** using in-gel hybridization to detect the 3' overhang followed by rehybridization to the denatured DNA in the same gel, allowing the ratio of ss to total TTAGGG signal to be determined. **G,** Immunoprecipitation of SHLD1 in *Tpp1*$^{F/F}$ MEFs with the indicated treatments and STN1 immunoblot. Statistical analysis was performed using ratio-paired t-test. *, $p<0.05$; **, $p<0.01$; ns, not significant. All means are indicated with center bars and SDs with error bars. Telomeric overhang assays were performed with help from Nanda Sasi.

clones, SHLD1Δ was expressed at the same level as wt SHLD1 and did not affect the expression of other proteins relevant to 53BP1 function (Figure 3.15D). We tested whether the SHLD1 LDLP motif has a function that is particular to the BRCA1-deficient context by CRISPR targeting *Brca1* in *Tpp1*$^{F/F}$ *Shld1*$^{-/-}$ MEFs and complementing them with wt SHLD1 or SHLD1Δ. However, deletion of BRCA1 did not alter the ability of SHLD1Δ to behave like wt SHLD1 in TPP1-deficient MEFs (Figure 3.15E, F). As was the case for the B cells used for CSR, we were unable to verify that the shieldin-CST interaction was diminished in MEFs expressing SHLD1Δ (Figure 3.15G).

We tested the possibility that ATM signaling (as presumably elicited by DSBs in PARPi-treated BRCA1-deficient cells) affects the shieldin-CST interaction. Deletion of TPP1 results in activation of ATR signaling, whereas ATM signaling is activated at telomeres when the shelterin subunit TRF2 is deleted[65]. At telomeres lacking TRF2, 53BP1 and REV7 repress the formation of excessive ss 3' telomeric DNA, although the

phenotype is not as strong as when TPP1 is absent (Chapter 2; Figures 2.1, 2.4)[30,35]. Therefore, we used a clonal *Trf2*$^{F/F}$ *Shld1*$^{-/-}$ MEF line to compare the effect of SHLD1Δ and wt SHLD1 on the formation of excessive ss telomeric DNA. The MEFs also lacked LIG4, thereby avoiding the confounding effect of telomere fusion after TRF2 deletion. In

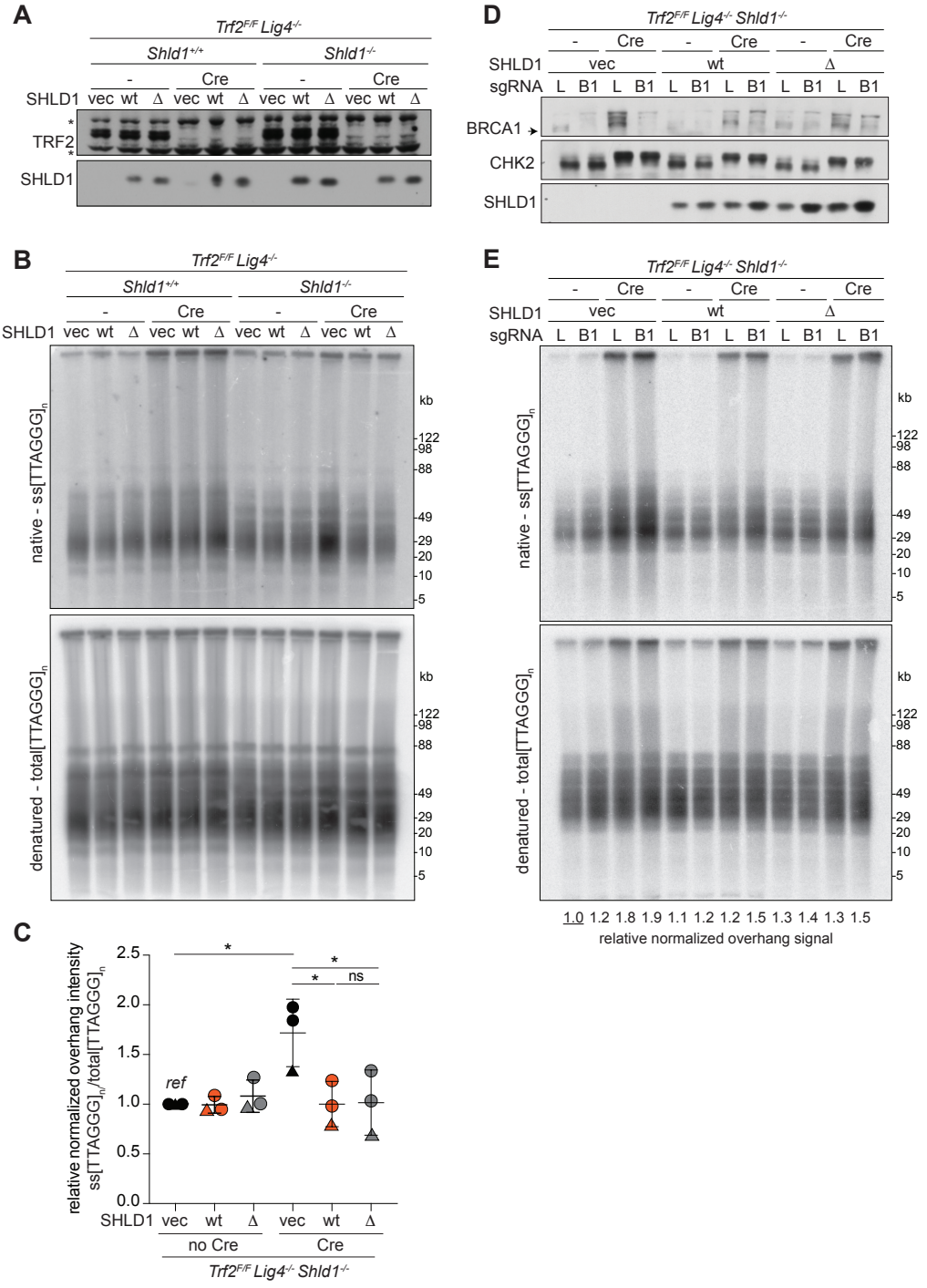

Figure 3.16. SHLD1Δ suppresses overhang increase at TRF2-deficient telomeres. A, Immunoblot showing SHLD1 construct expression and TRF2 loss after Cre in *Trf2$^{F/F}$ Lig4$^{-/-}$ Shld1$^{+/+}$* or *Shld1$^{-/-}$* clones. Asterisks indicate non-specific bands. **B,** Quantitative analysis of telomeric ss overhang intensity in cells as in **A. C**, Quantification of overhangs from *Trf2$^{F/F}$ Lig4$^{-/-}$ Shld1$^{-/-}$* cells in three independent experiments using two independent clones (circles and triangle). **D,** Immunoblot showing bulk CRISPR KO of BRCA1 (arrow), phosphorylation of CHK2 after TRF2 deletion, and SHLD1 construct expression. **E,** Telomeric overhang analysis on cells as in **D**. Statistical analysis was performed using ratio-paired t-test. *, $p<0.05$; **, $p<0.01$; ns, not significant. All means are indicated with center bars and SDs with error bars. Telomeric overhang assays were performed with help from Nanda Sasi.

this context as well, SHLD1Δ repressed the 3' telomeric overhang phenotype comparably to wt SHLD1 (Figure 3.16A-C). This finding held even when BRCA1 was co-deleted from the cells (Figure 3.16D, E). Thus, the SHLD1Δ mutant behaves differently in the context of dysfunctional telomeres and CSR than at the random DSBs in the BRCA1-deficient cells studied above. A possible reason for this distinction is discussed below.

3.7 Discussion

Determining how the RIF1/shieldin axis of 53BP1 prevents long 3' overhangs in DSB repair has been a subject of intensive research, and recently two (non-mutually-exclusive) models arose—that 5' end resection is blocked, or that resection is counteracted by fill-in synthesis. The data presented here provide direct evidence for the fill-in reaction in BRCA1-proficient and BRCA1-deficient cells in the form of incorporation of nucleotides at nuclease- or PARPi-induced DSBs in a 53BP1/shieldin/CST/Polα/primase-dependent manner (Figures 3.3-3.6). Two recent reports were published in support of the idea that fill-in synthesis is a general phenomenon at DSBs. A broad role for Polα-mediated fill-in at genome-wide DSBs was

noted at CRISPR/Cas9-induced DSBs[150] and at DSBs induced by ASISI[158]. These results are in keeping with our finding of CST/Polα/primase-dependent fill-in at FOKI-induced DSBs and further highlight the critical role of this mode of DSB processing. The implications of fill-in synthesis in DSB repair outside of the BRCA1-deficient context is discussed in Chapter 5.

We also highlight the critical role of fill-in synthesis in BRCA1-deficient cells. In this setting, we show the involvement of primase in promoting radial chromosomes (Figure 3.2); the ability of DSB-tethered CST to bypass the need for 53BP1/shieldin (Figure 3.10); and, based on a SHLD1 mutant (SHLD1Δ) that lacks CST binding, the requirement of CST recruitment for the function of shieldin in suppressing RAD51 loading and promoting radial formation (Figure 3.13). These hallmarks of shieldin loss in BRCA1-deficient cells were reversed when CST was force-tethered to shieldin containing SHLD1Δ by chemical-induced dimerization. Collectively, the data argue that 53BP1/shieldin function in BRCA1-deficient cells requires the interaction of shieldin with CST.

CST has been implicated both in CSR and at dysfunctional telomeres[35,90], two systems that have been used extensively as surrogates for DSB processing. Our previous work showed that shieldin recruits CST to dysfunctional telomeres, and that shieldin and CST are epistatic in their control of excessive 3' ss telomeric DNA (Figures 2.1-2.5)[35]. Yet, the SHLD1Δ mutant that does not bind CTC1 was fully functional in promoting CSR and preventing excessive ss 3' overhangs at dysfunctional telomeres. The difference in function of SHLD1Δ at random DSBs in BRCA1-deficient cells and at

DNA ends in CSR and at dysfunctional telomeres was not due to the presence of BRCA1 in the cells nor was it related to the activation of ATM versus ATR signaling.

What might account for the discordant behavior of SHLD1Δ? It is possible that SHLD1Δ behaves differently in CSR and at dysfunctional telomeres versus random DSBs due to a difference in cell-cycle phase of repair events, cell type (B cells for CSR), or chromatin context. However, we favor the explanation that SHLD1Δ is less deleterious to CST recruitment at DNA ends that bear CST recognition sites. The preferred substrates of CST are tandem repeats containing runs of 3 or more G residues (e.g. TTAGGG), but it also binds ssDNA containing multiple copies of GG dinucleotides[145]. The DNA ends formed during CSR have many tandem G-rich repeats[175] and the TTAGGG repeats of telomeres represent the optimal CST binding site. In particular, the mouse IgA switch region studied here contains more than 60 copies of tandem five nucleotide repeats containing GG or GGG (data not shown) and it is likely that these repeats can be bound by CST. The presence of these CST binding sites, together with the additional interactions between STN1 and TEN1 in CST and SHLD2, SHLD3, and REV7 in shieldin[35] (Chapter 2; Figure 2.5, 2.6) may make up for the lack of CTC1-SHLD1 interaction in the context of SHLD1Δ. In contrast, repeated runs of G residues will be less frequent at many of the random DNA ends created by IR or PARP inhibition, diminishing the CST-DNA interaction and making CST more reliant on its binding to SHLD1. We therefore propose that the behavior of SHLD1Δ in CSR and at dysfunctional telomeres represents an exception rather than the norm.

The idea that shieldin is important to facilitate the association of CST with DNA ends that lack preferred CST binding sites is consistent with the results of our bypass

experiments in which tethering of FHA-STN1 to DSBs did not fully complement the loss of SHLD2 (Figure 3.10B). Although this finding could be due to suboptimal function and/or recruitment of FHA fusion proteins, it is also possible that the shieldin-CST interaction improves the binding of CST to A-T rich overhangs, perhaps allowing CST to compete with RPA despite its lower affinity[145]. The *in vitro* binding affinity of SHLD2-C/SHLD1 (10 nM) is low compared to RPA[91], but the binding affinity of a complex formed by shieldin and CST (while undetermined) is likely to be much higher. It will be of interest to study the biochemistry and structural biology of CST/Polα/primase in complex with shieldin bound to ssDNA with and without repeated runs of G-residues. We have previously suggested that shieldin might function analogously to shelterin, which uses its TPP1 and POT1 subunits to recruit CST to fully protected telomeres[65]. A comparison of CST in complex with shieldin and with TPP1/POT1 would therefore be particularly informative. Finally, mutations in CST are responsible for the rare developmental disorder Coats plus[176] and the impact of these mutations on DSB repair warrants analysis. We[136] (Chapter 1) and others[156] have raised the possibility that 53BP1 acts primarily to ensure the fidelity of DSB repair. If so, the major outcome of inherited mutations that affect how shieldin and CST cooperate at DSB repair could be an increase in mutagenic repair and perhaps an associated increase in cancer risk.

CHAPTER 4. Expression of BRCA1, BRCA2, RAD51, and other DSB repair factors is regulated by CRL4/DDB1/WDR70

4.1 Abstract

Double-strand break (DSB) repair relies on DNA damage response (DDR) factors including BRCA1, BRCA2, and RAD51, which promote homology-directed repair (HDR); 53BP1, which affects formation of single-stranded (ss) DNA at DSBs; and proteins that mediate classical non-homologous end-joining (cNHEJ). Here we describe a role for the CRL4/DDB1/WDR70 cullin ring ligase complex in controlling the expression of DDR factors. Auxin-mediated degradation of WDR70 led to reduced expression of BRCA1, BRCA2, RAD51, and other HDR proteins; 53BP1 and its downstream effectors RIF1/shieldin/CST/Polα/primase; and other DDR factors. In contrast, cNHEJ factors were generally unaffected. Consistent with its effect on DDR factors, WDR70 loss abrogated the localization of HDR factors at DSBs and elicited hallmarks of genomic instability, although 53BP1/RIF1 foci still formed. Mutation of the DDB1-binding WD40 (DWD) motif, CRISPR disruption of DDB1, or inhibition of cullins phenocopied loss of WDR70, indicating that the effects were due to a change in CRL4/DDB1/WDR70. Finally, using RNA-seq, we show that the effect of WDR70 degradation is likely due to an effect on transcription. The data indicate that CRL4/DDB1/WDR70 is critical for the normal transcription of a multitude of genes, including BRCA1, BRCA2, RAD51.

4.2 Introduction

DSB repair can be mediated by classical non-homologous end-joining (cNHEJ) or homology-directed repair (HDR). BRCA1 and 53BP1 have been proposed to govern the choice between cNHEJ and HDR[3]. In addition to these pathways, DSBs that have undergone resection can be acted on by aNHEJ [24] or SSA[177]. (For a more complete introduction of these pathways, see Chapter 1[136]).

At the end of Chapter 1, we developed a model where the 53BP1 pathway promotes high fidelity DSB repair. Since the downstream effectors of 53BP1, namely the shieldin and CST ssDNA-binding complexes, are proposed to act at substrates with 3' ssDNA overhangs, we speculated that persistence of shieldin/CST on the ssDNA may be an impediment to RAD51 loading on the overhang. CST/Polα/prim is likely to leave sufficient ssDNA at the 3' end for RAD51 loading and HDR yet fill-in by CST/Polα/prim interferes with HDR of DSBs in BRCA1-deficient cells. This conundrum led us to speculate that BRCA1 might have a role in removing the shielding/CST complex, thereby freeing the ssDNA for RAD51 loading. BRCA1 could perform this function directly, for example through its E3 ligase activity in conjunction with BARD1 [178,179] or by removing 53BP1 from sites of DNA damage[131] but it could also evict shieldin/CST through an as-yet unidentified downstream effector. Such an effector would localize to DSBs (perhaps in a BRCA1-dependent manner) and would recapitulate BRCA1 phenotypes including PARPi-induced radial formation and sensitivity, and failure to load RAD51 at DSBs. After reviewing the literature, we selected two candidate factors that met these criteria and thus were possible mediators

of this function: SMARCAD1—a chromatin remodeler which was shown to have some BRCA1-like phenotypes—and WDR70, which is described in depth below.

4.3 No effect of SMARCAD1 on RAD51 loading or PARPi-induced radial formation

SMARCAD1 is an evolutionarily conserved SWI/SNF-like chromatin remodeler[180] that contains CUE domains which mediate interactions with ubiquitin and other proteins[181,182]; an ATPase domain; and a helicase domain (Figure 4.1A). A previous

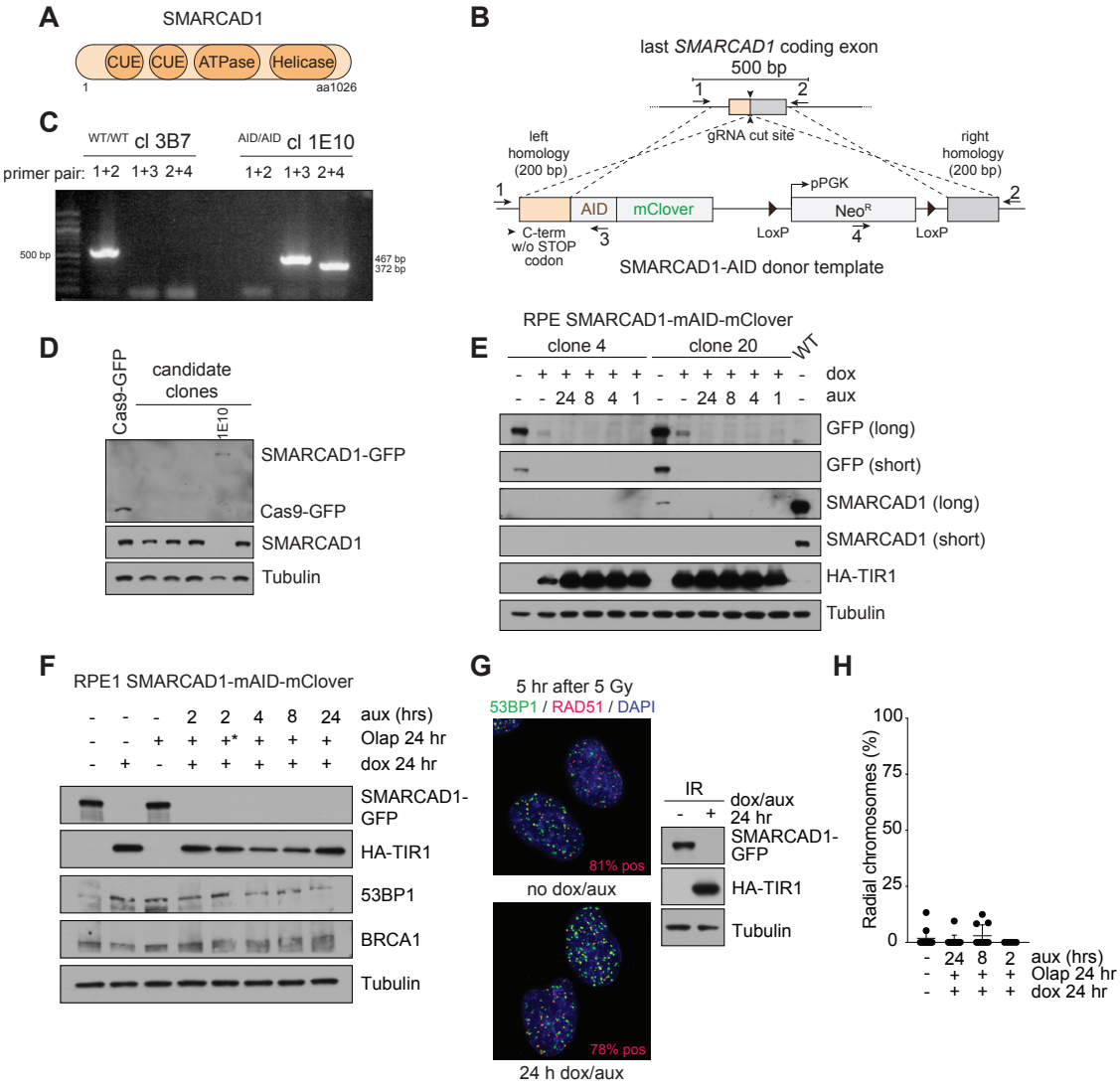

Figure 4.1. No effect of SMARCAD1 on RAD51 loading or PARPi-induced radial formation. A, Domain map of human SMARCAD1 protein, adapted from[79]. **B,** Generation of p53/Rb-null RPE1 cells[206] for rapid SMARCAD1 degradation. Top, Schematic for insertion of mAID-mClover cassette into both RPE1 *SMARCAD1* alleles. Bottom, diagnostic PCR showing bands of expected sizes for wild-type clone 3B7 (500 bp) and homozygous knock-in clone 1E10 (no wild-type band; left band 467 bp; right band 372 bp). Clone 1E10 was used in subsequent experiments. **C**, Immunoblot for GFP to detect mClover and SMARCAD1 on several candidate SMARCAD1-mAID-mClover clones. RPE1 cells expressing Cas9-GFP were run as a positive control for the GFP blot. Clone 1E10 is indicated; the other clones were not successfully edited. **D**, Immunoblot showing two SMARCAD1-mAID-mClover subclones of 1E10 isolated after introduction of HA-OsTIR1. Clone 20 was selected for further experiments. **E**, Immunoblot for SMARCAD1-mAID-mClover cells with the indicated treatments. Asterisk: In this lane, cells were also treated with Polα inhibitor CD437 for 2 h. **F**, Representative IF detecting 53BP1 and RAD51 foci formation in the indicated irradiated cells. The percent of cells with > 10 RAD51 foci is indicated in red on the images. Right, immunoblot verifying SMARCAD1 degradation. **G**, Quantification of radial chromosome formation in a subset of cells as in **E**. All panels are representative of one experiment.

study found that SMARCAD1 loss resembled BRCA1 deficiency in several key aspects: sensitivity to PARPi which was reversed by 53BP1 loss; lack of RAD51 loading which was also rescued by 53BP1 loss; and globular 53BP1 foci formation rather than the characteristic circular or horseshoe shaped foci[179]. SMARCAD1 was therefore a potential candidate for the BRCA1-mediated removal of shieldin/CST that we speculated about. In an attempt to reproduce the published data on SMARCAD1 deficiency, we first generated human RPE1 cells where SMARCAD1 can be rapidly depleted using the auxin/TIR system[168] (Figure 4.1B). Biallelic knock-in of the mini-AID cassette into the *SMARCAD1* locus was verified by PCR and immunoblotting (Figure 4.1C, D). Dox/aux-inducible SMARCAD1 degradation was seen in independent subclones harboring dox-inducible TIR1 (Figure 4.1E). Despite efficient SMARCAD1 degradation—which had no effect on 53BP1 or BRCA1 levels (Figure 4.1F)—IR-induced RAD51 foci formation was unaffected by SMARCAD1 loss (Figure 4.1G).

Concordantly, no radial chromosome formation was detected in SMARCAD1-deficient cells treated with PARPi (Figure 4.1H). Thus, in RPE1 cells, SMARCAD1 deficiency did not recapitulate the hallmarks of BRCA1 loss and was therefore not investigated further as a candidate factor for BRCA1-mediated removal of shieldin/CST.

4.4 WDR70 introduction

A second candidate for BRCA1-mediated removal of shieldin/CST at DSBs was WDR70. WDR70 is thought to function as part of the DDB1/Cullin Ring Ligase 4 (CRL4) complex[183]. CRL complexes are modular ubiquitin ligases with diverse roles in mammalian cell biology, including in DNA repair[184,185]. They are composed of a scaffold (cullin family protein), a RING finger protein (e.g., Rbx1), a linker protein (e.g. DDB1), and one of many substrate specificity factors (e.g. WDR70)[184]. Recent data suggests that CRL4/DDB1/WDR70 plays a role in the DDR. In fission yeast, WDR70 promotes resection through histone H2B mono-ubiquitination by opposing Crb2^{53BP1}[183]. Human WDR70 has also been linked to resection and HDR[183,186], making it an appealing target for further investigation. Intriguingly, DDB1 was identified in an siRNA screen for genes whose loss—like BRCA1/2—sensitizes cells to PARPi[187], further hinting at a role in HDR.

Because WDR70 appears to be essential in human cells (https://depmap.org/portal) and other organisms[188], we created RPE1 cells in which the endogenous WDR70 can be degraded with an auxin-inducible degron (AID)[168]. Using this system, we confirm that WDR70 is essential for cell viability and report that acute loss of WDR70 triggers genome instability. While WDR70 localizes to DSBs, its

localization did not depend on BRCA1, arguing against a role for WDR70 as a downstream effector of BRCA1 that evicts shieldin/CST complexes. Instead, we noted that WDR70 loss precipitated a striking reduction in the expression levels of BRCA1, BRCA2, RAD51 and other proteins involved in HDR and abrogation of DSB-induced focus formation by these factors. 53BP1 and its downstream factors, as well as proteins involved in aNHEJ, were also reduced after WDR70 loss. In contrast, factors involved in cNHEJ and apical DDR factors, such as the ATM kinase and RNF8, were unaffected. Based on mutations in WDR70, depletion of DDB1, and chemical inhibition of cullin activity, we conclude that WDR70 acts as part of the CRL4/DDB1 complex. These data reveal a novel shared regulation of factors involved in specific DSB repair pathways by the CRL4/DDB1/WDR70 complex.

4.5 WDR70 localizes to DSBs in a BRCA1-independent manner

We initially suspected that WDR70 might act downstream of the initial end processing steps promoted by BRCA1[12], potentially to evict shieldin/CST from 3' overhangs. We therefore asked whether WDR70 can localize to DNA damage foci, and whether this localization depends on BRCA1. WDR70 localized to DSBs induced by FOKI in U2OS-LacO cells expressing an inducible mCherry-tagged LacI-FOKI fusion protein[169] (Figure 4.2A). This experimental system facilitates the detection of factors localizing to DSBs, presumably because numerous DSBs are induced in the LacO array. After induction, most cells showed colocalization of the mCherry (FOKI) signal with WDR70 signal (Figure 4.2A). However, CRISPR-mediated knock out of BRCA1 did not diminish WDR70 recruitment to FOKI-induced DSBs (Figure 4.2B, C).

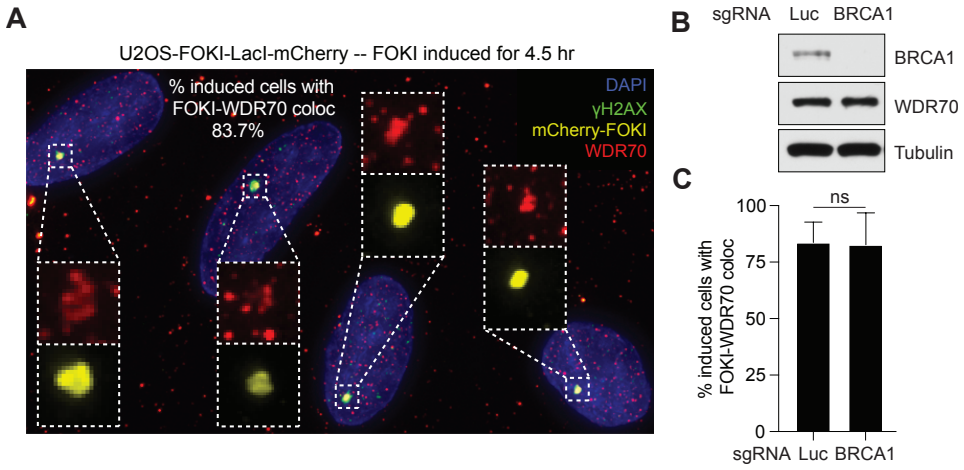

Figure 4.2. WDR70 localizes to DSBs in a BRCA1-independent manner. A, Representative IF image of U2OS-FOKI-LacI-mCherry cells where FOKI cutting is induced by treatment with tamoxifen (4-OHT) and the Shield-1 ligand. Cells were subjected to IF for γH2AX (green, Alexa-488) and WDR70 (red, Alexa-647) and counterstained with DAPI. mCherry fluorescence is false-colored yellow. **B**, Immunoblot on U2OS FOKI-LacI-mCherry cells with the indicated bulk targeting using CRISPR/Cas9 and sgRNAs to luciferase (*Luc*, control) or *BRCA1*. **C**, Quantification of the percent of FOKI-induced cells showing WDR70 colocalizing with mCherry-FOKI signal. Data from five independent experiments with mean and SD indicated. Statistical analysis based on two-tailed Welch's t-test. ns, not significant.

4.6 WDR70 is essential for genome integrity

To examine the phenotype of WDR70 loss, we generated cells in which endogenous WDR70 (Figure 4.3A) can be degraded rapidly using the AID/TIR1 system[168]. CRISPR/Cas9 was used to achieve biallelic knock-in of mini AID (mAID) fused to mClover into the *WDR70* loci of p53/RB-null RPE1 cells (Figure 4.3B). Biallelic targeting

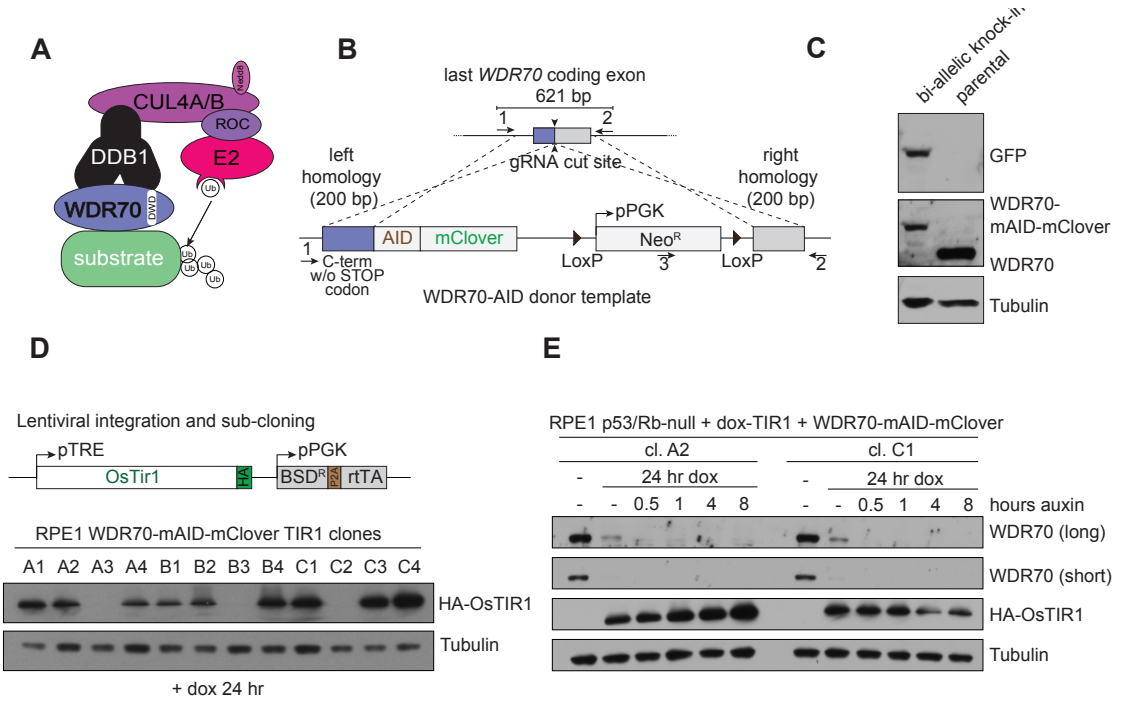

Figure 4.3. Generation of RPE1 cells for rapid WDR70 degradation. A, Schematic representation of CRL4/DDB1 complex shown with WDR70 (one of many potential adapter proteins). This complex is thought to promote ubiquitin-mediated degradation of substrate proteins. Adapted from[184]. **B**, Schematic for insertion of mAID-mClover cassette into both *WDR70* alleles of of p53/Rb-null RPE1 cells[206]. **C**, Immunoblot for GFP and WDR70 showing a representative WDR70-mAID-mClover candidate clone and the parental cell line for comparison. **D**, Immunoblot for HA-tagged OsTIR1 after doxycycline induction in 12 candidate subclones of clone 2E9, which had successful biallelic m-AID knock-in as in **C**. Subclones A2 and C1 were selected for further study. **E**, Immunoblot for dox/auxin-mediated degradation of WDR70 in two clones. Clone A2 was used for the experiments below and is referred to as WDR70-degron cells.

was confirmed by western blot (Figure 4.3C). Subclones harboring lentiviral dox-inducible HA-tagged OsTIR1 were generated (Figure 4.3D) such that dox and auxin (aux) addition in two independent clones resulted in rapid loss of WDR70 protein (Figure 4.3E).

We used one of these clones to examine the effects of WDR70 loss in RPE1 cells. WDR70-deficient cells experienced impaired cell cycle progression and reduced BrdU incorporation as judged by flow cytometry (Figure 4.4A, B), and ultimately death

with prolonged dox/auxin treatment (Figure 4.4C). Furthermore, DAPI-stained nuclei showed increased frequency of micronucleation, gross nuclear abnormalities, and elevated levels of γH2AX foci formation, all hallmarks of genomic instability (Figure 4.4D-G). These data indicate that WDR70 is an essential factor required for normal cell cycle progression and maintenance of genome integrity.

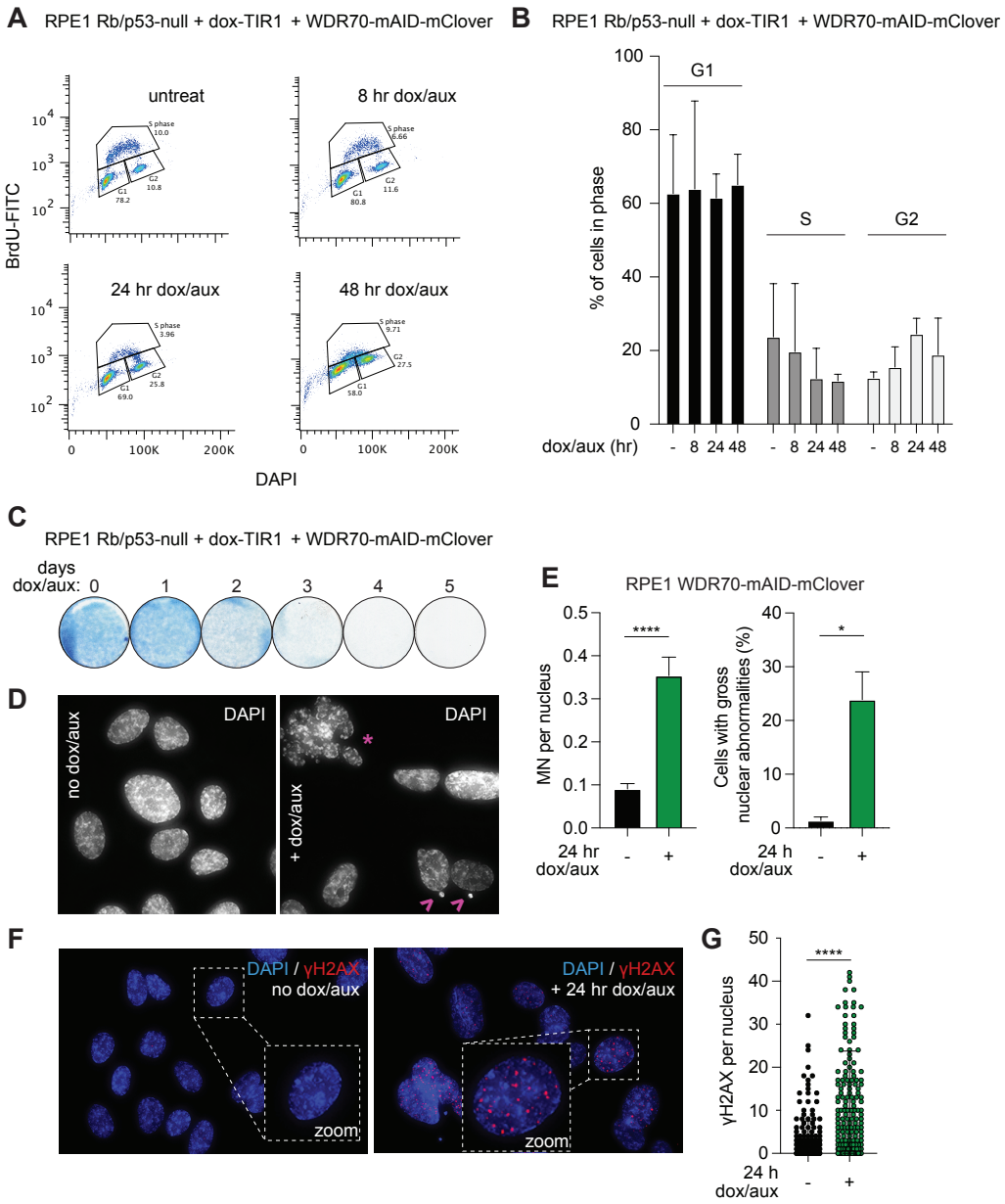

Figure 4.4. WDR70 is essential for genome integrity. A, Cell cycle flow cytometry plots for BrdU incorporation (30 m pulse of BrdU before fixation) and DAPI content in WDR70-degron cells with dox/auxin treatment for the indicated time. **B**, Quantification of cell cycle phase based on data as represented in **A**. **C**, Survival assay for cells in which WDR70 is degraded. Cells in 6-well plates were treated with dox/auxin for the indicated number of days and then analyzed by methylene blue staining at day 5. **D**, Representative images of DAPI-stained nuclei in control cells or WDR70-degron cells treated with dox/auxin for 24 hours. Micronuclei (MN) are indicated by the arrowhead; grossly abnormal nuclear morphology is indicated by the asterisk. **E**, Quantification of MN formation and grossly abnormal nuclei induced by WDR70 degradation detected as in **D**. **F**, Representative IF for γH2AX foci in control cells or WDR70-degron cells treated with dox/auxin for 24 hr. **G**, Quantification γH2AX foci as in **F**. Each dot represents a nucleus. For all panels, data is from three independent experiments. All statistical analysis based on two-tailed Welch's t-test. *, $p<0.05$; **, $p<0.01$; ***, $p<0.001$; ****, $p<0.0001$; ns, not significant. All means are indicated with center bars and SDs with error bars.

4.7 WDR70 regulates DNA damage response factors

In cells deprived of WDR70, we examined by immunoblotting the status of BRCA1 and other HDR factors. Strikingly, degradation of WDR70 resulted in loss of BRCA1, BRCA2, BARD1, and RAD51 (Figure 4.5A-C). Loss of these HDR factors in WDR70-deficient cells was accompanied by loss of the BRCA- and HDR-relevant factors ABRAXAS, RAP80, and PALB2, and the nuclease EXO1 and helicase WRN[12] (Figure 4.5D). The loss of these factors was not apparent after 8 h dox/aux treatment when some WDR70 remained but became obvious at 24 h coinciding with WDR70 being undetectable (Figure 4.5A, D). We therefore continued with the longer treatment protocol in subsequent experiments. The effect of WDR70 loss was independent of DNA damage and not further exacerbated by treatment with PARPi (Olaparib) or ionizing radiation (IR) (Figure 4.5B, C). WDR70 protein levels were similar in asynchronous cells and in cells arrested in G2 by RO-3306, and WDR70 degradation

accompanied by BRCA1 loss was unaffected by arrest in G2 (Figure 4.5E), suggesting that the function of WDR70 described here is not regulated by DNA damage or the cell cycle.

In addition to the HDR factors, 53BP1 and its downstream effectors RIF1 and REV7 were strongly diminished after WDR70 degradation (Figure 4.5A, B, F). REV7 is a subunit of the shieldin complex along with SHLD1, SHLD2, and SHLD3[134]. SHLD1/2/3 proteins are weakly expressed, and validated antibodies are scarce, but we observed that WDR70 degradation also precipitated SHLD2 loss (Figure 4.5G). Furthermore, two

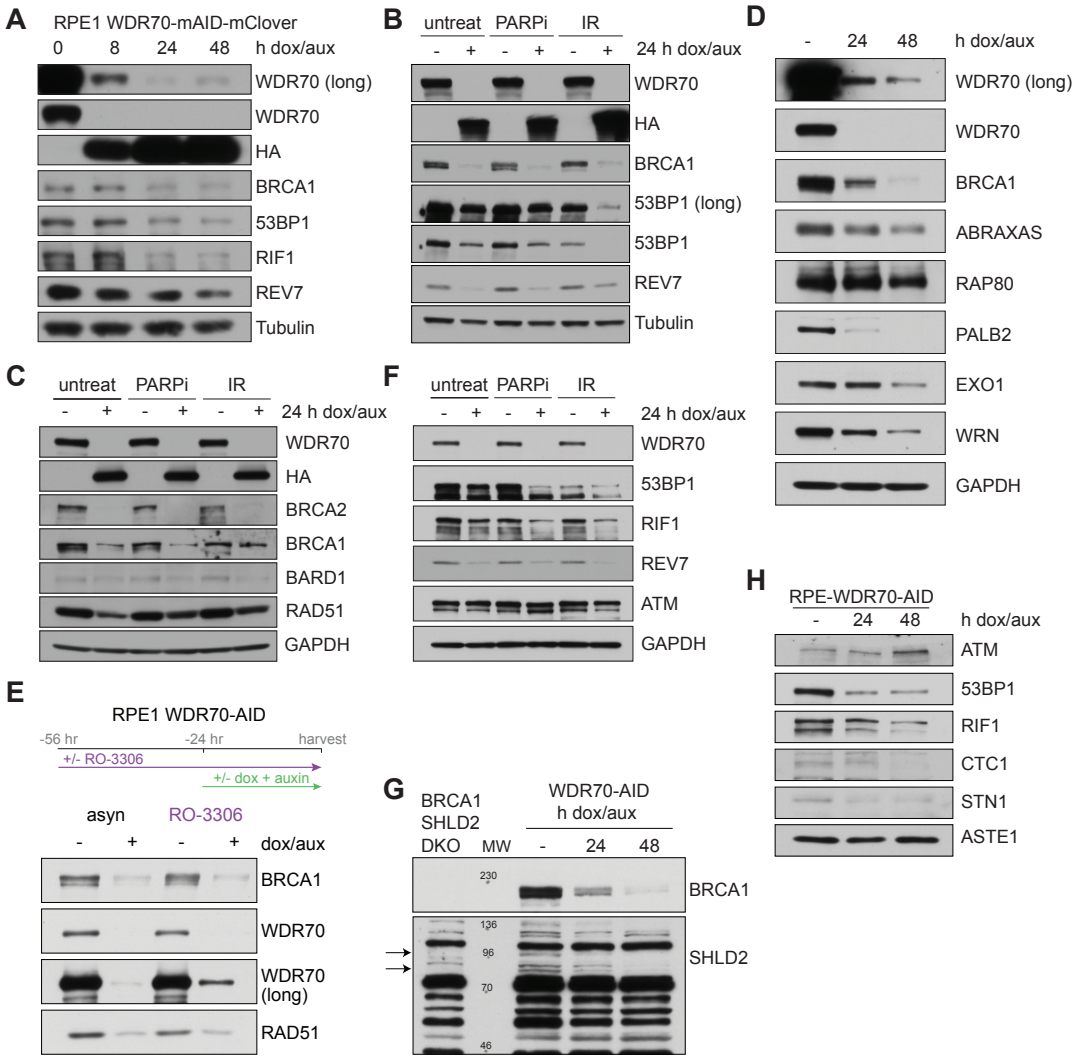

Figure 4.5. WDR70 regulates DNA damage response factors. A, Immunoblot for the indicated proteins in WDR70-degron cells after the dox/auxin treatment for the indicated times. **B**, Immunoblot for the indicated proteins in cells as in **A** treated with Olaparib (2 μM, 24 hr) or IR (5 hr after 5 Gy), with or without dox/auxin for 24 hr. **C,** Immunoblots for HDR factors and other BRCA-associated factors in WDR70-degron cells treated as in **B. D,** Immunoblots detecting HDR factors and other BRCA-associated factors in WDR70-degron cells treated for the indicated times with dox/aux. **E**, Top, time-line for cell cycle arrest and immunoblot analysis of WDR70-degron cells. Bottom, immunoblot for BRCA1, RAD51, and WDR70 in asynchronous cells and G2 arrested cells treated with dox/aux. **F-H,** Immunoblot analysis of 53BP1 pathway factors as in **B-D.** In **G**, *BRCA1/SHLD2* DKO RPE1 cells[91] were used to validate the SHLD2 antibody which results in many non-specific bands. Arrows indicate two bands that are absent in the *BRCA1/SHLD2* DKO RPE1 cells but present in WDR70-degron cells. These bands decrease after 24 or 48 hr dox/aux treatment. All blots are representative of two-four independent experiments. **D, F** were performed by Keshav Sharma. Because of the dramatic effect of WDR70 loss on DDR pathway components, protein concentrations were checked by BCA assay and Ponceau stains to ensure equal loading, and three distinct loading controls were employed (γTubulin, GAPDH, and HSP70), all of which were unchanged by WDR70 loss.

subunits of the CST complex, CTC1 and STN1, which acts downstream of 53BP1/shieldin to mediate fill-in synthesis at DSBs[35] (also see Chapters 2 and 3), were reduced in WDR70-deficient cells (Figure 4.5H); no antibody is available for the third CST subunit TEN1.

A number of proteins relevant to DSB repair were not affect by WDR70 degradation. ASTE1, a structure-specific endonuclease that localizes to DSBs downstream of shieldin and promotes NHEJ[143], was unaffected by WDR70 loss (Figure 4.5H) as were factors acting upstream of 53BP1 in the DDR signaling cascade (ATM, RNF8) (Figure 4.5H, Figure 4.6A). Some factors involved in aNHEJ (XRCC1 and Ligase 3) were also regulated by WDR70 while others (PARP1, POLQ) were not (Figure 4.6B, C). In contrast, none of the cNHEJ factors queried (KU70/80, DNA-PK, Artemis, LIG4) were affected by WDR70 loss (Figure 4.6D) and neither were the cohesin complex and

PCNA (Figure 4.6E). Collectively, the data reveal that WDR70 regulates the expression of DSB repair proteins in a manner that is selective to certain pathways. Specifically, the proteins that are affected by WDR70 create, regulate, or rely on DSB resection.

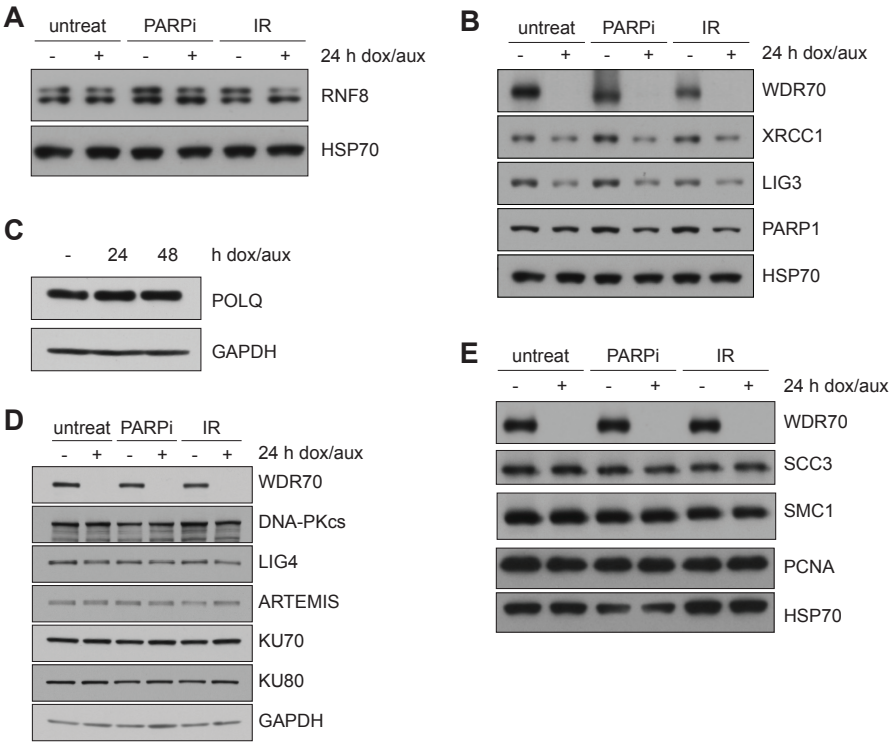

Figure 4.6. The effect of WDR70 on aNHEJ and cNHEJ factors. A, Immunoblot for RNF8 after treatment of WDR70-degron cells with dox/aux and either Olaparib (2 μM, 24 hr) or IR (5 hr after 5 Gy) as indicated. **B,** Immunoblot for the indicated aNHEJ proteins in cells as in **A**. **C,** Immunoblot for aNHEJ factor POLQ after treatment of WDR70-degron cells with dox/aux for one or two days. **D**, Immunoblot for the indicated cNHEJ factors in cells treated as in **A**. **E**, Immunoblot for cohesin subunits SCC3 and SMC1 and PCNA in cells treated as in **A**. All blots performed by Keshav Sharma and representative of multiple independent experiments. GAPDH or HSP70 are used as loading controls and are unaffected by WDR70 loss. Protein concentrations loaded on gels were ensured to be equal based on BCA Assay and Ponceau stain.

4.8 The effect of WDR70 loss on DNA damage foci

To determine whether WDR70 loss affects the ability of DDR factors to form DNA damage foci, we performed immunofluorescence (IF) after induction of DNA damage with PARPi or IR (Figure 4.7A, B). As shown above (Figure 4.4F, G), WDR70 loss itself

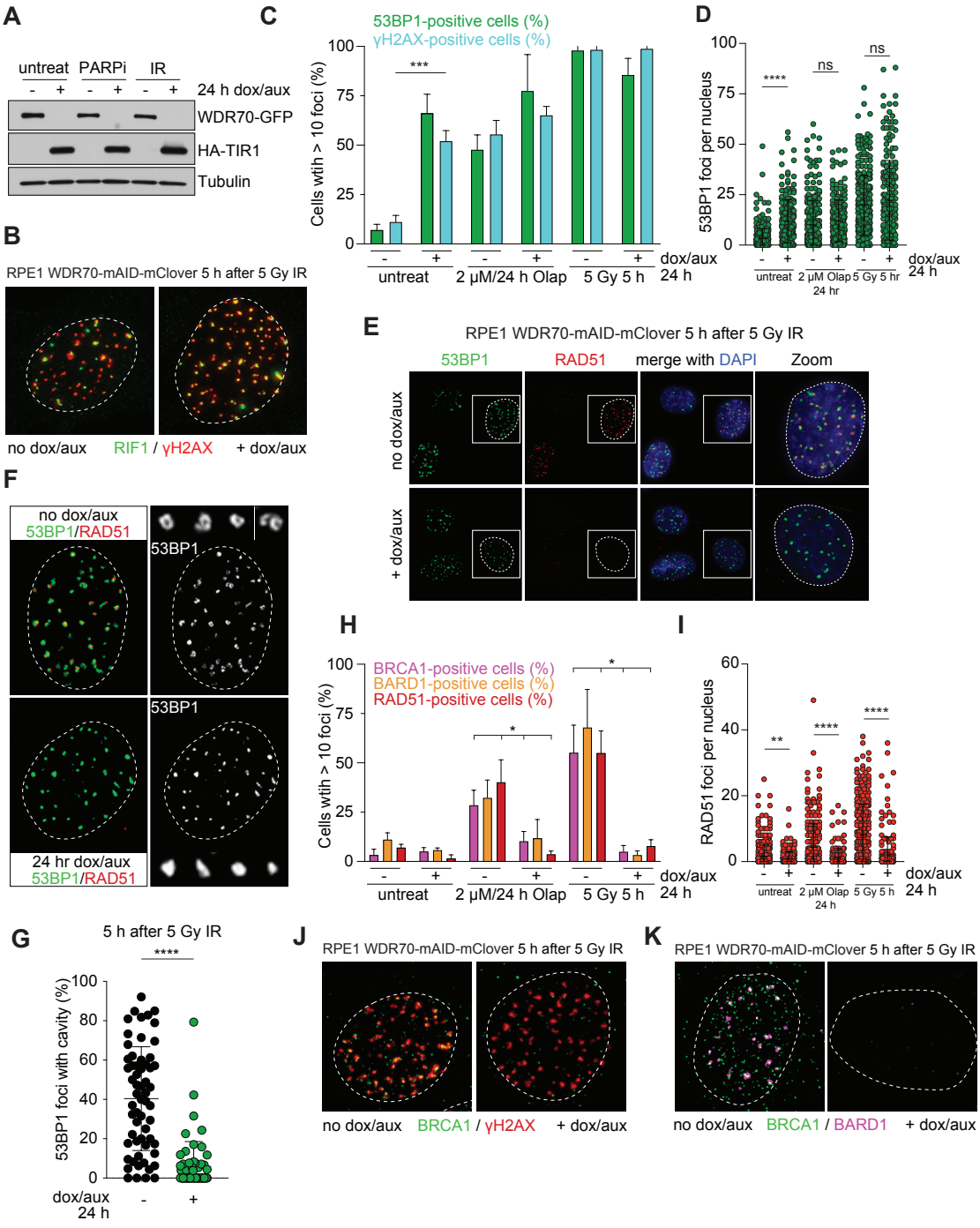

Figure 4.7. The effect of WDR70 loss on DNA damage foci. A, Immunoblot for WDR70 and HA-TIR in WDR70-degron cells untreated or treated with Olaparib (2 μM, 24 hr) or IR (5 hr after 5 Gy), with or without dox/auxin for 24 hr. **B**, Representative IF images of RIF1 (green) and γH2AX (red) in irradiated cells as in **A** with or without 24 hours of dox/auxin treatment. **C**, Quantification of percent of cells with greater than 10 foci in cells as in **A**. Bar graph depicts mean and SD from three independent experiments with 150-350 nuclei scored per condition. **D**, Automated foci scoring of 53BP1 foci per nucleus in WDR70-degron cells as in **C** with the indicated treatments. Each dot represents a nucleus. **E**, Representative IF images of 53BP1 (green) and RAD51 (red) co-stain in irradiated cells as in **A**. Dashed lines demarcate nuclear outline; solid white lines indicate the zoom panel merged with DAPI at right. **F**, Representative images from depicting 53BP1 and RAD51 foci architecture in the indicated irradiated cells. Right panel (53BP1) includes four enlarged foci from each nucleus. **G**, Quantification of the percent of 53BP1 foci with a cavity (see Materials and Methods for scoring rubric) in irradiated cells as in **F**. Each dot represents one nucleus. Data from three independent experiments with 60 nuclei scored per condition. **H**, Quantification of percent of cells with greater than 10 foci as in **C**. Bar graph depicts mean and SD from two (BARD1) or three (BRCA1, RAD51) independent experiments with 150-350 nuclei scored per condition. **I**, Automated foci scoring of RAD51 foci per nucleus in WDR70-degron cells as in **H** with the indicated treatments. Each dot represents a nucleus. **J**, Representative IF images of BRCA1 (green) and γH2AX (red) in cells as in **B**. **K**, Representative IF images of BRCA1 (green) and BARD1 (magenta) in cells as in **B.** Experiments were performed in collaboration with Keshav Sharma. All statistical analyses as in Figure 4.4.

induced γH2AX foci, even in the absence of DNA damage (Figure 4.7C). After PARPi- or IR-treatment of WDR70-deficient cells, the same level of γH2AX foci occurred as in WDR70-proficient cells, confirming that ATM and/or ATR signaling remained intact (Figure 4.7C).

We suspected that the ability of factors whose expression was affected by WDR70 loss would be compromised in their ability to form DNA damage foci. But interestingly, WDR70 loss did not diminish 53BP1 foci in response to DNA damage (Figure 4.7C-E), despite the dramatic loss of 53BP1 protein seen in immunoblots following irradiation (Figure 4.5B, F). RIF1 also retained its ability to form IR-induced foci even in the absence of WDR70 (Figure 4.7B). Though 53BP1 foci still formed in WDR70-deficient cells, the architecture of the foci was altered. 53BP1 forms ring- or

horseshoe-shaped microdomains that encircle BRCA1, RAD51, and RPA and this distinctive architecture is dependent on BRCA1[131,132]. Consistent with their reduced BRCA1 expression, WDR70-deficient cells had 53BP1 foci that did not show the horseshoe shape and were more globular (Figure 4.7F, G).

We next examined the ability of HDR factors to form DNA damage foci. In stark contrast to γH2AX and 53BP1/RIF1, the ability of BRCA1, BARD1, and RAD51 to form DNA damage foci was abrogated by WDR70 loss (Figure 4.7H-K). WDR70-deficient cells that did not experience PARPi or IR also showed a reduction in RAD51 foci, suggesting that the defect in RAD51 loading extends to endogenous DNA damage as well as PARPi or IR treatment (Figure 4.7I). As expected, the loss of BRCA1 and RAD51 foci correlated with the change in 53BP1 architecture noted above (Figure 4.7F, G). These results demonstrate that WDR70 specifically promotes the ability of HDR factors to coalesce into DSB foci.

4.9 WDR70 functions via its DWD motif as part of the CRL4/DDB1/WDR70 complex

WDR70 has been proposed to function as an adaptor to DDB1 as part of a Cullin Ring Ligase 4(CRL4) complex[183]. We therefore tested whether the DDB1-interacting WD motif (DWD) of WDR70[189] is important for its function by mutating the key tryptophan and aspartic acid residues to alanine (WD-AA mutant). The wild-type (wt) WDR70 was expressed slightly higher than the endogenous mAID-tagged WDR70, while the WD-AA mutant was expressed at similar levels to the endogenous WDR70 (Figure 4.8A). Importantly, the loss of BRCA1 and RAD51 in WDR70-deficient cells was mitigated by

wt WDR70 but not the WD-AA mutant (Figure 4.8A), indicating a functional role for these residues. The REV7 component of shieldin showed the same trend (Figure 4.8A).

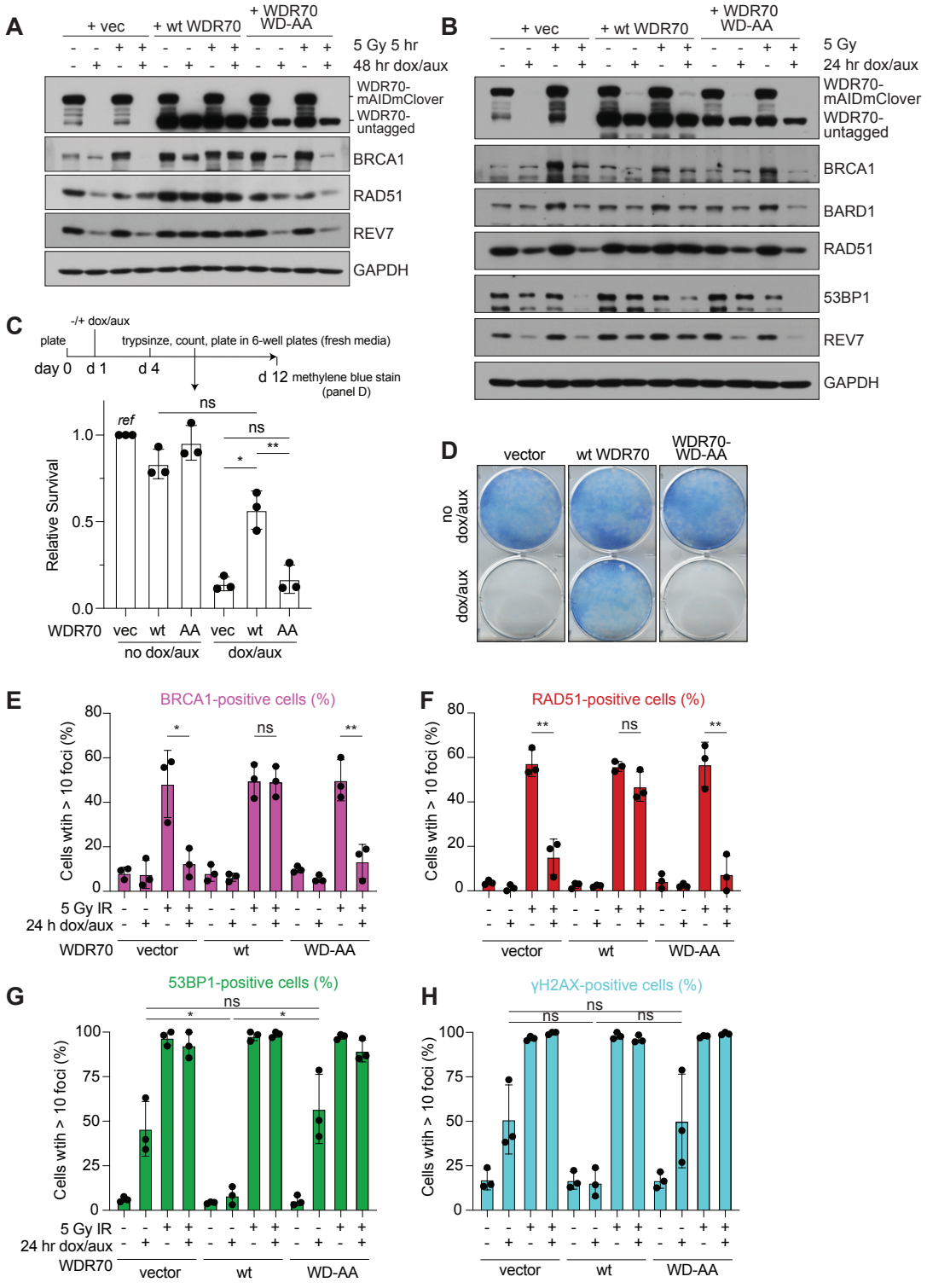

Figure 4.8. WDR70 function requires its DWD motif. A, Immunoblots for the indicated proteins from WDR70-degron cells complemented with empty vector (vec) or the indicated WDR70 constructs. Indicated cells were treated with IR (5 hr after 5 Gy) and/or dox/auxin for 48 hr. The top blot is WDR70 antibody, which detects the knock-in mAID-mClover-tagged WDR70 and the exogenously expressed untagged WDR70 wild-type or WD-AA mutant. **B**, Immunoblots for the indicated proteins from WDR70-degron cells as in **A** but with dox/auxin for 24 hr. **C**, Experimental schematic of cell survival assay for WDR70-degron cells complemented with empty vector or the indicated WDR70 constructs. Bottom, relative survival of the indicated cells after 72 hr of dox/aux treatment, normalized to empty vector cells with no dox/aux (ref). **D**, WDR70-degron cells complemented with empty vector or the indicated WDR70 constructs were stained with methylene blue to assess outgrowth after the indicated treatments. Experimental schematic in **C**. **E-H**, Quantification of percent of cells with greater than 10 foci in the indicated cells. Bar graph depicts mean and SD from three independent experiments with 200-400 nuclei scored per condition. All statistical analyses as in Figure 4.4.

The WDR70-dependent effects on protein levels were observed at 24 h of dox/auxin treatment (Figure 4.8B) but were more pronounced at 48 h (Figure 4.8A). The cell death elicited by WDR70 loss was reversed by wt WDR70 but not the WD-AA mutant (Figure 4.8C, D). Additionally, the failure of WDR70-deficient cells to form BRCA1 and RAD51 foci was fully complemented by wt WDR70 but not the WDR70 WD-AA mutant (Figure 4.8E, F). The 53BP1 and γH2AX foci observed in WDR70-deficient cells without DNA damaging agents were also suppressed by wt WDR70 but not the WD-AA mutant (Figure 4.9G, H).

These data prompted us to investigate whether HDR factor protein levels depend on the CRL4/DDB1/WDR70 complex. Consistent with that possibility, a pan-cullin inhibitor MLN4924[190] resulted in the progressive loss of BRCA1, BARD1, 53BP1, and REV7 (Figure 4.9A, B). Overexpression of wt WDR70 did not reverse the effect of MLN4924, although it again rescued the protein loss phenotypes associated with WDR70 degradation (Figure 4.9A). We used bulk CRISPR KO with two sgRNAs to

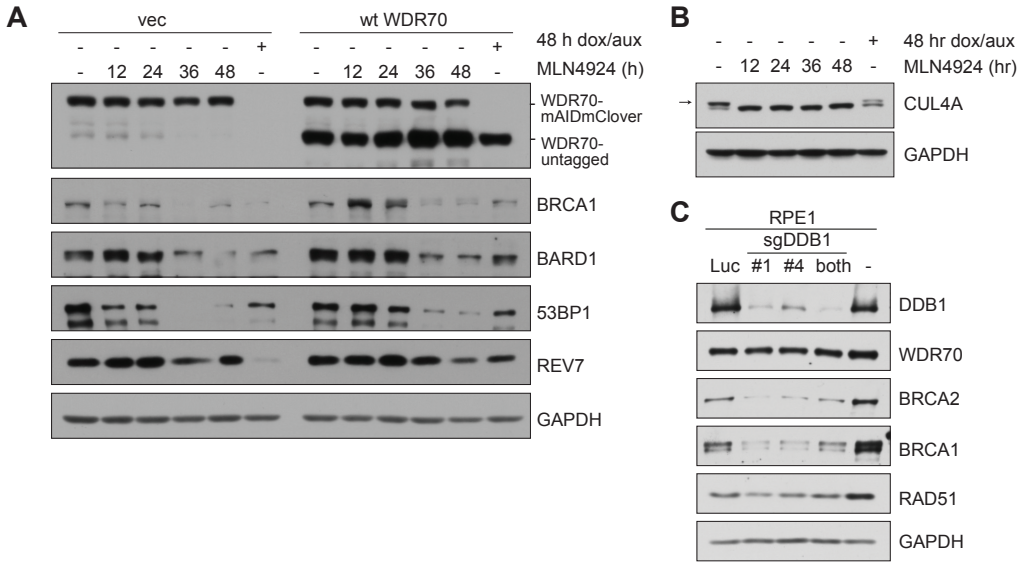

Figure 4.9. WDR70 functions as part of the CRL4/DDB1/WDR70 complex. A, Immunoblots for the indicated proteins from WDR70-degron cells complemented with empty vector or wild-type WDR70. Cells were treated with the pan-cullin inhibitor MLN4924 for the indicated time, or 48 hr of dox/auxin treatment. **B**, Immunoblot for CUL4A after treatment with MLN4924. Treatment with MLN4924 results in the disappearance of the top band, which likely represents NEDD8-conjugated CUL4A. **C**, Immunoblots for the indicated proteins from RPE1 cells treated with bulk CRISPR KO targeting luciferase (Luc) or *DDB1*. Experiments were performed by Keshav Sharma.

disrupt the CUL4 linker DDB1[184,187,189]. DDB1 KO with both sgRNAs together or individually reduced the levels of BRCA2, BRCA1, and RAD51 (Figure 4.9C) in a manner that is reminiscent of the effect of WDR70 loss (Figure 4.5), though WDR70 levels were not affected by targeting DDB1 (Figure 4.9C). Taken together, these results suggest that the expression of DDR factors promoted by WDR70 occurs in the context of a CRL4/DDB1/WDR70 complex.

4.10 WDR70 loss affects transcript levels of HDR and other DDR factors

We performed bulk RNA sequencing in WDR70-degron cells to test whether the loss of DDR proteins was due to a decrease in the mRNA levels of the corresponding genes. Total RNA was extracted from WDR70-depleted cells for comparison to control cells. Many factors were differentially regulated between cells with and without WDR70 (Figure 4.10A), but reassuringly, BRCA1 and RAD51 emerged as two of the most significantly down-regulated genes in WDR70-depleted cells (Figure 4.10A). Transcripts of the HDR factors BRCA2, BRIP1 (or BACH1/FANCJ), RAD51D, RAD54L, and others were also significantly diminished in WDR70-depleted cells (Figure 4.10A). PALB2, EXO1, and WRN, which were decreased in WDR70-depleted cells at the protein level (Figure 4.5D) were slightly elevated by RNAseq (Figure 4.10A). We confirmed the decrease seen in BRCA1, BRCA2, and RAD51 mRNA seen by RNAseq using RT-PCR (Figure 4.10B, E). BARD1 showed mildly increased mRNA levels in WDR70-depleted cells (Figure 4.10A, B), though BARD1 protein was slightly decreased in cells lacking WDR70 (Figure 4.5C), perhaps because of the more dramatic loss of its obligate binding partner, BRCA1 (Figure 4.10A; Figure 4.5C).

RNA sequencing of WDR70-depleted cells also revealed a decrease in transcripts of 53BP1, RIF1, MAD2L2 (REV7), and the CST complex (Figure 4.10C), in agreement with the loss of these proteins upon WDR70 degradation (Figure 4.5A, B, F-H). Upstream DDR signaling factors including ATM, MDC1, and γH2AX were modestly changed or unchanged, while RNF8 and RNF168 showed an increase (Figure 4.10C). We validated the change in mRNA levels for 53BP1, MAD2L2, and STN1 by RT-PCR (Figure 4.10D, E). cNHEJ factors which were unchanged at the protein level in WDR70-

depleted cells were mildly affected by WDR70 loss in the RNAseq data set (LIG4, PRKDC (DNA-PK), DCLRE1C (Artemis), and NHEJ1 (XLF)) (Figure 4.10F).

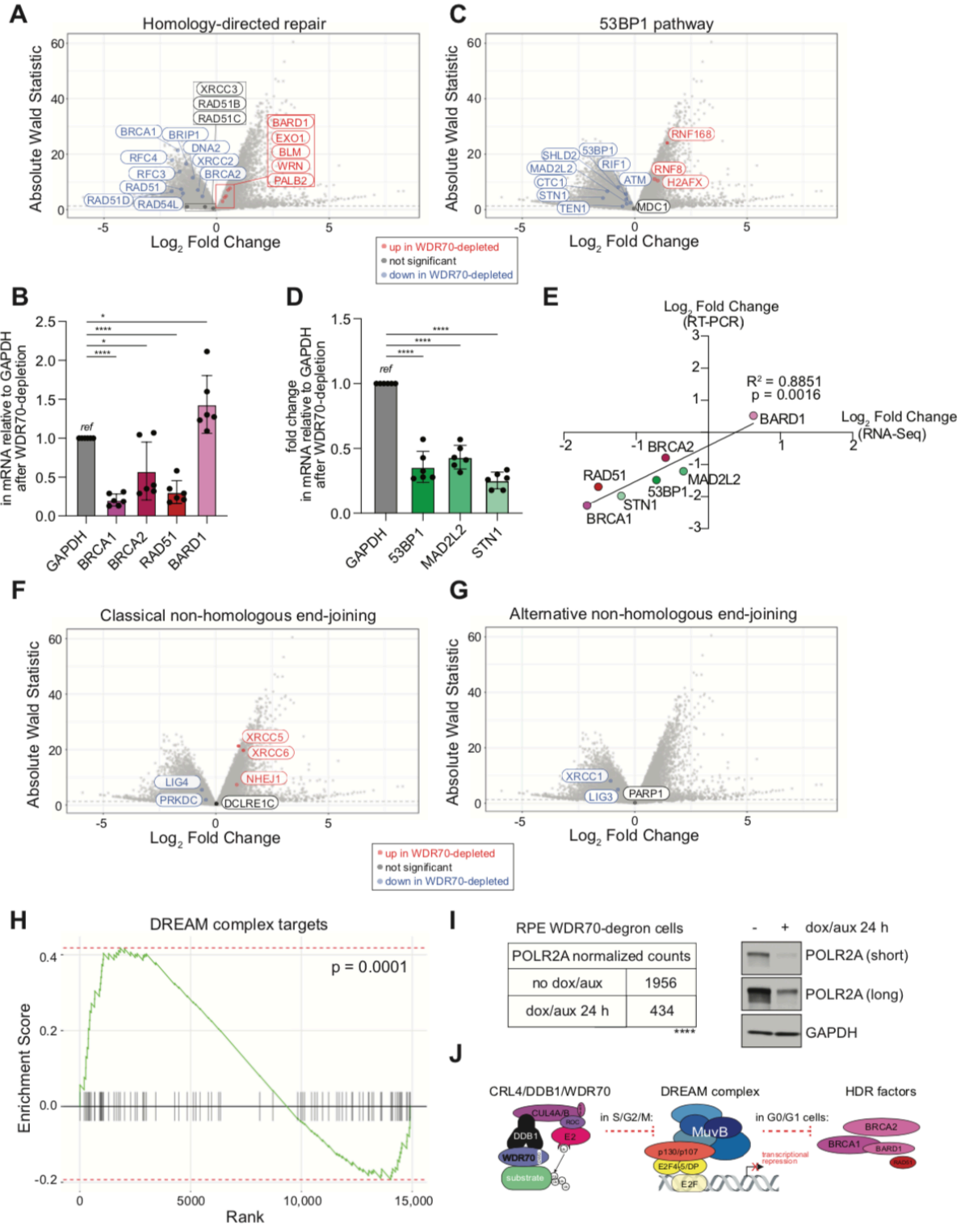

Figure 4.10. WDR70 loss affects RNA levels of DDR and other factors. (**A**) Volcano plot depicting Log_2 fold change and absolute Wald Statistic for transcripts in WDR70-depleted cells (dox and aux for 24 h). Negative Log_2 fold change (blue dots and labels) indicates transcripts which are less abundant in WDR70-depleted cells. Positive Log_2 fold change (red dots and labels) indicates transcripts which are more abundant in WDR70-depleted cells. Absolute Wald Statistic above 1.96 (marked by the dashed line) is considered significant. Black dots and labels indicated genes which were not differentially regulated. Transcripts of factors involved in homology-directed repair are highlighted. **(B)** RT-PCR data showing the fold change in mRNA of the indicated HDR factors relative to GAPDH in WDR70-degron cells. Two primer pairs were used for each gene in three independent biological replicates. **(C)** As in **(A)**, except depicting transcripts of factors involved upstream and downstream of 53BP1-mediated DSB processing are highlighted. **(D)** RT-PCR data as in **(B)** showing fold change for 53BP1, MAD2L2, and STN1. **(E)** Correlation between Log_2 fold change derived from RT-PCR (y-axis) and Log_2 fold change derived from RNAseq (x-axis) for the indicated genes. Simple linear regression was performed to determine the R^2 value, and the p value indicates a slope which is significantly non-zero. **(F, G)** Volcano plots as in **(A).** Transcripts of factors involved in repair by classical non-homologous end-joining **(F)** and alternative non-homologous end-joining **(G)** are highlighted. **(H)** GSEA plot showing differential expression in WDR70-depleted cells of 88 predicted targets of the DREAM complex[197]. Genes are ranked along the x-axis with the most downregulated genes in WDR70-depleted cells at the left. **(I)** RNAseq and immunoblot analysis of POLR2A. Left, average normalized POLR2A counts from three technical replicates in dox/aux-treated and control WDR70-degron cells (Log_2 fold change = -1.90; $p = 1.37 \times 10^{-8}$). Right, immunoblot showing POLR2A levels in the same cells. Representative of two independent experiments. **(J)** Speculative model for how CRL4/DDB1/WDR70 and DREAM control the expression of HDR factors BRCA1, BRCA2, and RAD51 among others. Statistical analyses as in Figure 1 except where otherwise indicated.

Surprisingly, KU70/80 transcripts were increased (Figure 4.10F) despite protein levels being unaffected by WDR70 loss (Figure 4.6D). In WDR70-depleted cells, transcript levels for the aNHEJ pathway genes XRCC1, LIG3, and PARP1 (Figure 4.10G) corresponded to the protein levels of those factors reported above (Figure 4.6B).

Many genes involved in cell cycle control, DNA replication and repair, and transcriptional regulation were affected by WDR70 loss. The collective regulation of myriad cell cycle components and particularly DDR factors was reminiscent of the DREAM complex, a p130-containing RB-like complex which usually functions as a

transcriptional repressor at E2F or CHR elements but upon dissociation of p130 and E2F can also act as an activator[195,196]. Meta-analyses have suggested hundreds of targets of the DREAM complex including BRCA1, BRCA2, RAD51, and other DDR factors[197]. We queried our RNAseq dataset to determine whether 88 predicted DREAM targets[197] were affected by WDR70 loss. Indeed, WDR70 loss caused significant dysregulation of DREAM targets, with some strongly increased and others substantially decreased (Figure 4.10H). Finally, we noted that POLR2A, the catalytic subunit of RNA polymerase II, was dramatically reduced in WDR70-depleted cells at the RNA and protein level (Figure 4.10I) which may account (in part) for reduced transcription of some genes, although many were significantly increased as well (Figure 4.10A-D). Collectively, the data indicate that WDR70 loss has a broad effect on cellular mRNA levels including the reduction of transcripts of many HDR and 53BP1 pathway factors, which corresponded to the loss of those factors observed at the protein level.

4.11 H2BK120R does not affect RAD51 loading or PAPRi-induced radial formation

It was previously proposed that monoubiquitination of H2B by CRL4/DDB1/WDR70 impacted resection and therefore HDR[183,191]. We expressed a dominant negative histone, H2BK120R, which cannot be ubiquitinated[192], yet this did not recapitulate BRCA1 phenotypes like loss of RAD51 loading or PARPi-induced radial chromosomes (Figure 4.11A, B). Loss of WDR70 also did not affect levels of RNF20, the ubiquitin ligase responsible for depositing H2BK120Ub (Figure 4.11C)[192,193]. We did observe minor decreases in H2BK120ub after WDR70 loss, in agreement with past experiments[183,191,194] (Figure 4.11D). Thus, the data presented here argue against a

major role for WDR70 downstream of BRCA1, for example, through ubiquitination of H2B. Instead, our data show that WDR70 promotes the expression of various DDR factors, and specifically promotes the focus-forming ability of HDR factors including BRCA1 and RAD51.

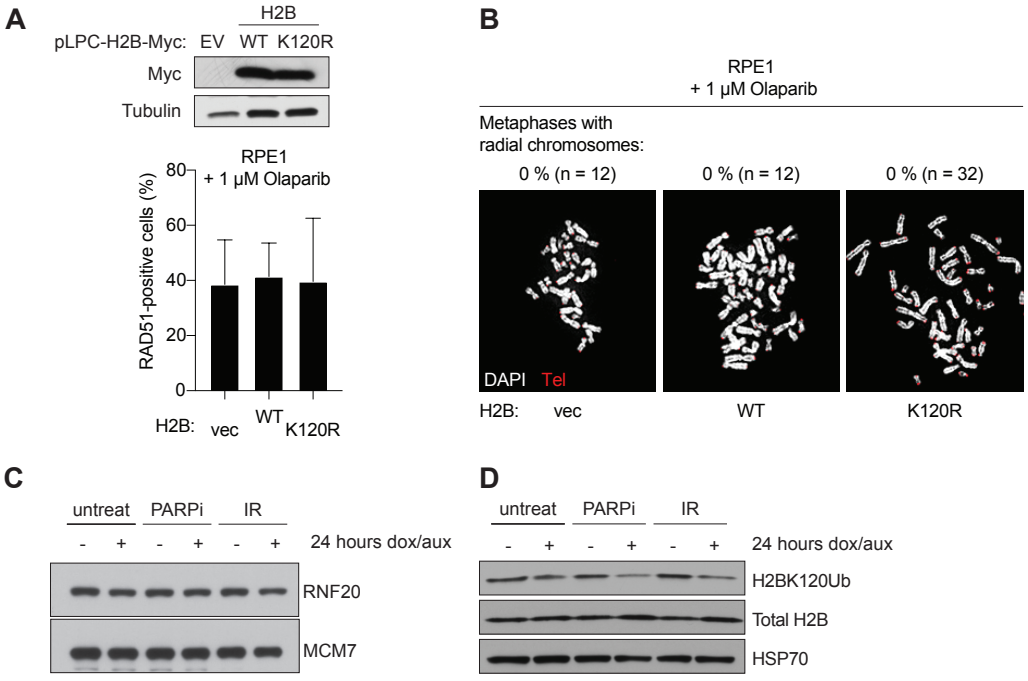

Figure 4.11. H2BK120R does not affect RAD51 loading or PARPi-induced radial formation. A, Top, Immunoblots for Myc and Tubulin from RPE1 cells transfected with wild-type (WT) or dominant negative (K120R) H2B constructs. Bottom, Quantification of the percent of cells with > 10 RAD51 foci per nucleus in cells as in **A**. **B**, Representative DAPI-stained metaphase spreads from cells as in **A**. **C**, Immunoblot for RNF20 after WDR70 loss in WDR70-degron cells with the indicated treatments. MCM7 is used as a loading control. Immunoblot performed by Keshav Sharma. **D**, Immunoblot for H2BK120Ub after WDR70 loss in cells as in **C**. All panels representative of multiple experiments. Equal amounts of protein were loaded based on BCA assay and Ponceau stain.

4.12 Discussion

We initially speculated that BRCA1-mediated eviction of shieldin/CST from DSBs would necessitate the involvement of a downstream effector of BRCA1, and we proposed two candidates. Our experiments on SMARCAD1 did not reproduce published data[179] and do not support a role for SMARCAD1 in association with BRCA1. We next queried WDR70 which, although it localized to DSBs, did so in a BRCA1-independent manner. By employing the auxin system for rapid degradation of WDR70, we identified a regulatory role for CRL4/DDB1/WDR70 in the DDR. CRL4/DDB1/WDR70 affects multiple DSB repair pathways but is particularly relevant to HDR. Yet our work raises questions about how and why WDR70 performs this role in genome integrity, selectively regulating DDR factors involved in HDR, 53BP1/RIF1/shieldin/CST pathway, and aNHEJ, but not cNHEJ.

How does WDR70 loss lead to this striking phenotype? One candidate for such regulation is the DREAM complex[195,196]. Many cell cycle genes and DDR factors including BRCA1, BRCA2, and RAD51 have promoters which are bound by subunits of the DREAM complex[195, 197]. We observed that in WDR70-depleted cells a group of predicted DREAM targets were strongly dysregulated (Figure 4.10H). The subunit composition and the activity of the DREAM complex depends on the cell cycle phase. The MuvB subunits of the DREAM complex dissociate from p130/p107 and associate with FOXM1 or B-MYB to function as a transcriptional activator in S/G2/M, while the repressive role of the DREAM complex is pronounced in G0/G1 cells[196,198]. We speculate that the repressive effect of the DREAM complex—which normally is restricted to G0/G1—is activated in S/G2/M when CRL4/DDB1/WDR70 is disrupted

(Figure 4.11J). Perhaps CRL4/DDB1/WDR70 degrades an inhibitor of the DREAM complex in S/G2/M or otherwise antagonizes the DREAM complex in a cell-cycle-regulated manner. Our work hints at a connection between CRL4/DDB1/WDR70 and the DREAM complex, but testing this will require further analysis across cell types and cell cycle phases.

It has also been observed that hypoxia induces loss of HDR proteins[199–201] in a manner reminiscent of WDR70-depleted cells, but it is not known how WDR70 may be affected by hypoxia. We note that hypoxia-inducible factor 1 alpha inhibitor (HIF1AN) mRNA levels were substantially lower in WDR70-depleted cells (Log2 fold change = -1.85; $p = 3.88 \times 10^{-36}$), so it is feasible that a transcriptional program like that of HIF1a stabilization is instated upon WDR70 loss. A noteworthy finding from our RNAseq of WDR70-degron cells was that POLR2A transcripts were decreased in cells lacking WDR70, suggesting that transcription may be reduced globally. However, some mRNAs (e.g., those pertaining to some upstream DDR signaling or cNHEJ factors) were unaffected, and indeed many were increased after 24 h of WDR70 degradation. The WDR70 phenotype, therefore, cannot be explained by decreased transcription alone. Whether WDR70 acts through known transcriptional regulators like the DREAM complex or HIF1a or through another mechanism, the regulation (and indeed, the selective advantage) of such a cellular program which affects many resection-relevant DDR factors will be of interest.

RNA sequencing in yeast wdr70Δ cells did not reveal major transcriptional differences as compared to wild-type cells[183], suggesting that the regulatory function of WDR70 may have evolved in higher eukaryotes. Studies in yeast proposed a role for

WDR70 in promoting resection through ubiquitination of H2B[183, 191], but human WDR70 affects the expression of myriad genes with two of the most affected genes being BRCA1 and RAD51. Therefore, our data support the notion that the effect of WDR70 on resection and HDR is likely indirect.

BRCA1 and 53BP1, which have been discussed as determinants of DSB repair pathway choice, were decreased at the levels of mRNA and protein after WDR70 degradation (Figures 4.4, 4.5, 4.10). However, 53BP1/RIF1 foci formation was unaffected by WDR70 loss, while HDR foci formation was abrogated (Figure 4.7). It is plausible that defects in WDR70 activity could resemble HDR-deficient cells or cancers, but the essential and pleiotropic[191,202] nature of WDR70 argue against the likelihood of total loss of function of the gene in cancer.

CHAPTER 5. Discussion

5.1 DSB repair by CST-mediated fill-in synthesis

In this thesis, we introduce CST-mediated fill-in synthesis as a novel mechanism in DSB repair by the 53BP1 pathway. CST recruited to telomeres by shelterin functions to keep telomeric 3' overhangs from becoming overly long, counteracting the effect of resection [65,83]. The data presented here argue that 53BP1/shieldin-mediated recruitment of CST to DSBs plays an analogous role and opposes the formation of long 3' overhangs at DSBs. We have demonstrated the involvement of CST, Polα, and primase downstream of 53BP1/shieldin (Chapters 2[35] and 3), and presented compelling evidence of fill-in synthesis in the form of nucleotide analog incorporation at DSBs (Chapter 3; Figure 3.3-6).

Yet there are several remaining questions which will be discussed in this chapter. First, there is the issue of the role of fill-in synthesis in the three contexts where the effect of the 53BP1 pathway is most apparent: opposing resection at telomeres lacking end protection of shelterin; CSR in the immune system; and BRCA1-deficient cells treated with PARPi. As discussed previously[136] (Chapter 1), these context-specific reactions have served as the surrogates for study of how the 53BP1 pathway works. In this Chapter, I discuss the role of CST-mediated fill-in synthesis in each context, and how our novel shieldin mutant (SHLD1Δ) revealed potential differences between the three contexts. Second, I will address the involvement of 53BP1/shieldin/CST-mediated DSB repair outside these three contexts—i.e., in 'normal' DSB repair (repair of genome-wide DSBs in BRCA1-proficient cells). While the 53BP1 pathway has generally been discussed in terms of DSB "repair pathway choice" favoring cNHEJ[2,3], our data in

Chapter 2[35] and the “Escort” model of Chapter 1[136], and other recent publications have complicated this notion[150,158]. Currently the data support a role for fill-in synthesis at DSBs outside of the three special contexts, but how and when fill-in synthesis is deployed as well as the fidelity of the repair products remains to be determined.

5.2 CST-mediated fill-in synthesis at dysfunctional telomeres, in CSR, and in BRCA1-deficient cells treated with PARPi

Here I discuss the advances in understanding the downstream steps of the 53BP1 pathways in three context-specific reactions and outline the challenges remaining to fully elucidate the mechanism. Our data using telomeres which lack end protection of TPP1 or TRF2, and therefore undergo extensive 5’ end resection, demonstrate a role for the CST complex in opposing such resection (Chapter 2; Figures 2.1, 2.4[35]). Given that the primary known function of CST is as a Polα/primase accessory factor, this is highly suggestive that CST counteracts resection through fill-in synthesis, though disruption of Polα/primase would be needed to validate the model. Such experiments are challenging due to the essential nature of Polα/primase and the long time-frame (~ 96 h after Cre-mediated shelterin removal) of the protocol. We attempted to use a SHLD1 mutant (SHLD1Δ), which is defective in its interaction with CTC1, to test the role of CST downstream of shieldin at dysfunctional telomeres, but the mutant proved uninformative in this context (see Chapter 3.7 Discussion). At present, it is unclear whether SHLD1Δ still recruits enough CST to counteract resection in this context, but depletion of CST in the presence of SHLD1Δ could resolve this issue. Alternatively, a different genetic perturbation of shieldin or CST may be needed to disrupt recruitment of

CST to dysfunctional telomeres and determine whether the primary role of shieldin in this context is recruitment of CST. If data emerges that shieldin has the ability to directly block resection, as has been proposed[123,134,158], separation of function mutants will be informative to establish the relative contributions of a block to resection vs. counteracting resection by fill-in. Another mystery remaining is how CST contributes to end-to-end fusions of telomeres lacking TRF2 (Chapter 2; Figure 2.9[35,90]), and, although this is largely outside the scope of this Chapter, it is discussed in Chapter 1[136].

We have argued that the primary functions of 53BP1 were well-adapted for the setting of CSR, and it is thought that the shieldin complex co-evolved with CSR[89,136] (Chapter 1). 53BP1/RIF1/shieldin clearly promote CSR, but the current data on the role of CST must be expanded upon to test whether fill-in plays a part in this DSB repair reaction. Again, due to the essential nature of CST/Polα/primase and the duration of CSR experiments, this poses a challenge. One study found that two heterozygote CTC1 clones showed reduced CSR[90], but why CST might be haploinsufficient in CSR is unclear. Similar to the setting of dysfunctional telomeres, SHLD1Δ was uninformative as it still supported normal CSR, though it was not determined whether CST retained its interaction with shieldin in this setting (Figure 3.14). Given that in CSR staggered nicks generate multiple DSBs with 5' and 3' overhangs of various sizes, this context may be of limited utility for understanding the roles—separately or together—of shieldin and CST, even if (ironically) it proves to be the DSB reaction for which shieldin evolved and possibly co-opted CST from a telomeric function to a genome-wide role[136]. It is also possible that 53BP1/shieldin mediated fill-in synthesis at DSBs in cells outside of the immune system conferred a selective advantage.

The final context where 53BP1/shieldin function has been studied is in BRCA1-deficient cells treated with PARPi. We showed in Chapters 2 and 3 that CST/Polα/primase disruption mirrors the loss of shieldin, and combined loss confers no further defect, indicating that CST/Polα/primase functions downstream of shieldin. In this setting, SHLD1Δ failed to recruit CST and mimicked shieldin-deficiency; yet re-establishing the shieldin-CST link through chemical dimerization of SHLD1Δ with CTC1 was sufficient to fully restore shieldin function (Figure 3.13). Thus, the data indicate that in this context, the primary function of shieldin is recruitment of CST. Is there any possibility, then, that in BRCA1-deficient cells resection can be blocked as has been proposed? Our data argue against a separate function for the shieldin complex blocking resection, as the entire effect of shieldin loss on radial chromosome formation and RAD51 loading can be reinstated by restoring CST recruitment, and presumably fill-in synthesis (Figure 3.13I-K). One possibility is that 53BP1 itself blocks resection independently of shieldin. In radial chromosome formation, the ability of 53BP1 to both promote DSB mobility and counteract resection contributes to cNHEJ[35,75]. However, in RAD51 loading assays after IR, loss of shieldin/CST/Polα/primase generally only confers a partial rescue of RAD51 loading compared to 53BP1[35,91] (though this is not always the case[90,92]), yet DSB mobility is not known play a role in suppressing RAD51 loading. It is therefore possible that at IR-induced DSBs, 53BP1 poses an as-yet unidentified barrier to resection in BRCA1-deficient cells. However, in BRCA1-deficient cells treated with PARPi, the data currently favor the model that fill-in synthesis and not a block to resection is the primary effector of 53BP1/shieldin function.

5.3 CST-mediated fill-in in normal DSB repair: revisiting the fidelity model

While the above three contexts have helped elucidate the 53BP1 pathway, comparatively less work has been done on the consequences of 53BP1 deficiency in wild-type cells. Yet there is now compelling evidence that 53BP1/shieldin-mediated fill-in synthesis does occur in normal cells. We detected fill-in synthesis in at FOKI-induced DSBs in U2OS cells (Chapter 3; Figure 3.3, 4), and recent studies also gave evidence for fill-in synthesis at nuclease-induced DSBs[150,158]. The outcome of 53BP1 pathway action in the three specialized contexts is very clear: end-to-end telomere fusions; productive class switching; and radial chromosomes. But what is the repair outcome when 53BP1 functions outside of these contexts? One recent study demonstrated 53BP1/shieldin/CST/Polα/primase-dependent tandem duplication formation Cas9 nickase-generated breaks that yield complementary 3' overhangs which are subsequently repaired by cNHEJ[150]. It is not yet clear whether this context is a valid surrogate for 53BP1 pathway action in normal cells, or more akin to the context-specific reactions described above. Additionally, this study proposed that primase could begin fill-in synthesis at or near the 3' tip, in contrast to our assertion that fill-in synthesis is incapable of re-generating a blunt end[136]. This is a dichotomy with potential implications for the fidelity of repair by fill-in synthesis.

Similarly, Polα-dependent fill-in synthesis was detected at AsiSI-induced cuts in Abl-transformed murine pre-B cells[158]. This experimental protocol used non-dividing, LIG4-deficient cells and a long time period of DSB induction to detect DNA synthesis, so it is not clear if this system represents a physiological type of DSB repair. This study, though presenting compelling evidence of fill-in synthesis, also revisited the question of

a block to resection, now in the context of 'normal' DSB repair. They detected residual Polα fill-in activity at DSBs in 53BP1- or shieldin-deficient cells. Since they found that this fill-in was not sufficient to counteract resection by EXO1, they concluded that 53BP1 normally poses a block to resection as well as recruiting the fill-in machinery[158]. However, it is also possible that the fill-in synthesis by CST/Polα/primase is more robust (e.g., more processive or more active) when it is recruited by 53BP1/shieldin, explaining why CST/Polα/primase by itself is incapable of fully counteracting resection by EXO1. Further experiments on 53BP1/shieldin deficiency will be needed to clarify this issue, and direct evidence of a mechanism by which 53BP1/shieldin block resecting nucleases is still lacking.

The key tenets of the 53BP1 fidelity ("Escort") model from Chapter 1 that must be tested are: 1) can fill-in synthesis re-generate near blunt ends at DSBs[150], or is some ssDNA predicted to remain after shieldin/CST engagement[136]? 2) does this DNA substrate remain bound by shieldin/CST, and are these protein complexes barriers to RAD51 loading and HDR that must be removed in order for recombination to occur (see also Chapter 1 and Appendix)? 3) does fill-in synthesis at "normal" DSBs lead to cNHEJ[150] as it does in the three context-specific reactions, or could it also lead to HDR as we have proposed[136]? 4) does the 53BP1 pathway prevent mutagenic outcomes like SSA[136,156], or might fill-in synthesis by Polα, which has low processivity and lacks proofreading ability, also potentially promote mutagenesis? Resolution of these issues will provide insight into the role of this enigmatic pathway in genome integrity in normal cells and in cancer.

APPENDIX: CST localizes to DSBs in mitosis and the subsequent G1

1. Introduction

In asynchronous interphase nuclei, we previously observed 53BP1/shieldin-dependent CST localization to telomeres lacking TPP1 in mouse cells (Figure 2.5A-C) and IR-induced foci in human cells (Figure 2.5D-F). We further demonstrated that CST-mediated fill-in synthesis prevents RAD51 loading and promotes PARPi lethality in BRCA1-deficient cells (Figure 2.10). During the course of these studies, we also examined CST localization to PARPi-induced damage in BRCA1-deficient cells. These data are presented and discussed in this appendix. We observed CST localization at breaks in metaphase spreads despite the absence of 53BP1, and CST localization in G1 cells forming chromatin bridges after PARPi treatment. Thus, CST localizes to DSBs throughout the cell cycle, though the functional significance of CST localization in mitosis and the subsequent G1 remains unclear.

2. CST localizes to breaks in mitosis and the subsequent G1

In TPP1-deficient MEFs, myc-tagged CTC1 colocalizes with γH2AX at dysfunctional telomeres in an ATR/53BP1/shieldin-dependent manner (Figure 2.5A-C). However, in mouse cells with intact shelterin, CST localization to telomeres is strong (Figure 2.5A), making studies of CST colocalization with random DSBs challenging. We therefore examined whether CST was enriched at γH2AX foci in PARPi-treated BRCA1-deficient cells, excluding the abundant telomeric foci such that colocalizations scored likely represent random non-telomeric DSBs where CST localizes. Deletion of BRCA1

significantly increased the percentage of γH2AX foci with CTC1 signal colocalizing (Figure App.1A, B). 53BP1 does not accumulate at breaks in mitosis[203], a finding which

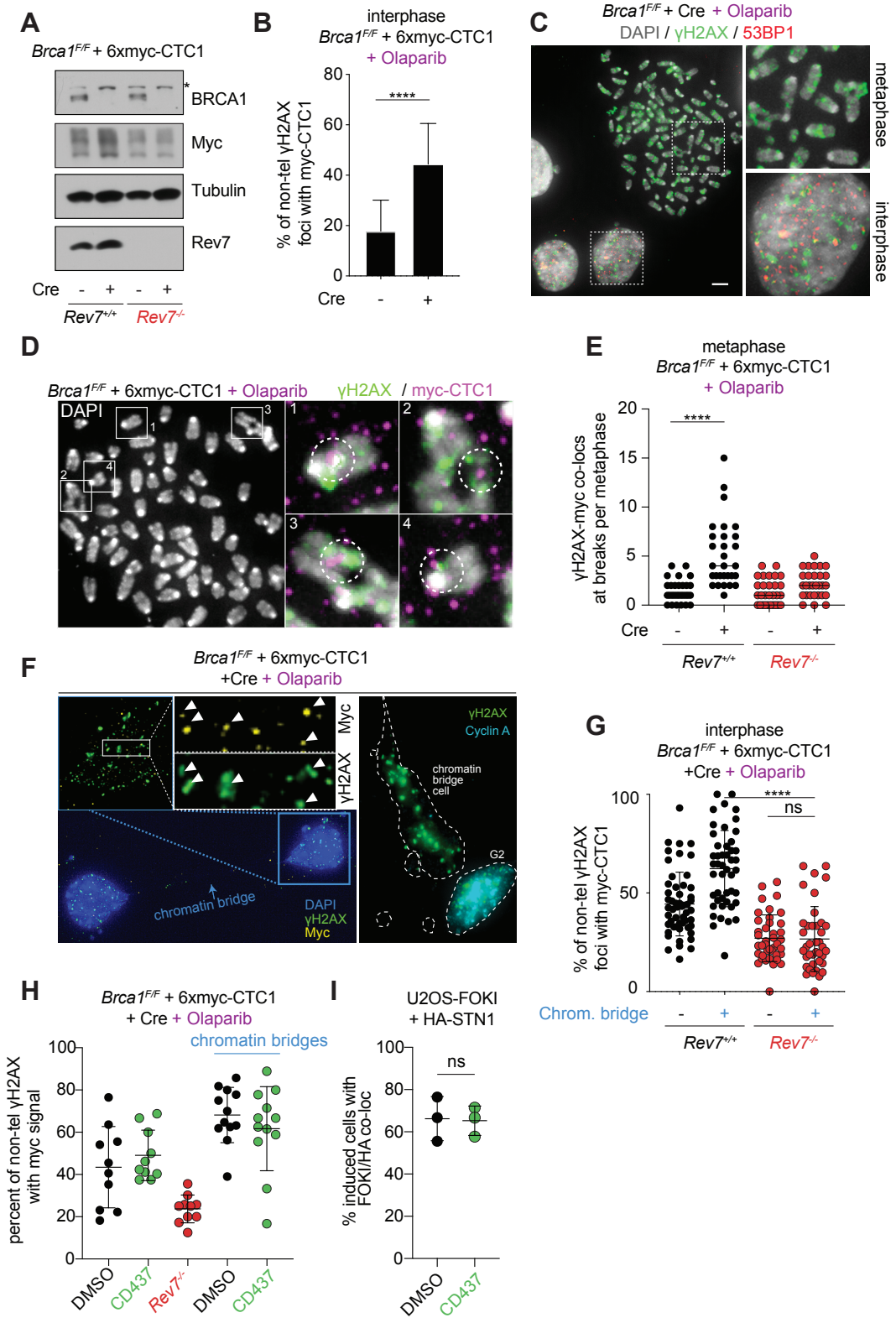

Appendix Figure 1. CST foci persist into metaphase and subsequent G1. A, Schematic of fill-in synthesis by 53BP1/shieldin/CST/Polα/primase. **B**, Immunoblot showing BRCA1 deletion by Cre in the indicated MEF cell lines harboring 6xmyc-tagged CTC1. Asterisk: non-specific band. **C,** BRCA1-deficient, PARPi-treated metaphase spreads (DAPI) with metaIF for detection of γH2AX and myc-tagged CTC1 at breaks in DAPI-stained chromosomal material. **D,** Quantification of γH2AX and myc-CTC1 co-localization at breaks in DAPI-stained chromosomal material in cells as in **B, C**. **E,** Schematic of fill-in synthesis by in cells where shieldin is absent as in **B-D**. **F**, Quantification of the percent of non-telomeric γH2AX foci co-localizing with myc-CTC1 in cells as in **B, D**. Cells displaying a DAPI-stained chromatin bridge are scored separately. **G**, Representative IF of chromatin bridge-containing cells as in **F**. Left, γH2AX and myc-CTC1 co-localization in a BRCA1-deficient cell treated with PARPi. Right, Cyclin A IF demonstrating that such chromatin bridge cells are in G1 (lack of cyclin A stain as compared to a neighboring cyclin A positive cell which is presumably in G2). **H,** Representative metaIF for γH2AX and 53BP1 in PARPi-treated, BRCA1-deficient cells. Zoomed images demonstrate the lack of 53BP1 stain in metaphase, as compared to neighboring interphase cells. **J,** Quantification of cells as in B-D with or without Polα inhibitor (CD437). Cells with chromatin bridges are scored separately as in **F**. **K**, Quantification of HA-mCherry co-localizations in U2OS-FOKI cells harboring HA-tagged STN1 (as in Figure 3.5**D, E**) with or without Polα inhibitor (CD437). All means are indicated with center bars and SDs with error bars. Statistical analysis based on two-tailed Welch's t-test. *, $p<0.05$; **, $p<0.01$; ***, $p<0.001$; ****, $p<0.0001$; ns, not significant.

we confirmed by metaIF[171–173](data not shown). Even when BRCA1 was deleted, cells treated with PARPi, which show many 53BP1 foci in interphase nuclei in this protocol, did not show 53BP1 stain on metaphase chromatin (Figure App.1C). As expected[203], γH2AX was detectable in metaphase (Figure App.1C). We suspected that CST, as a downstream effector of 53BP1 would similarly fail to form foci in mitosis. Surprisingly, metaIF for detection of γH2AX and myc-tagged CTC1 (Figure App.1D, E) revealed γH2AX and myc-tagged CTC1 colocalizations at chromosome breaks. Myc-CTC1 foci were abundant in this metaIF protocol, suggesting that the protocol could be optimized (e.g., for metaPLA (see Chapter 3; Figure 3.5)) to rule out spurious colocalizations. Nevertheless, γH2AX/CTC1 colocalizations were not observed in BRCA1-proficient cells, nor when the REV7 component of shieldin was deleted (Figure App.1E).

Given the enrichment of CTC1 at sites of damage in BRCA1-deficient metaphase spreads, we re-examined asynchronous BRCA1-deficient treated for 24 h with PARPi for γH2AX/CTC1 colocalizations in cells throughout the cell cycle. One class of cell stood out due to its striking γH2AX/CTC1 colocalizations: cells with DAPI-rich chromatin bridges at the time of fixation (Figure App.1F). Such cells, which were Cyclin A negative and thus presumed to be in G1(Figure App.1F), showed high levels on non-telomeric γH2AX colocalization with CTC1 (Figure App.1F, G). As was the case in metaphase, deletion of REV7 reduced the colocalization of CST with sites of damage in PARPi-treated BRCA1-deficient interphase nuclei (Figure App.1G). Unsurprisingly, chemical inhibition of Polα did not affect γH2AX/CTC1 colocalizations in the bulk population or specifically in cells with chromatin bridges (Figure App.1H). Additionally, in human U2OS cells, CST enrichment at FOKI-induced DSBs (Figure 2.7) was unaffected by Polα inhibition (Figure App.1I). Collectively, these data suggest that shieldin-dependent CST localization to DSBs in BRCA1-deficient cells occurs throughout the cell cycle, even in mitosis when 53BP1 does not localize to sites of DNA damage. These γH2AX/CTC1 colocalizations are most evident in G1 cells forming chromatin bridges after treatment with PARPi.

3. Discussion

53BP1, RIF1, and SHLD3 form large globular foci at sites of damage throughout interphase, albeit with increased number and intensity in G1[89,103,104,131]. REV7 and the remainder of shieldin, along with CST/Polα form smaller foci whose colocalization with the upstream factors is more subtle[35,87,89]. Here we describe a novel localization pattern

to sites of damage for the CST complex in BRCA1-deficient cells—in metaphase, and in G1 cells forming chromatin bridges. What is the possible significance of CST localization to such sites in these cell cycle phases?

In BRCA1-deficient cells treated with PARPi, it is generally thought that PARPi during S phase is required for DSB generation, though other models including ssDNA gap formation are proposed[204,205]. We previously showed that fill-in synthesis by Polα which leads to radial chromosome formation occurs late in G2, before or during nuclear envelope breakdown, but not after (Figure 3.7, for model see Figure App.2A). Why then,

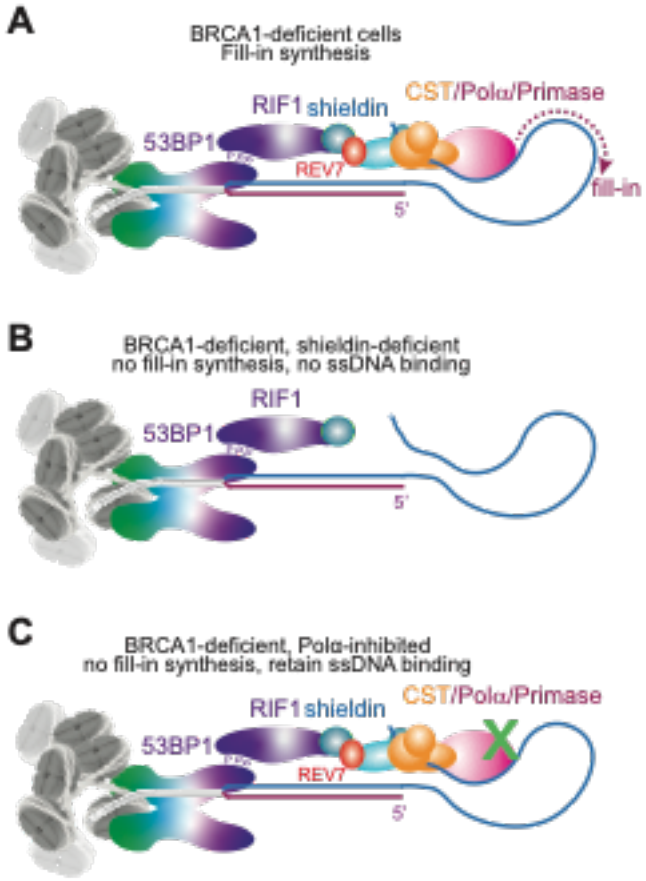

Appendix Figure 2. Models of DSBs in BRCA1-deficient cells. A, Schematic of fill-in synthesis by 53BP1/shieldin/CST/Polα/primase. **B,** Schematic of fill-in synthesis by in cells where shieldin is absent. **C,** Schematic of fill-in synthesis by in cells where Polα is inhibited.

might CST also localize to sites of damage in metaphase? In Chapter 1, we speculated that BRCA1 may antagonize the persistence of shieldin and/or CST complexes at DSBs, a notion consistent with our observation of increased CST foci in BRCA1-deficient cells (Figure App.1B, D, E). However, it is not at present clear how CST might persist at sites of damage in metaphase without the tethering ability of 53BP1 (Figure App.1C)[203]. Polα fill-in synthesis activity independent of 53BP1/shieldin has recently been proposed[158], so it is possible that CST remains bound at certain, possibly G-rich sites, without 53BP1, but further genetic and biochemical experiments are needed to develop this model.

It is worth questioning the relevance (if any) of the CST persistence about which we have speculated. When shieldin is absent, not only is fill-in synthesis lost, but also ssDNA binding activity of the complex (for model see Figure App.2B). Shieldin loss in BRCA1-deficient cells allows for RAD51 loading and diminishes radial chromosome formation[89,91,105]. On the other hand, Polα inhibition alone (which we have shown does not affect CST localization (Figure App.1H, I)) greatly diminishes radial formation[35] (Figures 2.10, 3.7). In this scenario, presumably enough ssDNA is made available by the lack of fill-in that HDR can occur (Figure 3.7E, for model see Figure App.2C), yet ssDNA binding by shieldin/CST should remain. Thus, the persistence of shieldin/CST at DSBs *per se* does not seem to suffice for blocking RAD51 loading and end-joining in this pathophysiological setting. However, in DSB repair in BRCA1-proficient cells, it remains possible that BRCA1 plays a role in antagonizing the downstream factors in the 53BP1 pathway, thus promoting HDR as we have proposed (Chapter 1), but this model awaits experimental validation.

MATERIALS AND METHODS

Cell culture

Cell culture was performed in biosafety cabinets, and cells were cultured at 37˚, 5% CO_2, and 20% O_2 unless otherwise stated. MEFs were isolated from E12.5 embryos and immortalized with pBabeSV40 large T antigen (a gift from G. Hannon) at early passage (P2/3), as described previously[66]. Genotypes were determined by Transnetyx Inc. using real time PCR with allele-specific probes. MEFs were cultured in Dulbecco's Modified Eagle Medium (DMEM, Corning) supplemented with 15% fetal bovine serum (FBS) (Gibco), non-essential amino acids (Gibco), 2 mM L-glutamine (Gibco), 100 U/ml penicillin, 100 µg/ml streptomycin (Gibco), 50 mM β-mercaptoethanol (Sigma). Cre-mediated gene deletion was achieved by three infections with retroviral pMMP Hit&Run Cre[66]. Time points of cell harvest indicate hours after the second Cre infection, and cells were harvested at 96 h after Cre unless otherwise noted.

293FT, Phoenix Ampho and Eco cells, and conditional POT1 knockout HT1080 clone c5[84] were cultured in DMEM supplemented with 10% bovine calf serum (BCS), non-essential amino acids, L-glutamine, and penicillin/streptomycin as above. RPE1 cells were cultured in DMEM/F-12 media (Gibco) supplemented with 10% FBS and penicillin/streptomycin as above. *CH12-F3* cells were cultured in RPMI supplemented with 5% NCTC-109 medium, 10% FCS, 100 U/ml penicillin, 100 ng/ml streptomycin and 2 mM l-glutamine at 37 °C with 5% CO_2 under ambient oxygen conditions. Human $CTC1^{F/F}$ HCT116 cells[163] were cultured in McCoy's 5A supplemented with 10% FCS, non-essential amino acids, L-glutamine, and penicillin/streptomycin as above. CTC1

gene deletion was induced with 0.5 mM 4-OHT for 5 h. Gene deletion was confirmed by Western blot using anti-Ctc1 antibody (MABE1103, Millipore) or an unpublished antibody made by John Zinder in the de Lange lab.

U2OS cells were cultured as the MEFs described above. U2OS cells containing a LacO array and a tamoxifen- and Shield1-regulated mCherry-FOKI-LacI fusion were used as described[169]. Cells were harvested 4 h after induction of FOKI by addition of 0.1 mM Shield1 and 10 mg/ml 4-OHT. For detection of BrdU in FOKI cells, BrdU was added during FOKI induction, and S-phase cells displaying global BrdU incorporation were excluded from BrdU/FOKI colocalization analysis. When Polα inhibitors were used in the U2OS-FOKI cell line, they were added for 30 m before induction of FOKI and remained in the media for the duration of DSB induction.

A complete list of cell lines used can be found in Table 1.

Retroviral Expression Constructs

Retroviral construct expression was performed by calcium phosphate transfection according to the de Lange lab protocol (https://delangelab.rockefeller.edu/protocols). Phoenix Ampho (for human cells infections) or Phoenix Eco (for murine cell infections) were plated 24 hr before transfection and then transfected in the evening. The next morning, fresh BCS media was put on the cells. That evening, media was replaced to match the target cells. The overnight viral media collection was filtered through a 0.45 μm filter and put onto the target cells for 12-24 hours. Infections were then repeated one-three times as necessary. A full list of plasmids is available in Table 2.

RNAi and CRISPR

Lentiviral constructs for shRNA (pLKO) or CRISPR/Cas9-mediated (pLentiCRISPRv2) gene disruption were co-transfected with packaging vectors VSV-G, RRE, and REV into 293T or 293FT cells by calcium phosphate transfection. Transfections and infections were performed as above. Viral media was collected beginning at 24 hr after transfection and cells were infected with the filtered viral supernatant. Four to six infections were performed for experiments in Chapter 2 which used 293T cells, while two infections were performed for subsequent experiments as 293FT cells produce more virus. Alternately, Cas9 and sgRNA vectors were delivered by nucleofection (Amaxa Kit R, Lonza). For shRNA, the Sigma MISSON library was used for reference. For CRISPR/Cas9 gene disruption, target sites were determined using ZiFit or Benchling. When CRISPR KO clones were generated, clones were first screened by immunoblotting if an antibody was available. All candidate clones were then verified by Sanger sequencing of Topo-cloned PCR products of the relevant locus to confirm bi-allelic gene targeting.

For the generation of auxin-inducible degron knock-in cell lines, p53- and RB-deficient RPE1-hTERT cells[206] were nucleofected with a donor template plasmid and two CRISPR/Cas9 plasmids targeting the last coding exon of the targeted gene[168,168]. Following selection in G418, mClover-positive cells were subcloned after flow-sorting for Clover and biallelically targeted clones were identified by PCR. HA-tagged OsTIR1[168] under the control of a dox-responsive promoter was introduced into confirmed clones using lentiviral integration followed by selection in blasticidin and single cell cloning. Twelve clones were picked and treated with 2 ug/ml dox for 24 h and harvested for

detection of HA-OsTIR1. Clones with inducible HA-OsTIR1 expression were then tested for efficient auxin-induced degradation of the target gene.

A full list of RNAi and CRISPR target sites is available in Table 3.

Drug Treatments

A complete list of drug and chemical treatments can be found in Table 4.

In-gel analysis of single-stranded telomeric DNA

Mouse telomeric overhang and telomeric restriction fragment patterns were analyzed 96-120 h after Cre treatment by in-gel hybridization with a γ-^{32}P-ATP end-labeled $[AACCCT]_4$ probe, as previously described[66]. Treatment with *E. coli* Exonuclease I prior to MboI digestion was used to verify the 3' terminal position of the ssDNA as described previously[161]. ImageQuant software was used to quantify the single-stranded telomere overhang signals and the signal from total telomeric DNA in the same lane in the denatured gel. In each experiment, this ratio was set to 1 for lanes not treated with Cre or shRNA and the ratios for the treated samples are given relative to this control.

Flow Cytometry

For cell cycle analysis, cells were pulsed with BrdU for 30 min prior to harvest by trypsinization and fixation in cold 70% Ethanol. Cells were washed with 1% BCS in PBS twice, denatured in 2N HCl for 20 m at room temperature, neutralized in sodium tetraborate, washed again, permeabilized in 0.5% Triton X-100, and washed again. Cells were then labelled with BrdU-FITC conjugated ab (BD, 347583), washed, and

then DAPI (0.01 mg/ml final) and RNAse A (100 µg/ml final) was added prior to analysis on a BD-LSRII system. Standard gating schemes were performed to analyze singlets for BrdU-FITC and DAPI content. Flow cytometry analysis for class switch recombination is detailed below, and was performed on Attune NxT (Life Technologies) or BD FACSCanto (Becton Dickinson). All analyses were performed in FlowJo.

Immunoblotting

Sample preparation was performed as described[35,83] according to the de Lange lab protocol using trypsinization or scraping into Laemmli buffer and shearing through a syringe after 5 m boiling. Alternatively, samples were prepared using RIPA lysis buffer (150 mM NaCl, 1%NP-40, 0.5% Sodium deoxycholate, 0.1% SDS, 50 mM TrisHCl pH 8, 0.5 mM PMSF, Roche protease inhibitor table) before protein quantification on a GeneQuant. Even sample loading for SDS-PAGE was always confirmed with Ponceau S staining.

A full list of antibodies used is available in Table 5.

Immunoprecipitation

Immunoprecipitation was carried out as described[35,83], according to de Lange lab protocol. Lysates were prepared in lysis buffer containing 50 mM Tris-HCl (pH 7.4), 150 mM NaCl, 10% glycerol, 0.1% NP-40, Complete protease inhibitor mix (Roche), and PhosSTOP phosphatase inhibitor mix (Roche). Lysate were incubated with 50 U Benzonase for 30 m at room temperature. A full list of plasmids used for co-immunoprecipitation is available in Table 2, and antibodies are indicated in Table 5.

Yeast two-hybrid assays

For interaction analysis by yeast two-hybrid, full-length versions of human CST and shieldin components were cloned into the NdeI site of the pGBKT7 and pGADT7 vectors (Clontech)[35]. Plasmids in pair-wise combinations were co-transformed into budding yeast strain PJ69-4A (*MATa trp1-901 leu2-3,112 ura3-52 his3-200 gal4 gal80 LYS2::GAL1-HIS3 GAL2-ADE2 met2::GAL7-lacZ*) and selected on synthetic complete drop-out media lacking tryptophan and leucine. Protein interactions were tested by plating on the same medium but also lacking adenine.

For the yeast two-hybrid random mutagenesis of human SHLD1, GBD-hCTC1[35] was transformed into budding yeast strain PJ69-4A (above) and selected on synthetic complete drop-out media lacking tryptophan. To recover only full-length SHLD1 variants in the screen, GAD-hSHLD1 was modified to contain a C-terminal ScUra3 gene. SHLD1 was then amplified by error-prone PCR (Taq, NEB) using the following conditions: 2.5 mM each dNTP; 7 mM $MgCl_2$; 0.1 mM $MnCl_2$ in 10x Buffer with $MgCl_2$. GAD-SHLD1WT-Ura3 was digested with Nde1/Age1 to remove the SHLD1 ORF, and the linearized vector was co-transformed with the SHLD1 variant library at a molar ratio of 1 vector: 3 insert into yeast harboring GBD-hCTC1 and plated on synthetic complete drop-out media lacking tryptophan, leucine, and uracil (SC-LTU). Colonies were then replica plated onto drop-out media also lacking adenine (SC-LTUA). Colonies that failed to grow on selective (SC-LTUA) media were picked from permissive media and spot dilutions were plated on selective and permissive media for validation. SHLD1 variant sequences were amplified by colony PCR, column purified, and sequenced.

IF, telomere FISH, and IF-FISH

IF, telomere FISH, and IF-FISH were performed as described according to de Lange lab protocols[35,66,83]. A modified cytoskeleton extraction protocol[207] for harvesting and for IF was employed as follows: dishes with cells on poly-lysine-coated coverslips were put on ice, and cells were washed twice with cold PBS; cells were then incubated in cytoskeleton buffer[207] for 5 m followed by cytoskeleton stripping buffer 5 m[207]. Cells were then washed thrice with cold PBS and fixed at room temperature in 3% PFA/2% sucrose fixative, before washing thrice in PBS at room temperature. Coverslips were pre-extracted with 0.5% Triton X-100 buffer[207] before IF. This protocol was used for the following targets: myc-tagged RPA32; myc-tagged Ctc1; HA-tagged Stn1; SNAP-tagged SHLD1; endogenous Polα; BrdU; or endogenous WDR70.

Standard IF without the cytoskeleton extraction protocol was carried out after fixation in 3% PFA at room temperature for 10 m. A full list of antibodies used for IF is available in Table 5. Highly cross-absorbed Alexa fluor plus 488, 555, and Cy5 or 647 secondary antibodies were used (Thermo Fisher).

Imaging was performed on a Zeiss Axioplan II microscope equipped with a Hamamatsu C4742-95 camera using Volocity software or on a DeltaVision (Applied Precision) equipped with a cooled charge-coupled device camera (DV Elite CMOS Camera), a PlanApo 60x 1.42 NA objective or 100x 1.40 NA objective (Olympus America, Inc.), and SoftWoRx software. Deconvoluted images were max projected before scoring foci manually or with automated foci counting software.

Intensity measurements of RPA32-myc IF were performed in FIJI as follows: nuclei were identified using thresholding. The average image background was then subtracted from the image, and the total raw pixel intensity within each area of interest in the channel of interest was calculated.

For HA-STN1/γH2AX colocalization in RPE1 cells, a random overlap background level was determined by splitting the two image channels, rotating one channel 90 degrees, and merging the channels. Colocalizations were then scored to determine the average overlap of foci by random chance due to telomeric (non-DSB) HA-STN1 foci or other spurious foci.

For 53BP1 cavity scoring, samples were blinded from the investigator, and foci were determined to be either cavity-containing, globular, or ambiguous. After excluding ambiguous foci, the percent of foci containing a cavity was derived from the total foci scored.

Metaphase chromosome analysis and metaPLA

Analysis of misrejoined chromosomes was carried out as described on DAPI-stained metaphase spreads after telomeric FISH which was performed according to the de Lange Lab protocol[35,66,83]. The metaPLA protocol was developed based on a protocol for immunofluorescence on metaphase spreads[171–173]. Cells were treated with BrdU for a total of 1 h (except where otherwise noted), during which colcemid was added for the final 45 minutes. For Polα inhibition, CD437 (10 μM) was added directly to the media for 30 min before addition of BrdU and kept in the media during colcemid treatment. For metaPLA in RPE1 PRIM1-mAID cells, the experimental protocol in Figure 3.2A was

followed, with addition of BrdU 15 min before washout. The PBS and FBS-containing media used for washout contained BrdU, dox, or auxin as appropriate, and cells were released into media containing colcemid, BrdU, dox, or auxin as appropriate for 50 min. Media was then replaced with warm hypotonic buffer (10 mM Tris-HCl, 40 mM glycerol, 20 mM NaCl, 1 mM $CaCl_2$, 0.5 mM $MgCl_2$) for 15 minutes at 37˚. Cells were then harvested by mitotic shakeoff and cytospinning (Shandon Cytospin3) for 10 min at 2,000 rpm. Slides were immediately fixed in 2% PFA in PBS. For metaPLA, cytospin spreads on glass slides were permeabilized in cold Triton X-100 buffer with 0.5% Triton[207] for 5 min, rinsed with H_2O, denatured in 1 N HCl for 10 min, and rinsed again before proceeding with PLA. Mouse γH2AX (05636, Millipore) and rabbit BrdU (152095, Abcam) antibodies were used with - and + probes and Duolink Orange kit (Sigma). PLA foci were only scored at breaks, gaps, or other aberrant chromosome structures. In *Trf2*$^{F/F}$ *Lig4*$^{-/-}$ MEFs, only PLA foci at chromosome termini were scored. The number of PLA foci observed in *Trf2*$^{F/F}$ *Lig4*$^{-/-}$ cells is consistent with not every dysfunctional telomere exhibiting a γH2AX focus in metaphase[208], and/or may reflect inefficiency in proximity labeling.

Telomere fusion assays

SV40LT-immortalized *Trf2*$^{F/F}$ RosaCre cells were infected with STN1 shRNA (or the empty vector) and 24 h later Cre was induced for 24 h with 4-OHT. Cells were harvested, counted (to rule out a proliferation defect), and processed for telomeric FISH on metaphases 72 h after Cre induction. This early time point was selected to avoid any

effect of the STN1 shRNA on proliferation since diminished proliferation reduces fusion frequencies. Telomere fusions were scored as described previously[66].

Survival assays

Cells were seeded in 6-well plates in duplicate at cell- and treatment-appropriate counts ranging from 10 to 10,000 cells per well. For survival after PARPi, after 24 h, cells were treated with Olaparib at the indicated concentrations for 24 h. Cells were then provided with media without Olaparib and incubated for one week with a media change at day 4. Colonies were fixed and stained with 50% methanol, 2% methylene blue, rinsed with water, and dried before counting. The survival percentage at each PARPi concentration compared to untreated cells was calculated using wells with 10-100 colonies clearly visible at the end of the experiment. Two technical replicates at two cell concentrations were scored for each condition in three independent experiments. For RPE1 cells, survival was assessed as above, but treatments and time-courses are described in figure legends and schematics.

Class switch recombination assay

CH12-F3 cells and CRISPR-Cas9 edited *Shld1*$^{-/-}$ derivatives[105] were generated by lentivirus-mediated transduction, using viral supernatants collected from 293T cells co-transfected with third generation packaging vectors and pLenti-PGK-PURO-DEST (Addgene #19068) containing cloned transgene inserts. Typically, cells were spinoculated with polybrene (8 μg/ml) and HEPES (20 mM)-supplemented viral supernatants (1500 rpm, 90 min at 25 °C). Stable cell-lines were subsequently selected

and maintained in the presence of puromycin (0.5 μg/ml). To stimulate CSR to IgA, *CH12-F3* cells were stimulated with agonist anti-CD40 antibody (0.5 μg/ml; Miltenyi Biotec; FGK45.5), mouse IL-4 (5 ng/μl; R&D Systems) and TGFβ1 (2.5 ng/μl; R&D Systems). Cell-surface IgA expression was determined by flow cytometric staining with anti-mouse IgA-FITC antibody (Thermo Fisher; 11-4204-82; MA-6E1). Pellets collected from cultures of ~4 × 10^7 CH12-F3 cells were lysed in BLB (Benzonase Lysis Buffer: 20 mM HEPES pH 7.9, 40 mM KCl, 2 mM MgCl2, 10% glycerol, 0.5% NP40, 50 U/ml Benzonase (Novagen), 0.05% (v/v) phosphatase inhibitors (Sigma-Aldrich) and protease inhibitors (Complete EDTA-free, Roche)) and were incubated on ice for 10 min before a second incubation with adjusted salt (450 mM KCl). TwinStrep-HA-SHLD1 wt, SHLD1ΔLDLP, L20P, or ΔN complexes were isolated from clarified lysates, following their dilution in NSB (no-salt buffer: 20 mM HEPES (pH 7.9), 10% glycerol, 0.5 mM DTT, 0.5 mM EDTA, 0.05% (v/v) phosphatase inhibitors (Sigma-Aldrich) and protease inhibitors (Roche)) to a final salt concentration of 125 mM. Complexes were immunopurified on Strep-Tactin®XT coated magnetic beads (IBA Life Sciences) and washed extensively in wash buffer (BLB supplemented with 125 mM KCl and 0.1% NP-40).

RNA extraction, RT-PCR, RNA sequencing

Total RNA was extracted using RNeasy Plus Mini kit (QIAGEN, 74136). cDNA libraries were generated using Trio RNA-Seq kit (Tecan, 0506). For RT-PCR, cDNA was generated using SuperScript IV First-Strand Synthesis System (Thermo Fisher, 18091050). RT-PCR was performed in technical triplicate using SYBR Green PCR

Master mix (Applied Biosystems, 4309155) and 0.25 μM concentration of each primer on a QuantStudio 12K-flex machine (Life Technologies). Fold change with respect to GAPDH was calculated using the ddCt method. A linear range was confirmed for each primer pair by a five-fold serial dilution curve. Primer sequences can be found in Supplementary Table 1. For RNA sequencing, 75 bp paired-end reads were generated by Illumina NextSeq 500.

RNAseq processing and analysis

Sequence and transcript coordinates for human hg38 UCSC genome and gene models were retrieved from the Bioconductor Bsgenome.Hsapiens.UCSC.hg38 (version 1.4.0) and TxDb.Hsapiens.UCSC.hg38.knownGene (version 3.4.0) Bioconductor libraries respectively. Transcript expressions were calculated using the Salmon quantification software[209] (version 0.8.2) and gene expression levels as TPMs and counts retrieved using Tximport[210] (version 1.8.0). Normalization and rlog transformation of raw read counts in genes were performed using DESeq2[210] (version 1.20.0). For visualization in genome browsers, RNA-seq reads are aligned to the genome using Rsubread's subjunc method (version 1.30.6)[211] and exported as bigWigs normalised to reads per million using the rtracklayer package (version 1.40.6). Genes were identified as differentially expressed between conditions using DESeq2 with a Benjamini Hochberg adjusted p-value cutoff of 0.05. Gene sets were retrieved from MsigDB c2 pathway gene sets (version 7.0), and gene set enrichment analysis was performed using the R Bioconductor fgsea package[212]. For visualization of gene sets, single sample GSEA

analysis was performed using GSVA (version 1.34.0)[213] and heat maps were drawn using the pheatmap R package.

TABLES

Table 1. Cell Lines

Name	Type	Reference
Brca1$^{F/F}$	MEF	{Xu et al., 1999, #59250}
Brca1$^{F/F}$ 53bp1$^{-/-}$	MEF	{Mirman et al., 2018, #105071}
Brca1$^{F/F}$ Rev7$^{-/-}$	MEF	{Mirman et al., 2018, #105071}
Brca1$^{F/F}$ Shld2$^{-/-}$	MEF	Mirman et al. 2022, (NCB in press)
Trf2$^{F/F}$	MEF	{Celli and de Lange, 2005, #61888}
Trf2$^{F/F}$ Lig4$^{-/-}$	MEF	{Celli and de Lange, 2005, #61888}
TPP1$^{F/F}$	MEF	{Kibe et al., 2010, #26051}
TPP1$^{F/F}$ 53BP1$^{-/-}$	MEF	{Kibe et al., 2010, #26051}
TPP1$^{F/F}$ Rif1$^{F/F}$	MEF	{Kibe et al., 2016, #12549}
TPP1$^{F/F}$ Rif1$^{F/+}$	MEF	{Kibe et al., 2016, #12549}
TPP1$^{F/F}$ 53BP1$^{-/-}$	MEF	{Mirman et al., 2018, #105071}
TPP1$^{F/F}$ 53BP1$^{+/+}$	MEF	{Mirman et al., 2018, #105071}
TPP1$^{F/F}$ REV7$^{-/-}$	MEF	{Mirman et al., 2018, #105071}
TPP1$^{F/F}$ Shld2$^{-/-}$	MEF	{Mirman et al., 2018, #105071}
POTb$^{STOP/STOP}$	MEF	{Hockemeyer et al., 2006, #56655}
Tpp1$^{F/F}$ Shld1$^{-/-}$	MEF	Mirman et al. 2022, (NCB in press)
Tpp1$^{F/F}$ Shld1$^{+/+}$	MEF	Mirman et al. 2022, (NCB in press)
Trf2$^{F/F}$ Lig4$^{-/-}$ Shld1$^{-/-}$	MEF	Mirman et al. 2022, (NCB in press)
Trf2$^{F/F}$ Lig4$^{-/-}$ Shld1$^{+/+}$	MEF	Mirman et al. 2022, (NCB in press)
PRIM1-mAID-mClover	RPE1	Mirman et al. 2022, (NCB in press)
BRCA1-proficient isogenic control	RPE1	{Noordermeer et al., 2018, #102280}
BRCA1 KO	RPE1	{Noordermeer et al., 2018, #102280}
SHLD1 KO	RPE1	Mirman et al. 2022, (NCB in press)
BRCA1/SHLD1 DKO	RPE1	Mirman et al. 2022, (NCB in press)
WDR70-mAID-mClover	RPE1	Mirman et al. 2022, (NCB in press)
FOKI-LACI-mCherry	U2OS	{Tang et al., 2013, #81012}
CH12-F3	murine B	{Ghezraoui et al., 2018, #72272}
CH12-F3 SHLD1 KO	murine B	{Ghezraoui et al., 2018, #72272}

Table 2. Plasmids

Name	Resistance	Reference
pLPC_6myc_mCtc1	Puro	{Mirman et al., 2018, #105071}
pWZL_6myc_mCtc1	Hygro	{Mirman et al., 2018, #105071}
pLPC_HA_Stn1	Puro	{Mirman et al., 2018, #105071}
myc-RPA32	Puro	{Gong et al., 2017, #92289}
53BP1wt	Puro	{Lottersberger et al., 2015, #98324}
53BP1ΔRIF1	Puro	{Lottersberger et al., 2015, #98324}
pLPC_Flag_Pot1a	Puro	{Hockemeyer et al., 2006, #56655}
pLPC_Flag_Pot1b	Puro	{Hockemeyer et al., 2006, #56655}
pLPC-myc-mCtc1	Puro	{Wu et al., 2012, #15448}
pLPC-myc-mStn1	Puro	{Wu et al., 2012, #15448}
pLPC-myc-mTen1	Puro	{Wu et al., 2012, #15448}
pLPC-myc-hCtc1	Puro	{Mirman et al., 2018, #105071}
pLPC-myc-hStn1	Puro	{Mirman et al., 2018, #105071}
pLPC-myc-hTen1	Puro	{Mirman et al., 2018, #105071}
pLPC-myc-hRev7	Puro	{Mirman et al., 2018, #105071}
pLPC_flag_mShld1	Puro	{Mirman et al., 2018, #105071}
pCDNA5-FLAG-hSHLD1	Puro	{Mirman et al., 2018, #105071}
pCDNA5-FLAG-hSHLD1ΔLDLP	Puro	Mirman et al., 2022 (NCB in press)
pLPC-myc-SHLD2C	Puro	Mirman et al., 2022 (NCB in press)
pQC-SNAP-hSHLD1	Neo	Mirman et al., 2022 (NCB in press)
pQC-SNAP-hSHLD1ΔLDLP	Neo	Mirman et al., 2022 (NCB in press)
pLPC-HALO-hCTC1	Puro	Mirman et al., 2022 (NCB in press)
pWZL-GFP-FHA-mSTN1	Hygro	Mirman et al., 2022 (NCB in press)
pWZL-GFP-mFHA-mSHLD1	Hygro	Mirman et al., 2022 (NCB in press)
pWZL-GFP-mFHAR61Q-mSHLD1	Hygro	Mirman et al., 2022 (NCB in press)
pWZL-GFP-mFHA-mSHLD1ΔLDLP	Hygro	Mirman et al., 2022 (NCB in press)
pQCN_Flag_hSHLD1	Neo	Mirman et al., 2022 (NCB in press)
pQCN_Flag_hSHLD1ΔLDLP	Neo	Mirman et al., 2022 (NCB in press)
pWZL_mShld1	Hygro	Mirman et al., 2022 (NCB in press)
pWZL_mShld1ΔLDLP	Hygro	Mirman et al., 2022 (NCB in press)
pLPC_hWDR70	Puro	Mirman et al. (submitted)
pLPC_hWDR70_WDAA	Puro	Mirman et al. (submitted)

Table 3. Target sequences

Gene	RNAi or CRISPR	Target
Stn1 #1	RNAi	GATCCTGTGTTTCTAGCCTTT
Stn1 #2	RNAi	GCTGTCATCAGCGTGAAAGAA
Ctc1	RNAi	CGGCAGATCACAGCATGATAA
ATR #1	RNAi	CTGTGGTTGTATCTGTTCAAT
ATR #2	RNAi	GATGAACACATGGGATATTTA
53bp1 #2	CRISPR	GAGAATCTTCTATTATC-(PAM)
53bp1 #3	CRISPR	GCATCTGCAGATTAGGA-(PAM)
Rev7 #2	CRISPR	GTGTCCCCACCACAGTGG-(PAM)
Rev7 #3	CRISPR	GCCGGTTCAGGTGAGCCC-(PAM)
Shld2	CRISPR	ATCAGTCAGATCCCTGCGTT-(PAM)
53BP1 #1	CRISPR	CAGAATCATCCTCTAGAACC-(PAM)
53BP1 #2	CRISPR	TTGATCTCACTTGTGATTCG-(PAM)
SHLD2 #1	CRISPR	TCTGGAGAACCAATAGATTC-(PAM)
SHLD2 #2	CRISPR	TTTGAGCTAAAAAAGCAACC-(PAM)
REV7 #1	CRISPR	CCTCAACTTTGGCCAAGGTA-(PAM)
REV7 #2	CRISPR	TATACTGATTCAGCTCCGGG-(PAM)
Shld2	CRISPR	ATCAGTCAGATCCCTGCGTTCGG-(PAM)
Shld1	CRISPR	CTGTACCTTGGATCTACCCG-(PAM)
SHLD1	CRISPR	TCTCTTATGTCACACGCTGA-(PAM)
BRCA1	CRISPR	GGCTCAGGGTTACCGAAGAG-(PAM)
BRCA2 #1	CRISPR	GCAGGTTCAGAATTATAGGG-(PAM)
BRCA2 #2	CRISPR	GTCTACCTGACCAATCGATG-(PAM)
Brca1	CRISPR	GTATGCCAGAGAAAGCGGAG-(PAM)
WDR70 Cterm deg 1	CRISPR	TGAGAGCTGTTTGCATGAGT-(PAM)
WDR70 Cterm deg 2	CRISPR	TTGAGAGCTGTTTGCATGAG-(PAM)
DDB1 #1	CRISPR	GGATAGCCATCTGAATTGAG-(PAM)
DDB1 #4	CRISPR	GCGGCACGTAAAAACCTATG-(PAM)

Table 4. Drugs and chemicals

Name	Number	Provider	Dose (unless otherwise stated)
ATMi	KU55933	Selleck	10 μM
ATRi	ETP-46464	Sigma	2.5 mM
Olaparib	AZD2281	Selleck	0.5-10 μM
CDKi	RO-3306	Sigma	9 μM
Polαi	CD437	Sigma	10 μM
Aphidicolin	A0781	Sigma	2.5 μM
Doxycycline	D9891	Sigma	2 μg/ml
IAA (auxin)	ab146402	Abcam	500 μM
Vidarabine Triphposphate	3714-60-1	Jena	10 μM
BrdU	B5002	Sigma	10 μM
Zeocin	R25001	Invitrogen	100μg/ml
HaXS8	4991	Tocris	0.5 μM
NAEi	MLN4942	Sigma	various
Cycloheximide	2112	Cell Signaling	50 μg/ml

Table 5. Antibodies

Gene	Company	Catalog	IF/WB/IP
53BP1	Abcam	ab175933	IF/WB
53BP1	NovusBio	NB100-304	IF/WB
Artemis	CellSignallingTechnologies	13381	WB
ASTE1	NovusBio	NBP1-8166 1	WB
ATM	NovusBio	nb100-104	WB
ATR	SantaCruz	sc-1887	WB
BARD1	SantaCruz	sc11438	IF/WB
BLM	Abcam	ab2179	WB
BRCA1	RD	mab22101	IF/WB
BRCA2	CellSignallingTechnologies	10741	WB
BRCA2	Millipore	OP95	WB
CCDC98	Abcam	ab139191	WB
Chk1	SantaCruz	sc-8408	WB
Chk1-P(Ser317)	CellSignallingTechnologies	2344	WB
Chk1-S345-P	CellSignallingTechnologies	2341S	WB
Chk2	BDBiosciences	611570	WB
CTC1	de Lange Lab	not published; JCZ	WB
CTC1	Millipore	MABE1103	WB
CUL4A	CellSignallingTechnologies	2699	WB
DDB1	Abcam	ab109027	WB
DNAPKcs	CellSignallingTechnologies	38168	WB
DNAPKcs-P(Ser2056)	CellSignallingTechnologies	68716	WB
Exo1	Abcam	ab95068	WB
Flag tag	Sigma	M2-F1804	IF/WB/IP
g-tubulin	Abcam	ab1136	WB
GAPDH	ThermoFisher	MA5-15738	WB
GFP	ProteinTech	50430-2-AP	WB
GFP	Sigma	11814460001	WB
gH2AX	Bethyl	A300-081A	IF/WB
gH2AX	Millipore	5636	IF/WB
HA	CellSignallingTechnologies	3724	IF/WB
HALO tag	Promega	G9211	WB
Histone 2B	Abcam	ab1790	WB
Histone 2B Ub K120	CellSignallingTechnologies	5546T	WB

Hsp70	BDBiosciences	610608	WB
Ku70	CellSignallingTechnologies	4588	WB
Ku80	CellSignallingTechnologies	2180	WB
Lamin a/c	SantaCruz	sc-6215	IF
Lig3	BDBiosciences	611876	WB
Lig4	CellSignallingTechnologies	14649	WB
MCM7	SantaCruz	sc9966	WB
MDC1	CalbioChem	DR1018	WB
Myc tag	CellSignallingTechnologies	9B11	WB/IP
Myc tag	CellSignallingTechnologies	71D10	IF
PALB2	CellSignallingTechnologies	E9R2W	WB
PARP1	Enzo	BML-SA249-0050	WB
PCNA	SantaCruz	sc7907	WB
PolQ	Abcam	ab80906	WB
PRIM1	ProteinTech	107731_AP	WB
Rad51	Bioacademia	70-001	IF/WB
RAP80	Bethyl	A300-764A	WB
REV7	Abcam	ab180579	WB
REV7	BDBiosciences	612266	WB
RIF1 #1060	de Lange Lab	Silverman et al 2004	IF/WB
RIF1 #1240	de Lange Lab	Buonomo?	IF/WB
RNF168	Abcam	ab103491	WB
RNF20	Abcam	ab32629	WB
RNF8	Abcam	ab105362	WB
RPA32	Bethyl	A300-244A	IF/WB
RPA32-P(S4/S8)	Bethyl	A300-245A	IF/WB
SCC3	Abcam	ab4457	WB
SHLD1	ThermoFisher	PA5-59280	WB
SHLD1	Chapman Lab; Eurogentec	not published	WB/IP
SHLD2	NovusBio	NBP1-88980	WB
SHLD2	Chapman Lab; Eurogentec	not published	WB/IP
SMC1	Abcam	ab9262	WB
SMC3	Abcam	ab9263	WB
SNAP tag	NEB	9310	IF/WB/IP
STN1	SantaCruz	sc-376450	IF/WB
STN1	Abcam	89250	WB
TRF2	de Lange Lab	1254	WB

WDR70	SantaCruz	sc-398268	WB
WDR70	Bethyl	A-301-871A	IF
WRN	Abcam	ab124673	WB
XLF	CellSignallingTechnologies	2854	WB
XRCC1	Abcam	ab134056	WB

LITERATURE CITED

1. Iwabuchi, K., Bartel, P. L., Li, B., Marraccino, R. & Fields, S. Two cellular proteins that bind to wild-type but not mutant p53. *Proc Natl Acad Sci U S A* **91**, 6098-6102 (1994).
2. Zimmermann, M. & de Lange, T. 53BP1: pro choice in DNA repair. *Trends Cell Biol* **24**, 108-117 (2014).
3. Panier, S. & Boulton, S. J. Double-strand break repair: 53BP1 comes into focus. *Nat Rev Mol Cell Biol* **15**, 7-18 (2014).
4. Hustedt, N. & Durocher, D. The control of DNA repair by the cell cycle. *Nat Cell Biol* **19**, 1-9 (2016).
5. Symington, L. S. & Gautier, J. Double-strand break end resection and repair pathway choice. *Annu Rev Genet* **45**, 247-271 (2011).
6. Pannunzio, N. R., Watanabe, G. & Lieber, M. R. Nonhomologous DNA end-joining for repair of DNA double-strand breaks. *J Biol Chem* **293**, 10512-10523 (2018).
7. Soutoglou, E. et al. Positional stability of single double-strand breaks in mammalian cells. *Nat Cell Biol* **9**, 675-682 (2007).
8. Agarwal, S. et al. Isolation, characterization, and genetic complementation of a cellular mutant resistant to retroviral infection. *Proc Natl Acad Sci U S A* **103**, 15933-15938 (2006).
9. Grundy, G. J. et al. The Ku-binding motif is a conserved module for recruitment and stimulation of non-homologous end-joining proteins. *Nat Commun* **7**, 11242 (2016).
10. Arnoult, N. et al. Regulation of DNA repair pathway choice in S and G2 phases by the NHEJ inhibitor CYREN. *Nature* **549**, 548-552 (2017).
11. Hung, P. J. et al. MRI Is a DNA Damage Response Adaptor during Classical Non-homologous End Joining. *Mol Cell* **71**, 332-342.e8 (2018).
12. Wright, W. D., Shah, S. S. & Heyer, W. D. Homologous recombination and the repair of DNA double-strand breaks. *J Biol Chem* **293**, 10524-10535 (2018).
13. Roy, R., Chun, J. & Powell, S. N. BRCA1 and BRCA2: different roles in a common pathway of genome protection. *Nat Rev Cancer* **12**, 68-78 (2011).
14. Sartori, A. A. et al. Human CtIP promotes DNA end resection. *Nature* **450**, 509-514 (2007).
15. Garcia, V., Phelps, S. E., Gray, S. & Neale, M. J. Bidirectional resection of DNA double-strand breaks by Mre11 and Exo1. *Nature* **479**, 241-244 (2011).
16. Deshpande, R. A., Lee, J. H., Arora, S. & Paull, T. T. Nbs1 Converts the Human Mre11/Rad50 Nuclease Complex into an Endo/Exonuclease Machine Specific for Protein-DNA Adducts. *Mol Cell* **64**, 593-606 (2016).
17. Anand, R., Ranjha, L., Cannavo, E. & Cejka, P. Phosphorylated CtIP Functions as a Co-factor of the MRE11-RAD50-NBS1 Endonuclease in DNA End Resection. *Mol Cell* **64**, 940-950 (2016).
18. Anand, R. et al. NBS1 promotes the endonuclease activity of the MRE11-RAD50 complex by sensing CtIP phosphorylation. *EMBO J* **38**, (2019).
19. Myler, L. R. et al. Single-Molecule Imaging Reveals How Mre11-Rad50-Nbs1 Initiates DNA Break Repair. *Mol Cell* **67**, 891-898.e4 (2017).

20. Nimonkar, A. V. et al. BLM-DNA2-RPA-MRN and EXO1-BLM-RPA-MRN constitute two DNA end resection machineries for human DNA break repair. *Genes Dev* **25**, 350-362 (2011).
21. Moynahan, M. E., Pierce, A. J. & Jasin, M. BRCA2 is required for homology-directed repair of chromosomal breaks. *Mol Cell* **7**, 263-272 (2001).
22. Davies, A. A. et al. Role of BRCA2 in control of the RAD51 recombination and DNA repair protein. *Mol Cell* **7**, 273-282 (2001).
23. West, S. C. et al. Resolution of Recombination Intermediates: Mechanisms and Regulation. *Cold Spring Harb Symp Quant Biol* **80**, 103-109 (2015).
24. Sfeir, A. & Symington, L. S. Microhomology-Mediated End Joining: A Back-up Survival Mechanism or Dedicated Pathway. *Trends Biochem Sci* **40**, 701-714 (2015).
25. Bunting, S. F. et al. 53BP1 inhibits homologous recombination in Brca1-deficient cells by blocking resection of DNA breaks. *Cell* **141**, 243-254 (2010).
26. Bouwman, P. et al. 53BP1 loss rescues BRCA1 deficiency and is associated with triple-negative and BRCA-mutated breast cancers. *Nat Struct Mol Biol* **17**, 688-695 (2010).
27. Zimmermann, M., Lottersberger, F., Buonomo, S. B., Sfeir, A. & de Lange, T. 53BP1 regulates DSB repair using Rif1 to control 5' end resection. *Science* **339**, 700-704 (2013).
28. Di Virgilio, M. et al. Rif1 prevents resection of DNA breaks and promotes immunoglobulin class switching. *Science* **339**, 711-715 (2013).
29. Difilippantonio, S. et al. 53BP1 facilitates long-range DNA end-joining during V(D)J recombination. *Nature* **456**, 529-533 (2008).
30. Lottersberger, F., Bothmer, A., Robbiani, D. F., Nussenzweig, M. C. & de Lange, T. Role of 53BP1 oligomerization in regulating double-strand break repair. *Proc Natl Acad Sci U S A* **110**, 2146-2151 (2013).
31. Morales, J. C. et al. Role for the BRCA1 C-terminal repeats (BRCT) protein 53BP1 in maintaining genomic stability. *J Biol Chem* **278**, 14971-14977 (2003).
32. Xu, Y. et al. 53BP1 and BRCA1 control pathway choice for stalled replication restart. *Elife* **6**, (2017).
33. Noon, A. T. et al. 53BP1-dependent robust localized KAP-1 phosphorylation is essential for heterochromatic DNA double-strand break repair. *Nat Cell Biol* **12**, 177-184 (2010).
34. Ward, I. M. et al. 53BP1 is required for class switch recombination. *J Cell Biol* **165**, 459-464 (2004).
35. Mirman, Z. et al. 53BP1-RIF1-shieldin counteracts DSB resection through CST- and Polα-dependent fill-in. *Nature* **560**, 112-116 (2018).
36. Panier, S. & Durocher, D. Push back to respond better: regulatory inhibition of the DNA double-strand break response. *Nat Rev Mol Cell Biol* **14**, 661-672 (2013).
37. Shang, Y. L., Bodero, A. J. & Chen, P. L. NFBD1, a novel nuclear protein with signature motifs of FHA and BRCT, and an internal 41-amino acid repeat sequence, is an early participant in DNA damage response. *J Biol Chem* **278**, 6323-6329 (2003).

38. Lou, Z., Minter-Dykhouse, K., Wu, X. & Chen, J. MDC1 is coupled to activated CHK2 in mammalian DNA damage response pathways. *Nature* **421**, 957-961 (2003).
39. Kolas, N. K. et al. Orchestration of the DNA-damage response by the RNF8 ubiquitin ligase. *Science* **318**, 1637-1640 (2007).
40. Huen, M. S. et al. RNF8 transduces the DNA-damage signal via histone ubiquitylation and checkpoint protein assembly. *Cell* **131**, 901-914 (2007).
41. Mailand, N. et al. RNF8 ubiquitylates histones at DNA double-strand breaks and promotes assembly of repair proteins. *Cell* **131**, 887-900 (2007).
42. Doil, C. et al. RNF168 binds and amplifies ubiquitin conjugates on damaged chromosomes to allow accumulation of repair proteins. *Cell* **136**, 435-446 (2009).
43. Stewart, G. S. et al. The RIDDLE syndrome protein mediates a ubiquitin-dependent signaling cascade at sites of DNA damage. *Cell* **136**, 420-434 (2009).
44. Mattiroli, F. et al. RNF168 ubiquitinates K13-15 on H2A/H2AX to drive DNA damage signaling. *Cell* **150**, 1182-1195 (2012).
45. Fradet-Turcotte, A. et al. 53BP1 is a reader of the DNA-damage-induced H2A Lys 15 ubiquitin mark. *Nature* **499**, 50-54 (2013).
46. Botuyan, M. V. et al. Structural basis for the methylation state-specific recognition of histone H4-K20 by 53BP1 and Crb2 in DNA repair. *Cell* **127**, 1361-1373 (2006).
47. Zhang, A., Peng, B., Huang, P., Chen, J. & Gong, Z. The p53-binding protein 1-Tudor-interacting repair regulator complex participates in the DNA damage response. *J Biol Chem* **292**, 6461-6467 (2017).
48. Drané, P. et al. TIRR regulates 53BP1 by masking its histone methyl-lysine binding function. *Nature* **543**, 211-216 (2017).
49. Botuyan, M. V. et al. Mechanism of 53BP1 activity regulation by RNA-binding TIRR and a designer protein. *Nat Struct Mol Biol* **25**, 591-600 (2018).
50. Dai, Y., Zhang, A., Shan, S., Gong, Z. & Zhou, Z. Structural basis for recognition of 53BP1 tandem Tudor domain by TIRR. *Nat Commun* **9**, 2123 (2018).
51. Adams, M. M. et al. 53BP1 oligomerization is independent of its methylation by PRMT1. *Cell Cycle* **4**, 1854-1861 (2005).
52. Ward, I. et al. The tandem BRCT domain of 53BP1 is not required for its repair function. *J Biol Chem* **281**, 38472-38477 (2006).
53. Zgheib, O., Pataky, K., Brugger, J. & Halazonetis, T. D. An oligomerized 53BP1 tudor domain suffices for recognition of DNA double-strand breaks. *Mol Cell Biol* **29**, 1050-1058 (2009).
54. Bothmer, A. et al. Regulation of DNA end joining, resection, and immunoglobulin class switch recombination by 53BP1. *Mol Cell* **42**, 319-329 (2011).
55. Kilic, S. et al. Phase separation of 53BP1 determines liquid-like behavior of DNA repair compartments. *EMBO J* **38**, e101379 (2019).
56. He, Y. J. et al. DYNLL1 binds to MRE11 to limit DNA end resection in BRCA1-deficient cells. *Nature* **563**, 522-526 (2018).
57. Becker, J. R. et al. The ASCIZ-DYNLL1 axis promotes 53BP1-dependent non-homologous end joining and PARP inhibitor sensitivity. *Nat Commun* **9**, 5406 (2018).
58. Joo, W. S. et al. Structure of the 53BP1 BRCT region bound to p53 and its comparison to the Brca1 BRCT structure. *Genes Dev* **16**, 583-593 (2002).

59. Derbyshire, D. J. et al. Crystal structure of human 53BP1 BRCT domains bound to p53 tumour suppressor. *EMBO J* **21**, 3863-3872 (2002).
60. Cuella-Martin, R. et al. 53BP1 Integrates DNA Repair and p53-Dependent Cell Fate Decisions via Distinct Mechanisms. *Mol Cell* **64**, 51-64 (2016).
61. Kleiner, R. E., Verma, P., Molloy, K. R., Chait, B. T. & Kapoor, T. M. Chemical proteomics reveals a γH2AX-53BP1 interaction in the DNA damage response. *Nat Chem Biol* **11**, 807-814 (2015).
62. Saldivar, J. C., Cortez, D. & Cimprich, K. A. The essential kinase ATR: ensuring faithful duplication of a challenging genome. *Nat Rev Mol Cell Biol* **18**, 622-636 (2017).
63. Denchi, E. L. & de Lange, T. Protection of telomeres through independent control of ATM and ATR by TRF2 and POT1. *Nature* **448**, 1068-1071 (2007).
64. Dimitrova, N., Chen, Y. C., Spector, D. L. & de Lange, T. 53BP1 promotes non-homologous end joining of telomeres by increasing chromatin mobility. *Nature* **456**, 524-528 (2008).
65. de Lange, T. Shelterin-Mediated Telomere Protection. *Annu Rev Genet* **52**, 223-247 (2018).
66. Celli, G. B. & de Lange, T. DNA processing is not required for ATM-mediated telomere damage response after TRF2 deletion. *Nat Cell Biol* **7**, 712-718 (2005).
67. Dimitrova, N. & de Lange, T. Cell cycle-dependent role of MRN at dysfunctional telomeres: ATM signaling-dependent induction of nonhomologous end joining (NHEJ) in G1 and resection-mediated inhibition of NHEJ in G2. *Mol Cell Biol* **29**, 5552-5563 (2009).
68. Attwooll, C. L., Akpinar, M. & Petrini, J. H. The mre11 complex and the response to dysfunctional telomeres. *Mol Cell Biol* **29**, 5540-5551 (2009).
69. Deng, Y., Guo, X., Ferguson, D. O. & Chang, S. Multiple roles for MRE11 at uncapped telomeres. *Nature* **460**, 914-918 (2009).
70. Smogorzewska, A., Karlseder, J., Holtgreve-Grez, H., Jauch, A. & de Lange, T. DNA ligase IV-dependent NHEJ of deprotected mammalian telomeres in G1 and G2. *Curr Biol* **12**, 1635-1644 (2002).
71. Griffith, J. D. et al. Mammalian telomeres end in a large duplex loop. *Cell* **97**, 503-514 (1999).
72. Doksani, Y., Wu, J. Y., de Lange, T. & Zhuang, X. Super-resolution fluorescence imaging of telomeres reveals TRF2-dependent T-loop formation. *Cell* **155**, 345-356 (2013).
73. Dimitrova, N. & de Lange, T. MDC1 accelerates nonhomologous end-joining of dysfunctional telomeres. *Genes Dev* **20**, 3238-3243 (2006).
74. Peuscher, M. H. & Jacobs, J. J. DNA-damage response and repair activities at uncapped telomeres depend on RNF8. *Nat Cell Biol* **13**, 1139-1145 (2011).
75. Lottersberger, F., Karssemeijer, R. A., Dimitrova, N. & de Lange, T. 53BP1 and the LINC Complex Promote Microtubule-Dependent DSB Mobility and DNA Repair. *Cell* **163**, 880-893 (2015).
76. Timashev, L. A., Babcock, H., Zhuang, X. & de Lange, T. The DDR at telomeres lacking intact shelterin does not require substantial chromatin decompaction. *Genes Dev* **31**, 578-589 (2017).

77. Aten, J. A. et al. Dynamics of DNA double-strand breaks revealed by clustering of damaged chromosome domains. *Science* **303**, 92-95 (2004).
78. Celli, G. B., Denchi, E. L. & de Lange, T. Ku70 stimulates fusion of dysfunctional telomeres yet protects chromosome ends from homologous recombination. *Nat Cell Biol* **8**, 885-890 (2006).
79. van Steensel, B., Smogorzewska, A. & de Lange, T. TRF2 protects human telomeres from end-to-end fusions. *Cell* **92**, 401-413 (1998).
80. Zhu, X. D. et al. ERCC1/XPF removes the 3' overhang from uncapped telomeres and represses formation of telomeric DNA-containing double minute chromosomes. *Mol Cell* **12**, 1489-1498 (2003).
81. Lam, Y. C. et al. SNMIB/Apollo protects leading-strand telomeres against NHEJ-mediated repair. *EMBO J* **29**, 2230-2241 (2010).
82. Wu, P., van Overbeek, M., Rooney, S. & de Lange, T. Apollo contributes to G overhang maintenance and protects leading-end telomeres. *Mol Cell* **39**, 606-617 (2010).
83. Wu, P., Takai, H. & de Lange, T. Telomeric 3' overhangs derive from resection by Exo1 and Apollo and fill-in by POT1b-associated CST. *Cell* **150**, 39-52 (2012).
84. Takai, H. et al. A POT1 mutation implicates defective telomere end fill-in and telomere truncations in Coats plus. *Genes Dev* **30**, 812-826 (2016).
85. Surovtseva, Y. V. et al. Conserved telomere maintenance component 1 interacts with STN1 and maintains chromosome ends in higher eukaryotes. *Mol Cell* **36**, 207-218 (2009).
86. Price, C. M. et al. Evolution of CST function in telomere maintenance. *Cell Cycle* **9**, 3157-3165 (2010).
87. Boersma, V. et al. MAD2L2 controls DNA repair at telomeres and DNA breaks by inhibiting 5' end resection. *Nature* **521**, 537-540 (2015).
88. Xu, G. et al. REV7 counteracts DNA double-strand break resection and affects PARP inhibition. *Nature* **521**, 541-544 (2015).
89. Gupta, R. et al. DNA Repair Network Analysis Reveals Shieldin as a Key Regulator of NHEJ and PARP Inhibitor Sensitivity. *Cell* **173**, 972-988.e23 (2018).
90. Barazas, M. et al. The CST Complex Mediates End Protection at Double-Strand Breaks and Promotes PARP Inhibitor Sensitivity in BRCA1-Deficient Cells. *Cell Rep* **23**, 2107-2118 (2018).
91. Noordermeer, S. M. et al. The shieldin complex mediates 53BP1-dependent DNA repair. *Nature* **560**, 117-121 (2018).
92. Dev, H. et al. Shieldin complex promotes DNA end-joining and counters homologous recombination in BRCA1-null cells. *Nat Cell Biol* **20**, 954-965 (2018).
93. Chen, L. Y., Redon, S. & Lingner, J. The human CST complex is a terminator of telomerase activity. *Nature* **488**, 540-544 (2012).
94. Hockemeyer, D. & Collins, K. Control of telomerase action at human telomeres. *Nat Struct Mol Biol* **22**, 848-852 (2015).
95. Methot, S. P. & Di Noia, J. M. Molecular Mechanisms of Somatic Hypermutation and Class Switch Recombination. *Adv Immunol* **133**, 37-87 (2017).
96. Basu, U. et al. The RNA exosome targets the AID cytidine deaminase to both strands of transcribed duplex DNA substrates. *Cell* **144**, 353-363 (2011).

97. Bregenhorn, S., Kallenberger, L., Artola-Borán, M., Peña-Diaz, J. & Jiricny, J. Non-canonical uracil processing in DNA gives rise to double-strand breaks and deletions: relevance to class switch recombination. *Nucleic Acids Res* **44**, 2691-2705 (2016).
98. Petersen, S. et al. AID is required to initiate Nbs1/gamma-H2AX focus formation and mutations at sites of class switching. *Nature* **414**, 660-665 (2001).
99. Franco, S. et al. H2AX prevents DNA breaks from progressing to chromosome breaks and translocations. *Mol Cell* **21**, 201-214 (2006).
100. Reina-San-Martin, B., Chen, J., Nussenzweig, A. & Nussenzweig, M. C. Enhanced intra-switch region recombination during immunoglobulin class switch recombination in 53BP1-/- B cells. *Eur J Immunol* **37**, 235-239 (2007).
101. Bothmer, A. et al. 53BP1 regulates DNA resection and the choice between classical and alternative end joining during class switch recombination. *J Exp Med* **207**, 855-865 (2010).
102. Sundaravinayagam, D. et al. 53BP1 Supports Immunoglobulin Class Switch Recombination Independently of Its DNA Double-Strand Break End Protection Function. *Cell Rep* **28**, 1389-1399.e6 (2019).
103. Escribano-Díaz, C. et al. A cell cycle-dependent regulatory circuit composed of 53BP1-RIF1 and BRCA1-CtIP controls DNA repair pathway choice. *Mol Cell* **49**, 872-883 (2013).
104. Chapman, J. R. et al. RIF1 is essential for 53BP1-dependent nonhomologous end joining and suppression of DNA double-strand break resection. *Mol Cell* **49**, 858-871 (2013).
105. Ghezraoui, H. et al. 53BP1 cooperation with the REV7-shieldin complex underpins DNA structure-specific NHEJ. *Nature* **560**, 122-127 (2018).
106. Ray Chaudhuri, A. et al. Replication fork stability confers chemoresistance in BRCA-deficient cells. *Nature* **535**, 382-387 (2016).
107. Farmer, H. et al. Targeting the DNA repair defect in BRCA mutant cells as a therapeutic strategy. *Nature* **434**, 917-921 (2005).
108. Bryant, H. E. et al. Specific killing of BRCA2-deficient tumours with inhibitors of poly(ADP-ribose) polymerase. *Nature* **434**, 913-917 (2005).
109. Fong, P. C. et al. Inhibition of poly(ADP-ribose) polymerase in tumors from BRCA mutation carriers. *N Engl J Med* **361**, 123-134 (2009).
110. Tutt, A. et al. Oral poly(ADP-ribose) polymerase inhibitor olaparib in patients with BRCA1 or BRCA2 mutations and advanced breast cancer: a proof-of-concept trial. *Lancet* **376**, 235-244 (2010).
111. Pilié, P. G., Gay, C. M., Byers, L. A., O'Connor, M. J. & Yap, T. A. PARP Inhibitors: Extending Benefit Beyond BRCA-Mutant Cancers. *Clin Cancer Res* **25**, 3759-3771 (2019).
112. Barnes, D. E. & Lindahl, T. Repair and genetic consequences of endogenous DNA base damage in mammalian cells. *Annu Rev Genet* **38**, 445-476 (2004).
113. Ray Chaudhuri, A. & Nussenzweig, A. The multifaceted roles of PARP1 in DNA repair and chromatin remodelling. *Nat Rev Mol Cell Biol* **18**, 610-621 (2017).
114. Zimmermann, M. et al. CRISPR screens identify genomic ribonucleotides as a source of PARP-trapping lesions. *Nature* **559**, 285-289 (2018).

115. Pommier, Y., O'Connor, M. J. & de Bono, J. Laying a trap to kill cancer cells: PARP inhibitors and their mechanisms of action. *Sci Transl Med* **8**, 362ps17 (2016).
116. Taylor, M. R. G. & Yeeles, J. T. P. The Initial Response of a Eukaryotic Replisome to DNA Damage. *Mol Cell* **70**, 1067-1080.e12 (2018).
117. Oostra, A. B., Nieuwint, A. W., Joenje, H. & de Winter, J. P. Diagnosis of fanconi anemia: chromosomal breakage analysis. *Anemia* **2012**, 238731 (2012).
118. Schoonen, P. M. et al. Progression through mitosis promotes PARP inhibitor-induced cytotoxicity in homologous recombination-deficient cancer cells. *Nat Commun* **8**, 15981 (2017).
119. Feng, L., Fong, K. W., Wang, J., Wang, W. & Chen, J. RIF1 counteracts BRCA1-mediated end resection during DNA repair. *J Biol Chem* **288**, 11135-11143 (2013).
120. Gao, S. et al. An OB-fold complex controls the repair pathways for DNA double-strand breaks. *Nat Commun* **9**, 3925 (2018).
121. Callen, E. et al. 53BP1 mediates productive and mutagenic DNA repair through distinct phosphoprotein interactions. *Cell* **153**, 1266-1280 (2013).
122. Wang, J. et al. PTIP associates with Artemis to dictate DNA repair pathway choice. *Genes Dev* **28**, 2693-2698 (2014).
123. Callen, E. et al. 53BP1 Enforces Distinct Pre- and Post-resection Blocks on Homologous Recombination. *Mol Cell* **77**, 26-38.e7 (2020).
124. Schlacher, K. et al. Double-strand break repair-independent role for BRCA2 in blocking stalled replication fork degradation by MRE11. *Cell* **145**, 529-542 (2011).
125. Schlacher, K., Wu, H. & Jasin, M. A distinct replication fork protection pathway connects Fanconi anemia tumor suppressors to RAD51-BRCA1/2. *Cancer Cell* **22**, 106-116 (2012).
126. Taglialatela, A. et al. Restoration of Replication Fork Stability in BRCA1- and BRCA2-Deficient Cells by Inactivation of SNF2-Family Fork Remodelers. *Mol Cell* **68**, 414-430.e8 (2017).
127. Rickman, K. & Smogorzewska, A. Advances in understanding DNA processing and protection at stalled replication forks. *J Cell Biol* **218**, 1096-1107 (2019).
128. Saredi, G. et al. H4K20me0 marks post-replicative chromatin and recruits the TONSL–MMS22L DNA repair complex. *Nature* **534**, 714-718 (2016).
129. Nakamura, K. et al. H4K20me0 recognition by BRCA1-BARD1 directs homologous recombination to sister chromatids. *Nat Cell Biol* **21**, 311-318 (2019).
130. Simonetta, M. et al. H4K20me2 distinguishes pre-replicative from post-replicative chromatin to appropriately direct DNA repair pathway choice by 53BP1-RIF1-MAD2L2. *Cell Cycle* **17**, 124-136 (2018).
131. Chapman, J. R., Sossick, A. J., Boulton, S. J. & Jackson, S. P. BRCA1-associated exclusion of 53BP1 from DNA damage sites underlies temporal control of DNA repair. *J Cell Sci* **125**, 3529-3534 (2012).
132. Ochs, F. et al. Stabilization of chromatin topology safeguards genome integrity. *Nature* **574**, 571-574 (2019).
133. Barazas, M. et al. Radiosensitivity Is an Acquired Vulnerability of PARPi-Resistant BRCA1-Deficient Tumors. *Cancer Res* **79**, 452-460 (2019).
134. Setiaputra, D. & Durocher, D. Shieldin - the protector of DNA ends. *EMBO Rep* **20**, (2019).

135. Findlay, S. et al. SHLD2/FAM35A co-operates with REV7 to coordinate DNA double-strand break repair pathway choice. *EMBO J* **37**, (2018).
136. Mirman, Z. & de Lange, T. 53BP1: a DSB escort. *Genes Dev* **34**, 7-23 (2020).
137. Nicolette, M. L. et al. Mre11-Rad50-Xrs2 and Sae2 promote 5' strand resection of DNA double-strand breaks. *Nat Struct Mol Biol* **17**, 1478-1485 (2010).
138. Yang, S. H. et al. The SOSS1 single-stranded DNA binding complex promotes DNA end resection in concert with Exo1. *EMBO J* **32**, 126-139 (2013).
139. Gong, Y., Handa, N., Kowalczykowski, S. C. & de Lange, T. PHF11 promotes DSB resection, ATR signaling, and HR. *Genes Dev* **31**, 46-58 (2017).
140. Myler, L. R. et al. Single-molecule imaging reveals the mechanism of Exo1 regulation by single-stranded DNA binding proteins. *Proc Natl Acad Sci U S A* **113**, E1170-9 (2016).
141. Soniat, M. M., Myler, L. R., Kuo, H. C., Paull, T. T. & Finkelstein, I. J. RPA Phosphorylation Inhibits DNA Resection. *Mol Cell* **75**, 145-153.e5 (2019).
142. Kratz, K. & de Lange, T. Protection of telomeres 1 proteins POT1a and POT1b can repress ATR signaling by RPA exclusion, but binding to CST limits ATR repression by POT1b. *J Biol Chem* **293**, 14384-14392 (2018).
143. Zhao, F. et al. ASTE1 promotes shieldin-complex-mediated DNA repair by attenuating end resection. *Nat Cell Biol* **23**, 894-904 (2021).
144. Bhattacharjee, A., Wang, Y., Diao, J. & Price, C. M. Dynamic DNA binding, junction recognition and G4 melting activity underlie the telomeric and genome-wide roles of human CST. *Nucleic Acids Res* **45**, 12311-12324 (2017).
145. Hom, R. A. & Wuttke, D. S. Human CST Prefers G-Rich but Not Necessarily Telomeric Sequences. *Biochemistry* **56**, 4210-4218 (2017).
146. Goulian, M., Heard, C. J. & Grimm, S. L. Purification and properties of an accessory protein for DNA polymerase alpha/primase. *J Biol Chem* **265**, 13221-13230 (1990).
147. Casteel, D. E. et al. A DNA polymerase-{alpha}{middle dot}primase cofactor with homology to replication protein A-32 regulates DNA replication in mammalian cells. *J Biol Chem* **284**, 5807-5818 (2009).
148. Ganduri, S. & Lue, N. F. STN1-POLA2 interaction provides a basis for primase-pol α stimulation by human STN1. *Nucleic Acids Res* **45**, 9455-9466 (2017).
149. Pellegrini, L. The Pol α-primase complex. *Subcell Biochem* **62**, 157-169 (2012).
150. Schimmel, J., Muñoz-Subirana, N., Kool, H., van Schendel, R. & Tijsterman, M. Small tandem DNA duplications result from CST-guided Pol α-primase action at DNA break termini. *Nat Commun* **12**, 4843 (2021).
151. Makarov, V. L., Hirose, Y. & Langmore, J. P. Long G tails at both ends of human chromosomes suggest a C strand degradation mechanism for telomere shortening. *Cell* **88**, 657-666 (1997).
152. Wright, W. E., Tesmer, V. M., Huffman, K. E., Levene, S. D. & Shay, J. W. Normal human chromosomes have long G-rich telomeric overhangs at one end. *Genes Dev* **11**, 2801-2809 (1997).
153. Sfeir, A. J., Chai, W., Shay, J. W. & Wright, W. E. Telomere-end processing the terminal nucleotides of human chromosomes. *Mol Cell* **18**, 131-138 (2005).
154. Orthwein, A. et al. A mechanism for the suppression of homologous recombination in G1 cells. *Nature* **528**, 422-426 (2015).

155. Huertas, P. & Jackson, S. P. Human CtIP mediates cell cycle control of DNA end resection and double strand break repair. *J Biol Chem* **284**, 9558-9565 (2009).
156. Ochs, F. et al. 53BP1 fosters fidelity of homology-directed DNA repair. *Nat Struct Mol Biol* **23**, 714-721 (2016).
157. Pellegrino, S., Michelena, J., Teloni, F., Imhof, R. & Altmeyer, M. Replication-Coupled Dilution of H4K20me2 Guides 53BP1 to Pre-replicative Chromatin. *Cell Rep* **19**, 1819-1831 (2017).
158. Paiano, J. et al. Role of 53BP1 in end protection and DNA synthesis at DNA breaks. *Genes Dev* **Epub ahead of print**, (2021).
159. Lazzerini-Denchi, E. & Sfeir, A. Stop pulling my strings - what telomeres taught us about the DNA damage response. *Nat Rev Mol Cell Biol* **17**, 364-378 (2016).
160. Sfeir, A. & de Lange, T. Removal of shelterin reveals the telomere end-protection problem. *Science* **336**, 593-597 (2012).
161. Kibe, T., Zimmermann, M. & de Lange, T. TPP1 Blocks an ATR-Mediated Resection Mechanism at Telomeres. *Mol Cell* **61**, 236-246 (2016).
162. Gu, P. et al. CTC1 deletion results in defective telomere replication, leading to catastrophic telomere loss and stem cell exhaustion. *EMBO J* **31**, 2309-2321 (2012).
163. Feng, X., Hsu, S. J., Kasbek, C., Chaiken, M. & Price, C. M. CTC1-mediated C-strand fill-in is an essential step in telomere length maintenance. *Nucleic Acids Res* **45**, 4281-4293 (2017).
164. Karlseder, J., Broccoli, D., Dai, Y., Hardy, S. & de Lange, T. p53- and ATM-dependent apoptosis induced by telomeres lacking TRF2. *Science* **283**, 1321-1325 (1999).
165. Hockemeyer, D., Daniels, J. P., Takai, H. & de Lange, T. Recent expansion of the telomeric complex in rodents: Two distinct POT1 proteins protect mouse telomeres. *Cell* **126**, 63-77 (2006).
166. Han, T. et al. The antitumor toxin CD437 is a direct inhibitor of DNA polymerase α. *Nat Chem Biol* **12**, 511-515 (2016).
167. Bhattacharyya, A., Ear, U. S., Koller, B. H., Weichselbaum, R. R. & Bishop, D. K. The breast cancer susceptibility gene BRCA1 is required for subnuclear assembly of Rad51 and survival following treatment with the DNA cross-linking agent cisplatin. *J Biol Chem* **275**, 23899-23903 (2000).
168. Natsume, T., Kiyomitsu, T., Saga, Y. & Kanemaki, M. T. Rapid Protein Depletion in Human Cells by Auxin-Inducible Degron Tagging with Short Homology Donors. *Cell Rep* **15**, 210-218 (2016).
169. Tang, J. et al. Acetylation limits 53BP1 association with damaged chromatin to promote homologous recombination. *Nat Struct Mol Biol* **20**, 317-325 (2013).
170. Holzer, S. et al. Structural Basis for Inhibition of Human Primase by Arabinofuranosyl Nucleoside Analogues Fludarabine and Vidarabine. *ACS Chem Biol* **14**, 1904-1912 (2019).
171. Nakamura, A. et al. Techniques for gamma-H2AX detection. *Methods Enzymol* **409**, 236-250 (2006).
172. Cesare, A. J. et al. Spontaneous occurrence of telomeric DNA damage response in the absence of chromosome fusions. *Nat Struct Mol Biol* **16**, 1244-1251 (2009).

173. Cesare, A. J., Heaphy, C. M. & O'Sullivan, R. J. Visualization of Telomere Integrity and Function In Vitro and In Vivo Using Immunofluorescence Techniques. *Curr Protoc Cytom* **73**, 12.40.1-12.40.31 (2015).
174. Erhart, D. et al. Chemical development of intracellular protein heterodimerizers. *Chem Biol* **20**, 549-557 (2013).
175. Chaudhuri, J. & Alt, F. W. Class-switch recombination: interplay of transcription, DNA deamination and DNA repair. *Nat Rev Immunol* **4**, 541-552 (2004).
176. Anderson, B. H. et al. Mutations in CTC1, encoding conserved telomere maintenance component 1, cause Coats plus. *Nat Genet* **44**, 338-342 (2012).
177. Chang, H. H. Y., Pannunzio, N. R., Adachi, N. & Lieber, M. R. Non-homologous DNA end joining and alternative pathways to double-strand break repair. *Nat Rev Mol Cell Biol* **18**, 495-506 (2017).
178. Baer, R. & Ludwig, T. The BRCA1/BARD1 heterodimer, a tumor suppressor complex with ubiquitin E3 ligase activity. *Curr Opin Genet Dev* **12**, 86-91 (2002).
179. Densham, R. M. et al. Human BRCA1-BARD1 ubiquitin ligase activity counteracts chromatin barriers to DNA resection. *Nat Struct Mol Biol* **23**, 647-655 (2016).
180. Adra, C. N. et al. SMARCAD1, a novel human helicase family-defining member associated with genetic instability: cloning, expression, and mapping to 4q22-q23, a band rich in breakpoints and deletion mutants involved in several human diseases. *Genomics* **69**, 162-173 (2000).
181. Lim, M. et al. A Ubiquitin-Binding Domain that Binds a Structural Fold Distinct from that of Ubiquitin. *Structure* **27**, 1316-1325.e6 (2019).
182. Ding, D. et al. The CUE1 domain of the SNF2-like chromatin remodeler SMARCAD1 mediates its association with KRAB-associated protein 1 (KAP1) and KAP1 target genes. *J Biol Chem* **293**, 2711-2724 (2018).
183. Zeng, M. et al. CRL4(Wdr70) regulates H2B monoubiquitination and facilitates Exo1-dependent resection. *Nat Commun* **7**, 11364 (2016).
184. Jackson, S. & Xiong, Y. CRL4s: the CUL4-RING E3 ubiquitin ligases. *Trends Biochem Sci* **34**, 562-570 (2009).
185. Li, J. M. & Jin, J. CRL Ubiquitin Ligases and DNA Damage Response. *Front Oncol* **2**, 29 (2012).
186. Guo, L. D. et al. [Functional Analysis of DNA Damage Repair Factor WDR70 and Its Mutation in Ovarian Cancer]. *Sichuan Da Xue Xue Bao Yi Xue Ban* **47**, 501-506 (2016).
187. Lord, C. J., McDonald, S., Swift, S., Turner, N. C. & Ashworth, A. A high-throughput RNA interference screen for DNA repair determinants of PARP inhibitor sensitivity. *DNA Repair (Amst)* **7**, 2010-2019 (2008).
188. Weber, M. et al. A mutation in the essential and widely conserved DAMAGED DNA BINDING1-Cullin4 ASSOCIATED FACTOR gene OZS3 causes hypersensitivity to zinc excess, cold and UV stress in Arabidopsis thaliana. *Plant J* **103**, 995-1009 (2020).
189. He, Y. J., McCall, C. M., Hu, J., Zeng, Y. & Xiong, Y. DDB1 functions as a linker to recruit receptor WD40 proteins to CUL4-ROC1 ubiquitin ligases. *Genes Dev* **20**, 2949-2954 (2006).
190. Soucy, T. A. et al. An inhibitor of NEDD8-activating enzyme as a new approach to treat cancer. *Nature* **458**, 732-736 (2009).

191. Zeng, M., Tang, Z., Guo, L., Wang, X. & Liu, C. Wdr70 regulates histone modification and genomic maintenance in fission yeast. *Biochim Biophys Acta Mol Cell Res* **1867**, 118665 (2020).
192. Nakamura, K. et al. Regulation of homologous recombination by RNF20-dependent H2B ubiquitination. *Mol Cell* **41**, 515-528 (2011).
193. Moyal, L. et al. Requirement of ATM-dependent monoubiquitylation of histone H2B for timely repair of DNA double-strand breaks. *Mol Cell* **41**, 529-542 (2011).
194. Ren, L. et al. The Antiresection Activity of the X Protein Encoded by Hepatitis Virus B. *Hepatology* **69**, 2546-2561 (2019).
195. Litovchick, L. et al. Evolutionarily conserved multisubunit RBL2/p130 and E2F4 protein complex represses human cell cycle-dependent genes in quiescence. *Mol Cell* **26**, 539-551 (2007).
196. Engeland, K. Cell cycle arrest through indirect transcriptional repression by p53: I have a DREAM. *Cell Death Differ* **25**, 114-132 (2018).
197. Fischer, M., Steiner, L. & Engeland, K. The transcription factor p53: not a repressor, solely an activator. *Cell Cycle* **13**, 3037-3058 (2014).
198. Chen, B. R. et al. LIN37-DREAM prevents DNA end resection and homologous recombination at DNA double-strand breaks in quiescent cells. *Elife* **10**, e68466 (2021).
199. Somyajit, K. et al. Homology-directed repair protects the replicating genome from metabolic assaults. *Dev Cell* **56**, 461-477.e7 (2021).
200. Bindra, R. S. et al. Down-regulation of Rad51 and decreased homologous recombination in hypoxic cancer cells. *Mol Cell Biol* **24**, 8504-8518 (2004).
201. Chan, N. et al. Chronic hypoxia decreases synthesis of homologous recombination proteins to offset chemoresistance and radioresistance. *Cancer Res* **68**, 605-614 (2008).
202. Bertram, K. et al. Structural Insights into the Roles of Metazoan-Specific Splicing Factors in the Human Step 1 Spliceosome. *Mol Cell* **80**, 127-139.e6 (2020).
203. Giunta, S., Belotserkovskaya, R. & Jackson, S. P. DNA damage signaling in response to double-strand breaks during mitosis. *J Cell Biol* **190**, 197-207 (2010).
204. Cong, K. et al. Replication gaps are a key determinant of PARP inhibitor synthetic lethality with BRCA deficiency. *Mol Cell* **81**, 3227 (2021).
205. Cantor, S. B. Revisiting the BRCA-pathway through the lens of replication gap suppression: “Gaps determine therapy response in BRCA mutant cancer”. *DNA Repair (Amst)* **107**, 103209 (2021).
206. Yang, Z., Maciejowski, J. & de Lange, T. Nuclear Envelope Rupture Is Enhanced by Loss of p53 or Rb. *Mol Cancer Res* **15**, 1579-1586 (2017).
207. Mirzoeva, O. K. & Petrini, J. H. DNA damage-dependent nuclear dynamics of the Mre11 complex. *Mol Cell Biol* **21**, 281-288 (2001).
208. Cesare, A. J., Hayashi, M. T., Crabbe, L. & Karlseder, J. The telomere deprotection response is functionally distinct from the genomic DNA damage response. *Mol Cell* **51**, 141-155 (2013).
209. Patro, R., Duggal, G., Love, M.I., Irizarry, R.A. and Kingsford, C. (2017) Salmon provides fast and bias-aware quantification of transcript expression. *Nat Methods* **14**, 417-419.

210. Love, M.I., Soneson, C. and Patro, R. (2018) Swimming downstream: statistical analysis of differential transcript usage following Salmon quantification. *F1000Res* **7**, 952.
211. Liao, Y., Smyth, G.K. and Shi, W. (2013) The Subread aligner: fast, accurate and scalable read mapping by seed-and-vote. *Nucleic Acids Res* **41**, e108.
212. Subramanian, A., Tamayo, P., Mootha, V.K., Mukherjee, S., Ebert, B.L., Gillette, M.A., Paulovich, A., Pomeroy, S.L., Golub, T.R., Lander, E.S. and Mesirov, J.P. (2005) Gene set enrichment analysis: a knowledge-based approach for interpreting genome-wide expression profiles. *Proc Natl Acad Sci U S A* **102**, 15545-15550.
213. Hänzelmann, S., Castelo, R. and Guinney, J. (2013) GSVA: gene set variation analysis for microarray and RNA-seq data. *BMC Bioinformatics* **14**, 7.